EFFICIENT RENDERING AND COMPRESSION FOR FULL-PARALLAX COMPUTER-GENERATED HOLOGRAPHIC STEREOGRAMS

A Dissertation

Presented to the Faculty of the Graduate School

of Cornell University

in Partial Fulfillment of the Requirements for the Degree of

Doctor of Philosophy

by

Daniel Aaron Kartch

May 2000

EFFICIENT RENDERING AND COMPRESSION FOR FULL-PARALLAX COMPUTER-GENERATED HOLOGRAPHIC STEREOGRAMS

Daniel Aaron Kartch, Ph.D.

Cornell University 2000

In the past decade, we have witnessed a quantum leap in rendering technology and a simultaneous increase in usage of computer generated images. Despite the advances made thus far, we are faced with an ever increasing desire for technology which can provide a more realistic, more immersive experience.

One fledgeling technology which shows great promise is the electronic holographic display. Holograms are capable of producing a fully three-dimensional image, exhibiting all the depth cues of a real scene, including motion parallax, binocular disparity, and focal effects. Furthermore, they can be viewed simultaneously by any number of users, without the aid of special headgear or position trackers. However, to date, they have been limited in use because of their computational intractability.

This thesis deals with the complex task of computing a hologram for use with such a device. Specifically, we will focus on one particular type of hologram: the holographic stereogram. A holographic stereogram is created by generating a large set of two-dimensional images of a scene as seen from multiple camera points, and then converting them to a holographic interference pattern.

It is closely related to the light fields or lumigraphs used in image-based rendering. Most previous algorithms have treated the problem of rendering these images as independent computations, ignoring a great deal of coherency which could be used to our advantage.

We present a new computationally efficient algorithm which operates on the image set as a whole, rather than on its individual elements. Scene polygons are mapped by perspective projection into a four-dimensional space, where they are scan-converted into 4D color and depth buffers. We use a set of very simple data structures and basic operations to form an algorithm which will lend itself well to future hardware implementation, so as to drive a real-time holographic display.

We also examined issues related to the compression of stereograms. Holograms contain enormous amounts of data, which make storage and transmission cumbersome. We have derived new methods for efficiently compressing this data. Results compare favorably with existing techniques.

Finally, we describe an algorithm for simulating a camera viewing a computed hologram from arbitrary positions. It uses wave optics to track the propagation of light from the hologram, through a lens, and onto a film plane. This enabled us to evaluate our rendering and compression methods in the absence of an electronic holographic display and without the lengthy processing time of hardcopy holographic printing.

Biographical Sketch

Dan Kartch was born in Pompton Plains, NJ on January 4, 1967, and was raised in Wayne, NJ. After graduating from Wayne Hills High School in 1985, he attended Cornell University in Ithaca, NY, where he majored in Physics. There, he received his first experience in computer graphics while working for astronomers Saul Teukolsky and Stuart Shapiro, producing videos of the results of their research. After receiving a B.A. in 1989, he remained at Cornell to study under Donald Greenberg in the Program of Computer Graphics. Several hundred years later, he produced the volume you are now holding, and received his Ph.D. in Computer Science.

To my parents.

Acknowledgements

First and foremost, I would like to thank my committee chair, Donald Greenberg. Don was undetered by the forward-looking nature of my research, and the fact that, even if successful, it would not prove to be practically applicable for several years after its completion, until various other technological advancements are achieved. He continued to provide advice and support, both moral and financial, despite the many, many, many, many, many, many years that it took me to finish. For this, I will always be grateful.

I would also like to thank the other members of my committee, Ken Torrance and Saul Teukolsky, for their continuing support. I am especially grateful to Saul, as well as Stuart Shapiro, who gave me a part-time job performing graphics programming during my junior and senior years as an undergraduate. It was there that computer programming, which had previously been only a hobby for me, grew to become a career. I also thank Jack Tumblin for his services as reviewer and proofreader.

I thank my parents, Matthew and Joan Kartch, my brother David, and many friends from my days as an undergraduate, whose constant nagging, er . . . I mean whose steadfast encouragement, helped me see my degree through to completion.

I thank Ben Trumbore for providing me with a place to live for most of my time in graduate school, and for serving as an avid and challenging opponent in games too numerous to count. On a similar note, I must thank Chris Schoeneman for providing an incredibly evil bit of software that wasted much valuable time which would have been better spent working, and also Gün Alppay, Sebastian Fernandez, Gene Greger, Andrew Kunz, Jed Lengyel, Brian Smits, Greg Spencer, Bretton Wade, and anyone else I may have forgotten, all of whom blowed up real good.

I am grateful to the following people who provided software or services which were invaluable during my research: our system administrators, Hurf Sheldon and Mitch Collinsworth, who kept everything running (most of the time); James Durkin, who provided support for Emacs and various other utilities; Bruce Walter, for his RGBE libraries and for generating a global illumination solution used in this thesis; Moreno Piccolotto and SuAnne Fu, for their aid in preparing several of the models used here, and Richard Meier Associates for providing one of those models to us; Pete Shirley, whose gg libraries saved me a lot of bother; and the consultants of the Cornell Theory Center for aiding me with various problems. I thank the contributors to several software projects for selflessly making the fruits of their efforts free to all and sundry: LaTeX, GNU Emacs, MPICH, FFTW, ImageMagick, and the GIMP. Similarly, I thank the following people who made their models available on the web: Barry Driessen, Dave Edwards, and Luis Filipe.

My thanks go out as well to the many other staff and students in the lab who have made my stay at Cornell so pleasant.

Last but not least, I am grateful to the various sponsors without whose sup-

port this research would not have been possible. This work was supported in part by the National Science Foundation Science and Technology Center for Computer Graphics and Scientific Visualization (ASC-8920219), and by NSF grants ASC-9523483 and CCR-8617880. Much of this research was performed on equipment generously donated by the Hewlett-Packard Corporation and the Intel Corporation. I also thank the Cornell Theory Center, which receives funding from Cornell University, New York State, federal agencies, and corporate partners, for the use of their computing resources.

Table of Contents

List of Figures

Chapter 1

Introduction

Twenty years ago, the computer was seen by most people as a mysterious and daunting device whose use was relegated to an elite few capable of mastering the arcane languages and rituals needed to invoke it. Today, it has become an indispensable tool in almost all walks of life, and is revolutionizing the fields of engineering, medicine, and scientific research. Its success is due in large part to the development of fast graphics hardware and software which enable users to interact with their data and designs at an easily comprehensible visual level.

However, as the data to be dealt with becomes more and more complex, we see increasing dissatisfaction with the limitations of standard two-dimensional display systems. No matter how fast or photo-realistic the output of rendering software becomes, it cannot take full advantage of the human visual system's capabilities so long as the results can only be viewed on a flat screen. To meet this need, a great deal of research has been dedicated to the development of three-dimensional display systems. A number of devices based on several different display methods are already commercially available, and work continues on improving these technologies and developing new ones.

One of the most promising is the electronic holographic display. A holographic display would be able to produce a completely realistic three-dimensional image of an object or scene without the need for special eyewear or position trackers. It could therefore be viewed simultaneously from any angle by any number of users.

This functionality does not come cheap. A holographic display requires a resolution several orders of magnitude higher than that of a CRT monitor. The current state of the art can provide small screens with this resolution in only one dimension, allowing the display of holograms with limited parallax and depth. It may be a decade or more before full-size, full-parallax holographic monitors become a commercial reality, but researchers are confident that this goal will be achieved.

In addition to the engineering obstacles that must be overcome, there are computational hurdles as well. Simulating the optical phenomena that produce a hologram is a much more complex problem than that which produces a two-dimensional image. Furthermore, where a typical computer-generated image requires a few million bytes of information, a hologram requires hundreds of billions or more. Not only does this present an enormous computation task, it is also a tremendous amount of data to be stored or transmitted to the display device. There is therefore a great need for algorithms to efficiently compute and compress holograms.

The most promising methods we have seen are those based on a class of hologram known as holographic stereograms, particularly the work on diffraction specific computation performed by Lucente at the MIT Media Lab. These methods will be discussed in detail later. For now we summarize by saying

that they split the computation into two stages. In the first stage, a set of two-dimensional images are generated using traditional rendering algorithms. In the second stage, these images are converted into a holographic interference pattern using Fourier techniques. These methods provide a tremendous increase in speed over single step algorithms which produce a hologram directly from a scene by simulating the interference which would occur in the real world. In addition, as Lucente showed, the images produced by the first stage can serve as a far better compression domain than the interference patterns, and using specialized hardware, we can rapidly convert from this compressed form to the final hologram.

In this thesis, we build upon this work, improving computation speed and compression statistics. Unlike much of the previous work , which focused primarily on horizontal parallax only holograms, we will look at the more general, and more computationally complex, case of full-parallax holograms. Chapter 2 provides an overview of three-dimensional display technology and discusses the advantages of a holographic display. Chapter 3 discusses previous work in computational holography. Chapter 4 proposes and compares several compression schemes. Chapter 5 presents a four-dimensional z-buffering algorithm for rapidly performing the rendering process. Chapter 6 describes a method for testing holographic rendering algorithms in the absence of an electronic holographic display to provide visual feedback. Chapter 7 concludes by summarizing our results and discussing avenues for future research.

Chapter 2

Three-Dimensional Displays

As mentioned in the previous chapter, the development of a holographic display is not a simple task. Why then, should we bother when existing technologies such as stereoscopic monitors and virtual reality headsets can already produce convincing three-dimensional effects? When we first undertook this project, we heard many questions along these lines. In order to motivate this work and answer these questions, this chapter provides a brief overview of past and present 3D display devices, and discusses their relative advantages and disadvantages.

Three-dimensional display devices have a long history, dating back to the first half of the nineteenth century. Okoshi [94, 95] and Lipton [75] provide extensive explanations and historical discussions of three-dimensional imaging techniques prior to 1980. McAllister et al. [88] describe current electronic 3D display devices and their use with computer generated images.

2.1 The need for a three-dimensional display

Our visual system transforms the two-dimensional images received by our eyes into a three-dimensional representation of the world using a combination of psychological and physiological depth cues [56]. The psychological cues are primarily functions of how the environment projects onto our retina. Examples include linear perspective, texture gradient, retinal image size, aerial perspective, relative brightness, shading, and occlusion. The physiological depth cues are functions of how our eyes adjust to view objects at different distances and how the images change when viewed from different positions. These include the focal length and convergence of the eyes, binocular disparity, and motion parallax.

Using perspective transformations, hidden surface removal, texture mapping, global illumination algorithms, and good reflection models, we can create computer generated images that provide all of the psychological depth cues. While we cannot yet produce perfectly photo-realistic images of arbitrary scenes, the differences affect the realism of the images, not their three-dimensionality. However, when we view a two dimensional image, we are focusing on a fixed object (the monitor or photograph) at a single depth. This depth is unaffected by what point in the image we look at, or how distant an object that part of the image represents, and therefore the physiological depth cues are not present.

In most cases, psychological depth cues are sufficient. However, for a growing set of applications, additional cues are needed to interpret the information being displayed. To illustrate, we will take a look at examples of three classes of applications where this is the case.

Applications where the display must match reality as closely as possible: Flight simulators are becoming increasingly important for the training of military and airline pilots. They allow difficult maneuvers to be learned, and test reactions in dangerous situations, without risk to life or property. Since the environments for which the pilots are training provide physiological depth cues, it is important that the simulations provide them as well. Otherwise, the perceptual changes when going from the simulator to the real world may slow reaction time and lead to fatal mistakes.

Applications where psychological depth cues are present but useless: Our visual system's use of psychological depth cues is adapted to deal with environments normally encountered in the real world, and can fail when we are placed in highly atypical surroundings. If placed in a room whose dimensions have been deliberately distorted to project the same image on the retina as a normal room while actually being quite different, we will interpret the scene as the more familiar environment, rather than as it truly is. If placed in an environment that does not resemble anything we have ever encountered, we will have a hard time interpreting it at all. Scientific data sets provide just such an environment. We do not encounter complex molecular chains or colored clouds representing electrical potentials in our normal visual world, and therefore have difficulty understanding them when displayed on a monitor, no matter how realistically they are rendered. A three-dimensional display radically improves this situation. The addition of physiological depth cues causes coherent structures in the data to be immediately apparent to the user, greatly increasing the usefulness of scientific visualization software.

Applications where psychological depth cues are absent or undesirable: Consider the design of an air traffic control system. The controllers need to be able to monitor the paths of multiple, widely-separated objects through a mostly empty three-dimensional space. Because this environment is so sparse, the dominant psychological depth cues which would be available in a realistic rendering would be the retinal image size and aerial perspective. These, however, are undesirable in this situation, because they would make it difficult for controllers to see distant airplanes. Instead, they are forced to use two-dimensional abstractions with image position representing map coordinates and height indicated by textual annotations. These displays require some experience to use since it is difficult to determine from a 2D image whether or not two airplanes in the 3D space will come close enough for there to be a danger of collision. What is really needed here is a three-dimensional display which the controller can view from any angle, easily and accurately determining the relative positions and paths of every plane.

As these three cases illustrate, there is a growing class of applications for which ordinary two-dimensional displays are inadequate. The depth cues they provide are insufficient to allow the user to easily and naturally interpret the scenes being rendered. With the introduction of a three-dimensional display, these problems can be overcome. In addition, Merrit [91] lists several other side-benefits of 3D displays: they aid in filtering visual noise and provide greater effective image quality; they provide a wider total field of view; and they allow the display of luster, scintillation, and surface sheen (which are highly dependent on viewing position), improving the realism of images.

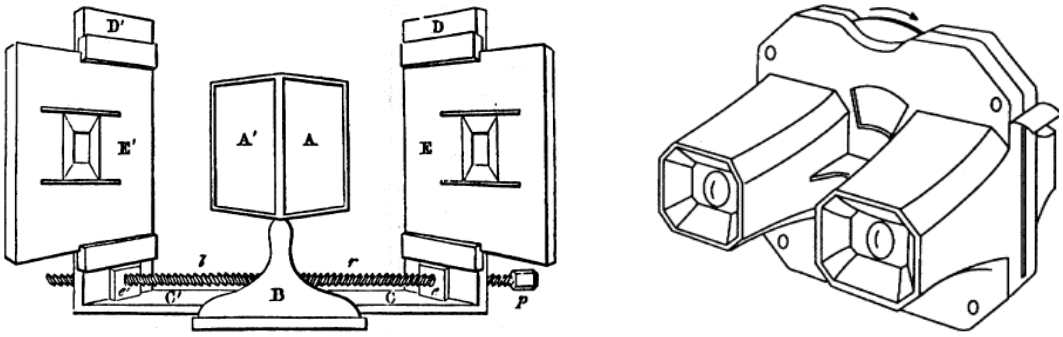

(a) **(b)**

Figure 2.1: (a) Wheatstone's original stereoscope, (b) the View-Master, its modern descendent. (Images from [75] and [88], respectively.)

2.2 Stereoscopic displays

The easiest physiological depth cue to provide is binocular disparity. The effect of binocular disparity on depth perception was first demonstrated in the 1830's by Sir Charles Wheatstone [123] with the invention of the stereoscope (Figure 2.1). This device took a pair of drawings, made from two slightly different positions, and used a set of mirrors to present one to each of the user's eyes, creating a striking illusion of three-dimensionality (Figure 2.2). The View-Master, introduced in 1940 and still sold in toy stores today, is a modern descendent of this device.

Two decades after Wheatstone first published his results, two techniques (the *eclipse system* and the *anaglyph*, discussed below) were introduced which allowed images for the left and right eyes to be displayed on a common viewscreen. Special eyewear was used to ensure that each eye received only the intended image. These innovations made it possible for stereoscopic displays to be viewed by more than one person at a time. Since then, numerous stereoscopic imaging techniques have been developed, many of which have been adapted for

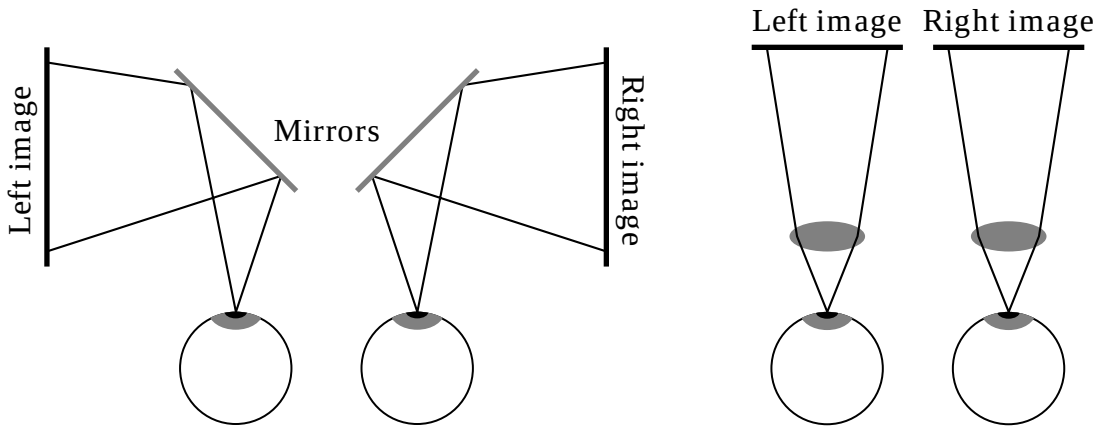

(a) Wheatstone's stereoscope **(b)** View-Master

Figure 2.2: Schematics of the devices in Figure 2.1. The mirrors / lenses are adjusted so that the images appear in a natural viewing position. The left and right eye images are fused by the human visual system to create an illusion of three-dimensionality.

electronic displays.

2.2.1 Liquid-crystal shutter systems

Passive screen, active glasses

One of the most popular stereo display methods is an adaptation of the *eclipse system* (Figure 2.3). According to Lipton [78], this system was invented in 1858, and first used commercially by Laurens Hammond in 1922. Images for the left and right eyes are projected in alternation onto a single screen. The user views the screen through headgear containing shutters for each eye. The shutters open and close in synchronization with the projectors so that the left eye sees one set of images and the right sees the other.

Numerous mechanical and electrical shuttering systems have been developed since then, but none could be made commercially feasible until modern electro-optical materials were developed. In the mid-70's, John Roese used

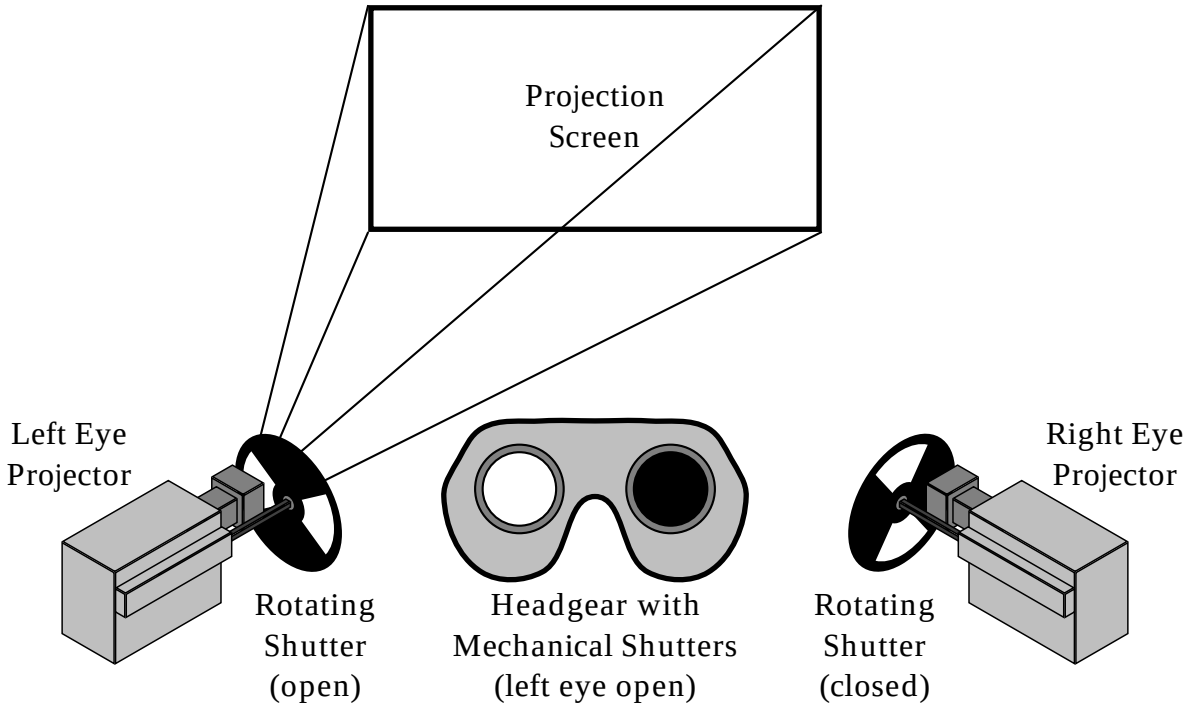

Figure 2.3: A simple 3D projection system using the eclipse method. The shutters on the projectors rotate so that each projector provides every other frame. The shutters in the headset are synchronized with the projectors so that each eye only sees the images from the corresponding projector.

the recently invented lead lanthanum zirconate titanate (PLZT) ceramics, sandwiched between two polarizers, as shuttering lenses in a pair of stereo goggles [100, 101]. The lenses' states could be made to alternate between transparent and opaque with the application of an electric current. Frame buffers were used to alternate the image on a television monitor between left and right eye images with each frame, and the signals sent to the lenses were synchronized with the monitor.

These goggles produced an effective illusion of depth, but had several problems: they were dim, they produced a distracting and disturbing flicker, and they tethered the user to his monitor with a power cord. The flicker was elimi-

nated with the introduction [80] of a 120 Hz monitor. The dimness was solved by replacing the PLZT with liquid-crystal (LC) shutters [51], which provided much higher transparency. The LC shutters also drew much less power, allowing the power cord to be eliminated in favor of a battery in the glasses [77]. Synchronization of the shutters with the display was now provided by an infrared emitter mounted atop the monitor. StereoGraphics has been quite successful marketing this device under the brand name CrystalEyes [109].

Active screen, passive glasses

A related display device is based on a method demonstrated by Edwin Land [12] in 1935, which, in turn, is a more sophisticated version of the *anaglyph*, introduced by Ducos du Hauron in 1858. The anaglyph uses two superimposed drawings from slightly different viewpoints, one colored green and the other red. Green and red tinted lenses are worn which filter out the corresponding drawing, ensuring that each eye receives only the desired image. Land's system (Figure 2.4) displayed the left and right images simultaneously, using two projectors whose lenses were covered by polarizers aligned perpendicular to each other. The viewers wore glasses containing a pair of polarized lenses, each aligned parallel to the polarizer on the corresponding projector. These lenses prevented perpendicularly polarized light from passing through, so each eye only received the intended image. During the early 1950's, the motion picture industry experienced a short-lived boom in 3D movies made with this technique, and it is still used for the occasional 3D film made today.

This method can also be used to construct electronic stereoscopic displays. As with the system in the last section, a monitor is used to alternately display

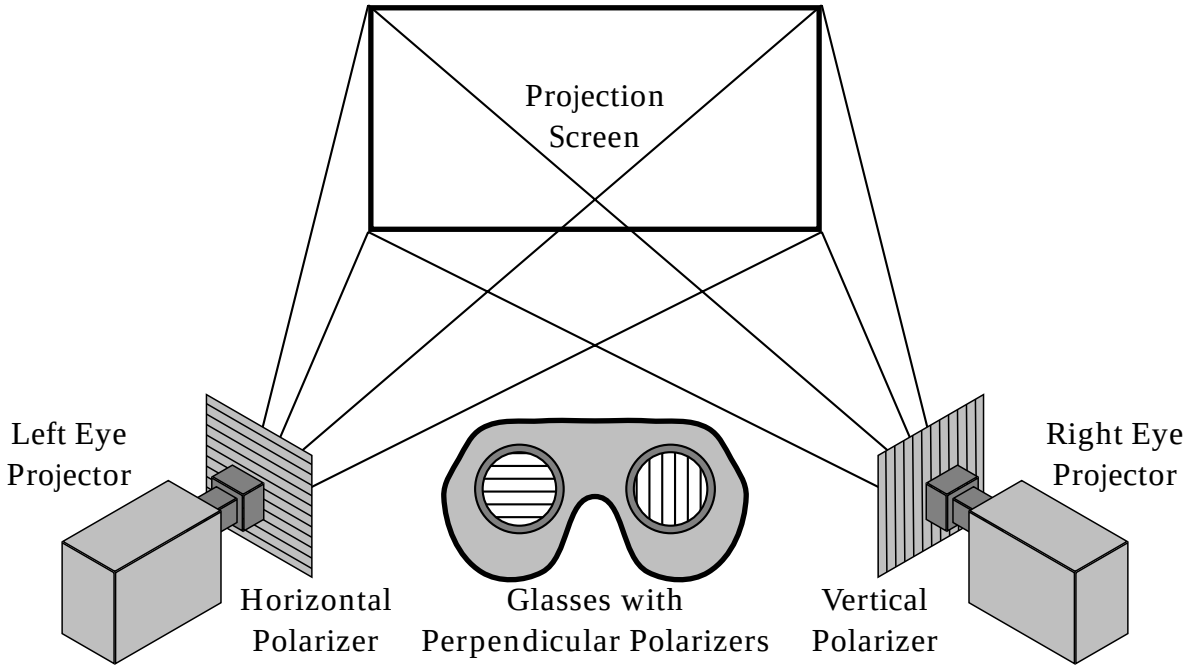

Figure 2.4: Land's stereoscopic projection system. The projectors produce two perpendicularly polarized images on the viewscreen. The polarized glasses filter out the appropriate image for each eye.

right and left images. Instead of a shutter mechanism built into the lenses, the monitor is covered with a transparent liquid-crystal screen whose polarization alternates between vertical and horizontal in sync with the monitor [79]. The user now wears only a simple and inexpensive pair of polarized lenses. The large polarized screen is more expensive to make than the LC shutter glasses, but is becoming more cost effective with the introduction of new LCD technology, especially in situations where the display is to be seen by many viewers at once, such as with a large projection-screen display [76].

Common characteristics of LC shutter displays

These displays allow affordable, three-dimensional viewing for multiple users. However, they have several disadvantages. First, they only provide a proper image of the environment for a single viewing position. Looking at the monitor from a different position causes the image to appear oddly sheared. The addition of a head-mounted position tracker [1,92] fixes this problem, but the image will still only be optimized for a single viewer. Second, the rapid switching back and forth between the two eyes, as well as a phenomena called "ghosting" caused by the decay rate of the monitor's phosphors being too slow, have been known to cause eye strain when used for extended periods. Finally, the glasses can be inconvenient and uncomfortable to use for long periods, especially when worn over a pair of prescription glasses.

2.2.2 Chromostereoscopy

Another method for producing stereo images is chromostereoscopy [26, 108]. This process takes advantage of the fact that light of different wavelengths will bend at different angles when passed through a prism. Using a pair of prisms made of different materials placed against each other, the amount of divergence can be finely controlled (Figure 2.5). By viewing an image through two of these *superchromatic prisms*, the apparent depth of objects in the image will vary depending on their color (Figure 2.6). By coloring images appropriately, one can construct strikingly three-dimensional scenes with this method.

This method has the advantage over the liquid-crystal displays of the previous section of being extremely easy and inexpensive. Any standard color television or printer can be used, and only a set of cheap plastic glasses is needed.

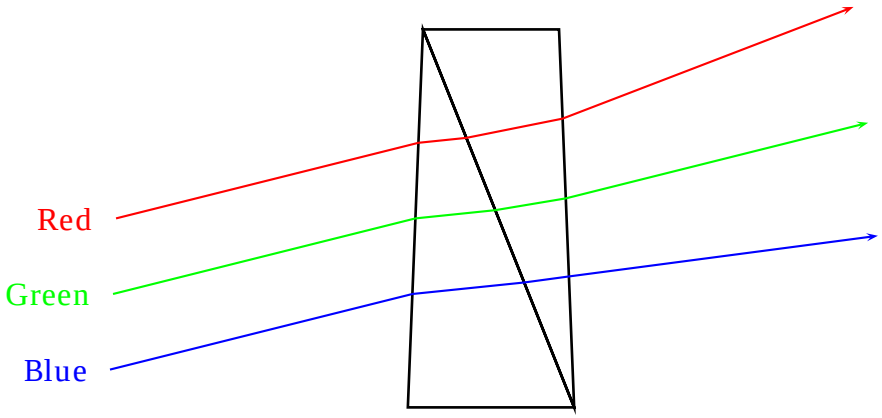

Figure 2.5: Superchromatic prism

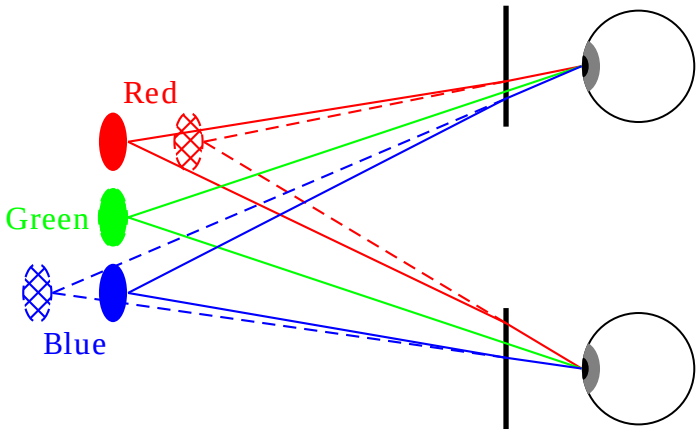

Figure 2.6: An image viewed through chromostereoscopic lenses. The light is bent by the prisms so that blue objects appear more distant and red objects appear closer. The solid objects represent the real positions of the images, while the dashed objects indicate their apparent positions.

In fact, this is actually an enhancement of an effect already present in human vision [58,116], and images made with this technique can often be viewed without the use of special lenses at all. However, it requires that the color of the image be totally devoted to depth. This limits the technique's usefulness for scientific visualization or the display of real scenes, making it mainly appropriate for artists.

2.2.3 Head-mounted displays

In 1968, Ivan Sutherland eliminated the free standing television completely and mounted a pair of miniature CRTs directly over the user's eyes [111]. Combined with a position tracker, this provides both binocular disparity and motion parallax, creating an illusion of total immersion in a three-dimensional environment. Sutherland's research gave birth to the field of virtual reality [17,110]. Although only now becoming commercially viable, this technology has gained a great deal of interest, and is likely to become the method of choice for many applications.

Nevertheless, it suffers from many of the same drawbacks as the liquid-crystal displays described in Section 2.2.1. A head-mounted display system can only be used by a single person at a time. Instead of the flicker and ghosting of the LC displays, head-mounted displays currently suffer from a lag between the time the user moves his head and the time the image updates, causing a form of motion sickness known as "simulator sickness". These weaknesses make head-mounted displays unsuitable for many applications.

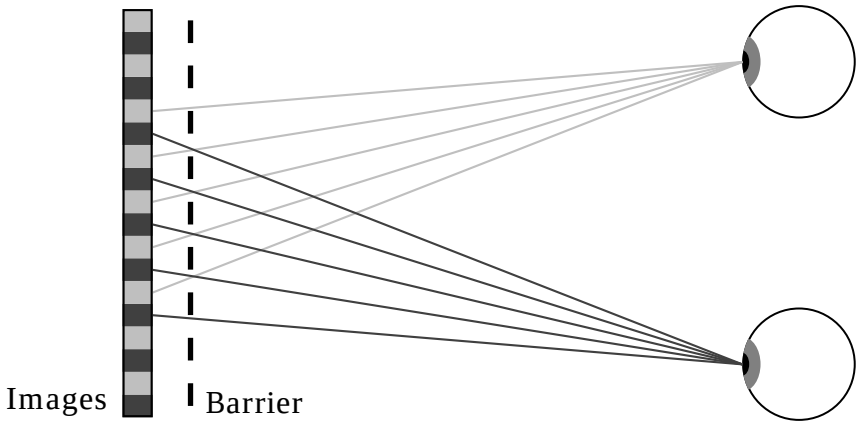

Figure 2.7: A parallax barrier display with two images. The barrier ensures that only one image is visible from any given position. By decreasing the slit size, a display with more images can be created.

2.2.4 Autostereoscopic displays

One of the major drawbacks of all of the above systems is the need to don special headgear to use them. A simple desk monitor that can produce a three-dimensional image all by itself would be much more convenient. Several manufacturers are therefore experimenting with autostereoscopic imaging techniques.

The first such technique was the parallax barrier [54, 55], invented in 1903. A parallax barrier is an opaque screen with many thin vertical slits, placed a slight distance in front of a piece of photographic film (Figure 2.7). An image projected through the barrier will be recorded on the film as a series of thin strips. Depending on the width and separation of the slits, a number of images can be recorded in this way from different angles without interfering with each other. Once the film is developed, the parallax barrier will ensure that a viewer looking at it from any given direction will see only the image taken from that angle. This not only produces a stereoscopic effect, it also allows the user to

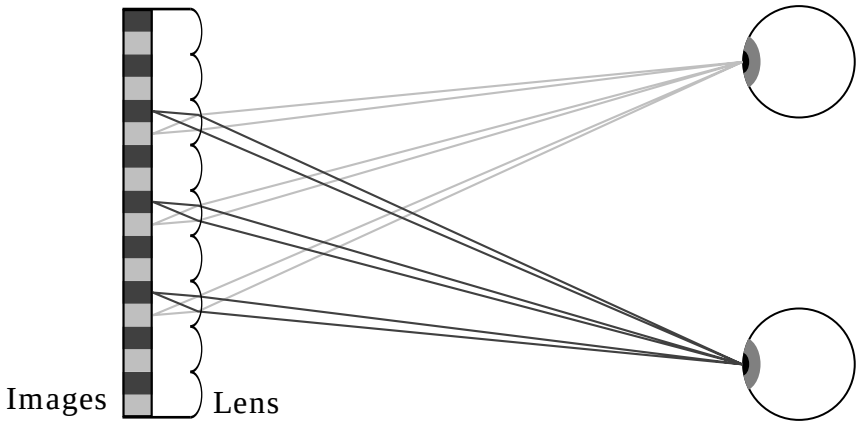

Figure 2.8: A lenticular sheet display with two images. The lenses bend the light so that only one image is visible from any given position.

move around the display and view the 3D environment from any angle.

A related technique is the lenticular sheet [95], invented in the 1920's. Instead of an opaque barrier, the image is covered with a transparent sheet composed of a series of cylindrical or elliptical lenses (Figure 2.8). Rather than blocking light from a given direction, these lenses redirect it so that the viewer only sees the appropriate part of the composite image. This allows much more light into the system, resulting in brighter, clearer images than those provided by the parallax barrier.

Both of these methods can readily be adapted to electronic displays. A monitor can easily be designed with a built in parallax barrier or lenticular sheet [18, 39, 104], and software to produce the necessary composite images is easy to write. Of course, there is a trade-off between image resolution and the number of images, since the resolution of the underlying monitor remains fixed. In addition, several other variations on this theme unique to electronic displays are also possible [40, 41, 112].

Although they free the user from the inconvenience of headgear, these displays are still not perfect. The number of discrete angles for which views can be provided is limited, and the changes between them are abrupt and disturbing. This problem can be solved with the addition of a position tracker [103], but this reintroduces the problem of headgear and prevents them from being effectively used by more than one person.

2.2.5 Stereoblindness

In addition to the individual disadvantages possessed by all of these stereoscopic technologies, there is the problem of stereoblindness. A small but non-negligible portion of the population lacks the ability to fuse stereo pairs into a three-dimensional whole without additional depth cues [96, 99]. The exact number of people who suffer from this is a matter of debate, and appears to be dependent on the testing method used, but all studies place it between one and ten percent of the population. For these people, most of the devices described in this section are useless. In the next two sections, we will see several experimental displays designed to take advantage of *all* of the physiological depth cues.

2.3 Direct volume displays

Direct volume displays draw points throughout a three-dimensional volume of space. They are also known as multi-planar displays, since they essentially have several image planes rather than the single one provided by a two-dimensional monitor. Because the images created are truly three-dimensional, they provide

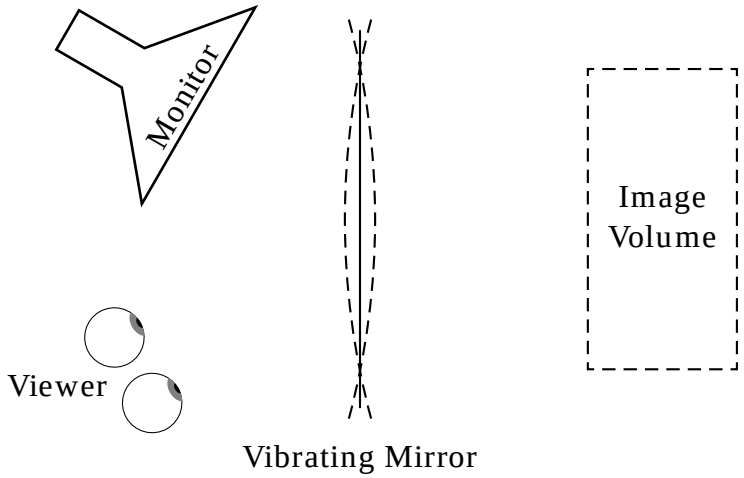

Figure 2.9: A varifocal mirror display. Due to the curvature of the mirror, the image of the monitor moves through a large volume, despite the small range of the mirror itself.

all of the physiological depth cues.

2.3.1 Varifocal mirror displays

The first multi-planar displays were varifocal mirror devices [98, 106]. These displays consisted of a rapidly oscillating mirror and an ordinary CRT monitor (Figure 2.9). They were used by viewing the reflection of the monitor in the mirror. Because the mirror was oscillating, the position of the image reflected in it would also oscillate. By rapidly changing the image displayed on the monitor, one could create the illusion of a continuum of images floating in three-dimensional space.

2.3.2 Rotating screen displays

Varifocal mirror displays were limited in both the size of their display volume and the angles from which they could be viewed. They have since been aban-

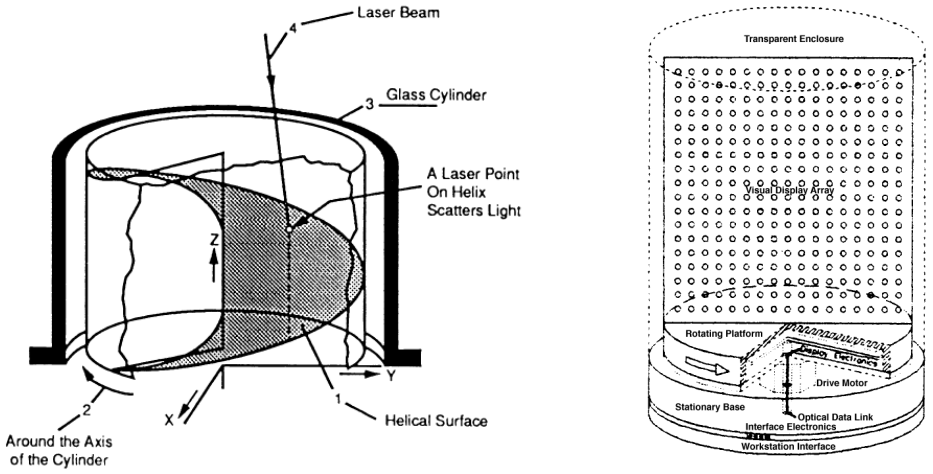

(a) Translucent screen **(b)** LED array

Figure 2.10: Rotating screen displays. (Images from [88, pg. 237] and [107], respectively.)

doned in favor of more versatile rotating screen displays [30,107,124,125]. These use a flat or helical screen rotating within an enclosed volume (Figure 2.10). In most cases, the screen is translucent and a laser is used to draw points on it as it passes through space. In a few devices the screen itself is composed of an array of LEDs which can be rapidly turned on and off. With these devices, one can theoretically draw arbitrarily complex figures throughout the display volume.

Not only do rotating screen displays take advantage of all of the physiological depth cues, they allow any number of people to use them, and they provide a full 360 degree field of view. This makes them ideally suited for certain classes of applications, such as the air traffic control system example discussed in Section 2.1. However, while they gain physiological depth cues, they lose an important psychological cue: occlusion. In addition, their use is limited to environments which can be contained in the display volume. This makes them unsuitable for large environments or applications requiring realistic rendering.

2.4 Holographic displays

Perhaps the most promising 3D display technology is the holographic display system. Holograms work by completely reproducing the light (at a wavelength scale) given off by an actual object or objects. They therefore provide all the depth cues present in the real scene, both psychological and physiological. Although not yet a commercial reality, an electronic display based on holographic principles would produce a completely realistic three-dimensional image of an environment, viewable from any angle, without any headgear needed.

Stephen Benton [4–6] provides an overview of holographic imaging technology prior to 1985. Since then, there has been an explosion of proposed methods for constructing a high-resolution, real-time, electronic holographic display [7,9–11,13,14]. Although it remains unclear which of these will prove to be most viable, all but the most skeptical developers agree that commercially available electronic holographic displays will be a reality within twenty years [126].

Chapter 3

Computer-Generated Holography

The word *hologram* comes from the Greek roots *holos* and *gramma* and literally means “total message”. In general, holography refers to any process which allows both the magnitude and phase of a wave to be recorded and later reconstructed. It can be applied to any type of wave phenomenon, including light, sound, and quantum mechanical particle scattering. However, the most well known forms of holograms are those made with visible light. These three-dimensional images, which can be found on everything from toys to credit cards to museum walls, are what we wish to simulate.

The hologram was introduced in 1948 by Dennis Gabor [42–44], who proposed it as a means of improving the resolution of the electron beam microscope. He exposed a piece of photographic film to monochromatic light passing through a very small photographic slide. This light formed a microscopic interference pattern, which the film was able to capture. Gabor showed that illuminating the developed film with the same light source would produce an image of the slide, suspended in space at it’s original position. He called this process *wavefront reconstruction*.

Due to the lack of a coherent light source, little progress was made in the field until the invention of the laser in 1960. This device enabled Leith and Upatnieks [63–65] to produce the first holograms of solid objects. Since then, significant improvements in holographic recording techniques have been made, and holography has become a minor art form. However, the basic principles remain the same: coherent light is passed through or reflected off of a set of objects, combined with a reference beam, and the resulting interference pattern is used to expose a piece of film.

Unfortunately, while producing a hologram is not much more complicated than producing a photograph, *computing* one is a far more difficult task than computing a two-dimensional image. One can begin to understand this complexity by considering the fact that a photograph contains the image seen from a single point, while a hologram contains the images seen from every point across it's surface. However, the problem is even more fundamental than this. Holograms and photographs require completely different models of light to compute.

Traditional rendering algorithms are based on the particle model of light. Light sources are considered emitters of photons or rays, which travel through space in straight lines until they strike a surface, where they can partially or completely reflect and/or refract. How closely this process is modeled varies widely depending on the algorithm used, but in all cases, the light propagation obeys simple rules of geometric optics. In general, under this model, the light throughout space can be represented by a real-valued scalar function $L(\vec{x}, \vec{\omega}, \lambda)$ of six variables: the position $\vec{x} = (x, y, z)$; the direction of propagation $\vec{\omega} = (\theta, \phi)$; and the wavelength λ. Computing an image is essentially equivalent

to evaluating this function at a single point in space (for a pinhole camera) or across a small region (for a finite aperture).

On the other hand, holography theory is based on the wave model of light. Under this model, light can be represented by a complex-valued vector field $\vec{F}(\vec{x}, \lambda)$ of four variables. This can be either the electric field, $\vec{E}$, or the magnetic field, $\vec{B}$. The intensity of light at a given point is proportional to the square of this field's magnitude. Instead of following simple geometric rules, $\vec{F}$ propagates according to a set of differential equations. To compute a hologram, we must solve these equations to evaluate this function across it's entire face.

From a computational standpoint, the key difference between these two representations is their relative coherence. The function for the particle model is dominated by low-frequency components and possesses a great deal of coherence. Rendering algorithms can take advantage of this by making numerous approximations which decrease computation time without adversely affecting the image quality. The wave model representation is dominated by high-frequency terms on the scale of the wavelength of light. This means that the computation must be carried out at a much finer level.

A numerical representation of a hologram requires about 10^9 sample points per square centimeter. To perfectly simulate the hologram's formation, the objects in the scene must be sampled at the same level, and the contribution of every object point to every point on the hologram must be considered. Even for small holograms of simple scenes, this can require over 10^{20} operations, well beyond the limits of current computer technology.

Research in computer-generated holography has therefore focused on finding approximations in the scene description and the light itself which allow the

complexity to be reduced. The early evolution of these techniques can be observed in several review papers [27, 34, 52, 62, 68, 115] dating from 1971 through 1989. This chapter discusses these methods as well as more recent ones, and examines their advantages and disadvantages.

3.1 Notation

We begin by describing the notational conventions which will be used throughout this thesis. We use italic text to represent real-valued variables and functions (a, f, F, x, ...), and bold italic for complex values ($\boldsymbol{a}$, $\boldsymbol{f}$, $\boldsymbol{F}$, $\boldsymbol{x}$, ...). Oblique text is used for constants (a, f, F, x, ...). In particular, i is used to denote $\sqrt{-1}$.

Spatial coordinates are denoted by $\vec{x}$, with or without a subscript ($\vec{x}_p$,$\vec{x}_s$, ...). For a point $\vec{x}_p$, the individual coordinate components are (x_p, y_p, z_p). Vectors are denoted by other letters, notably $\vec{r}$ and $\vec{k}$. Given a vector $\vec{r}$, its magnitude is represented by the scalar $r \equiv \|\vec{r}\|$ and its direction by the unit vector $\hat{r} \equiv \frac{\vec{r}}{r}$. In Cartesian coordinates, its components are written as (r_x, r_y, r_z), while in polar coordinates we use (r, r_θ, r_ϕ). We also use $\vec{\omega} = (\theta, \phi)$ to denote a generic unit vector.

For an expression $\boldsymbol{U}$ dependent on variable x, we define

$$\mathcal{F}_x \{\boldsymbol{U}(x)\}(k) \equiv \int_{-\infty}^{+\infty} \boldsymbol{U}(x) e^{i2\pi kx} dx \tag{3.1}$$

to be the Fourier transform of $\boldsymbol{U}$ with respect to x evaluated at k. Similarly, the inverse Fourier transform is given by

$$\mathcal{F}_k^{-1} \{\boldsymbol{u}(k)\}(x) \equiv \int_{-\infty}^{+\infty} \boldsymbol{u}(k) e^{-i2\pi kx} dk. \tag{3.2}$$

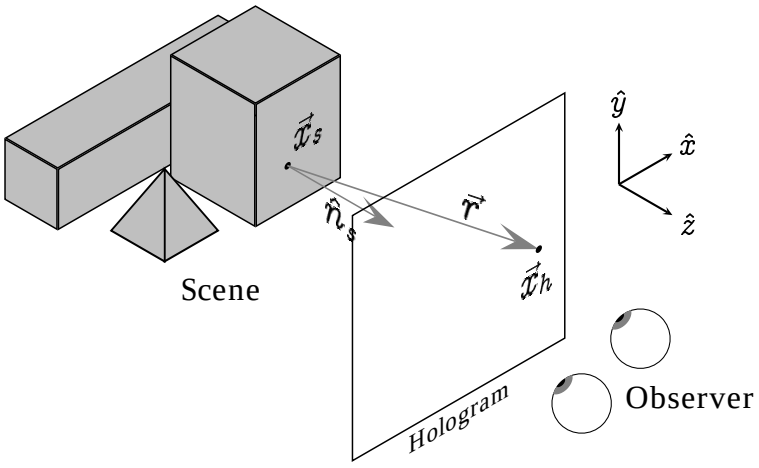

Figure 3.1: A sample scene to be rendered holographically

In discrete form, for an array $\boldsymbol{U}_i$ with n samples, these equations become

$$\mathcal{F}_i\{\boldsymbol{U}_i\}_j \equiv \sum_i \boldsymbol{U}_i e^{i2\pi\frac{ij}{n}} \tag{3.3}$$

$$\mathcal{F}_j^{-1}\{\boldsymbol{u}_j\}_i \equiv \sum_j \boldsymbol{u}_j e^{-i2\pi\frac{ij}{n}}. \tag{3.4}$$

3.2 Problem definition

For the purposes of this discussion, we will consider the task of computing a hologram of the simple scene shown in Figure 3.1. The holographic film lies in the x-y plane centered at the origin, and will be viewed by observers in the positive z region. The objects are shown here a short distance behind the hologram, but in general may be placed anywhere, including in front of, or even passing through, the hologram plane.

We assume that the scene is illuminated by monochromatic light of wavelength λ and wavenumber $k = \frac{2\pi}{\lambda}$. Although the light $\vec{\boldsymbol{F}}$ is a vector field, we will consider only one vector component, since, in most circumstances, the three components operate almost independently and identically. Our representation

for the light throughout space becomes $\boldsymbol{F}(\vec{x})$. Note that these assumptions ignore some of the finer details of electro-magnetic wave propagation, notably near- and sub-surface effects, but these factors can be safely omitted when computing a hologram. The value of $\boldsymbol{F}$ at all points $\vec{x}_s$ on the objects' surfaces is directly related to the light emitted by and reflected from them. It can be found using existing illumination algorithms in combination with a high frequency phase factor to account for directional variations. Given this $\boldsymbol{F}(\vec{x}_s)$, we must determine the value of $\boldsymbol{F}(\vec{x}_h)$ at every point on the hologram.

Note that to record a hologram, the light from the objects must be combined with a reference wave, and to reconstruct the image, the same wave must be used to illuminate the hologram. For the sake of simplifying this discussion, we will omit this wave and treat the hologram as if it were made of some ideal substance that can perfectly record, and later reproduce, both the magnitude and phase of light across it. Nevertheless, the reader should be aware that when implementing any of the algorithms discussed here, it will be necessary to add such a reference wave to the computed field $\boldsymbol{F}(\vec{x}_h)$ in order to produce a usable hologram.

For simplicity, we assume that the hologram is square, with sides of length D, and that the same sample spacing, δ, is used in both directions. If we define Θ to be the largest angle at which the hologram will be viewed (Figure 3.2), then δ is constrained by

$$\delta \leq \frac{\lambda}{4 \sin \Theta}.$$

We use twice the usual Nyquist sampling rate here because the holographic recording process captures the complex wavefront as a real-valued intensity field, so more samples are needed to reconstruct both the real and imaginary

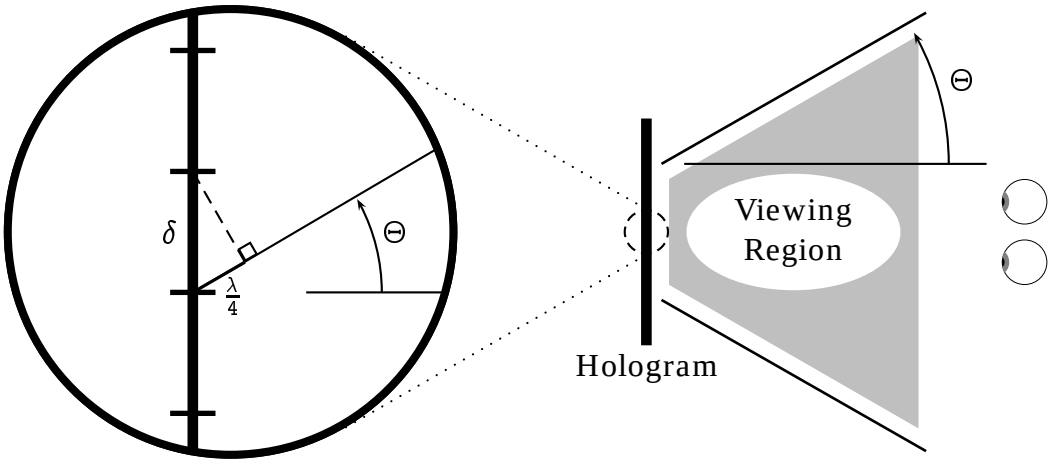

Figure 3.2: Dependence of hologram sampling on maximum viewing angle

parts. Given δ, we define the pitch $p \equiv \frac{1}{\delta}$ to be the number of samples per unit length, and $N_\delta \equiv D \cdot p = \frac{D}{\delta}$ to be the number of samples along each side of the hologram. For visible light, λ lies between about 400 and 700 nm, and for a typical hologram, Θ is about 30 or 45 degrees, so typical values are on the order of $\delta \approx 250$ nm and $p \approx 4000$ samples / mm.

The hologram is square, so it contains a total of ${N_\delta}^2$ samples. To accurately simulate the hologram's formation, we will also need to sample the object surfaces at the Nyquist limit, $\frac{\lambda}{2}$, so they too will each require $O({N_\delta}^2)$ sample points. For a snapshot-sized hologram, N_δ is on the order of 10^5. In addition, we define N_o to be the number of objects in the scene to be rendered. Although most of the computer generated holography (CGH) literature has dealt only with scenes containing a handful of objects, we should expect that for a realistic environment, N_o can also be on the order of 10^5 or more.

In the absence of occlusion, the light at a point $\vec{x}_h$ on the hologram is given

by

$$\boldsymbol{F}(\vec{x}_h) = \frac{1}{i\lambda} \iint \boldsymbol{F}(\vec{x}_s) \frac{e^{ikr}}{r} (\hat{n}_s \cdot \hat{r}) d\vec{x}_s, \tag{3.5}$$

where $\boldsymbol{F}(\vec{x}_h)$ is the light at location $\vec{x}$, $\vec{x}_s$ is a position on an object surface, $\vec{x}_h$ is a position on the hologram, $\vec{r}$ is the vector from $\vec{x}_s$ to $\vec{x}_h$, and $\vec{n}_s$ is the surface normal at $\vec{x}_s$ (see Goodman [45, Ch. 3-4] for details). For a single object, this integral can be computed numerically with $O({N_\delta}^2)$ operations. The computation must be performed for all N_o objects and all ${N_\delta}^2$ hologram points, so the total time required is $O(N_o {N_\delta}^4)$.

When objects are allowed to occlude one another, as is the case for all but the most trivial scenes, accurate simulation of the hologram formation requires accounting for the diffraction around objects. This is an extremely difficult problem to solve for arbitrary environments, so we usually assume that diffraction has a negligible effect on the image seen by the viewer, and consider only direct point-to-point occlusion. Equation (3.5) becomes

$$\boldsymbol{F}(\vec{x}_h) = \frac{1}{i\lambda} \iint V(\vec{x}_s, \vec{x}_h) \boldsymbol{F}(\vec{x}_s) \frac{e^{ikr}}{r} (\hat{n}_s \cdot \hat{r}) d\vec{x}_s, \tag{3.6}$$

where $V(\vec{x}_s, \vec{x}_h)$ is 1 if $\vec{x}_s$ and $\vec{x}_h$ are directly visible from one another, and 0 if another object lies between them. This visibility function requires, at worst, $O(N_o)$ time to compute, so the total time to compute the hologram becomes $O({N_o}^2 {N_\delta}^4)$. Since N_o and N_δ can both number in the hundreds of thousands, it is necessary to find ways to reduce this complexity for the problem to become feasible.

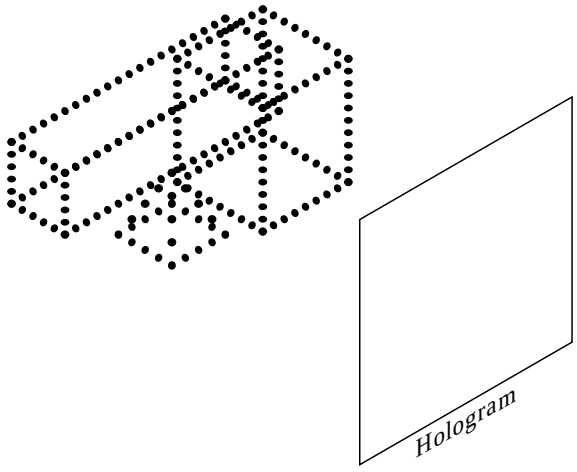

Figure 3.3: Scene with objects replaced by point sources

3.3 Geometric simplifications

One way in which the complexity can be reduced is to simplify the geometry of the scene to forms whose emissions can be more easily computed. Waters [118, 119] replaced the objects with a series of closely spaced point sources lining the surface edges (Figure 3.3). This reduces the dimensionality of the objects from two-dimensional surfaces to one-dimensional lines, allowing a corresponding reduction in the number of object sample points required. Additionally, since we are no longer trying to display realistic surfaces, we no longer need to sample the objects at wavelength scale. It is sufficient to position the points closely enough so that the gaps are not visible to an observer. The complexity of the algorithm becomes $O(N_o {N_\delta}^2 N_p)$, where N_p is the number of point sources per object, which can now be measured in hundreds rather than hundreds of thousands.

Frère and Leseberg [24,67] took this a step further by finding analytical solutions for the propagation of light from a luminous line segment to the hologram

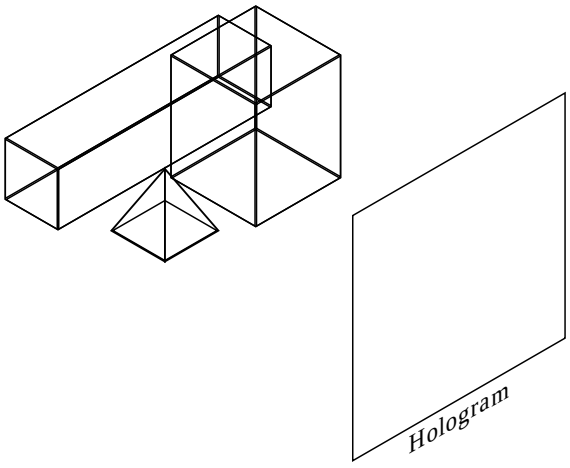

Figure 3.4: Scene with objects replaced by line sources

(Figure 3.4). This allows the objects to be represented by a few lines, rather than hundreds of points. The time required now becomes $O(N_o {N_\delta}^2 N_l)$.

Despite the increased speed of this algorithm, a great deal is lost by replacing the objects with points or lines. Obviously, we cannot present objects with realistic surface properties, such as textures and complex reflection patterns, because there are no surfaces at all. Additionally, lines cannot provide any occlusion, so objects which should be hidden behind others will instead be visible through them, turning large scenes into confusing jumbles. Thus, while this technique is suitable for applications where we might use a wire-mesh rendering program, such as some engineering and design problems, it will not produce realistic images.

3.4 Fourier holography

Both in research and in practice, the most widely used CGH methods are forms of Fourier holography. This subfield uses a variety of approximations to ex-

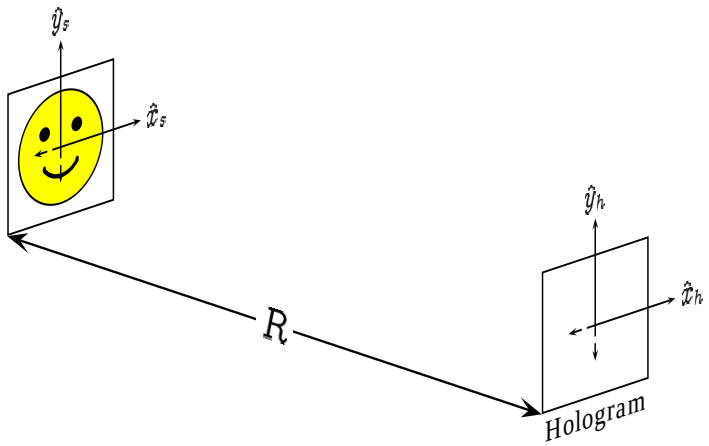

Figure 3.5: A Fraunhofer hologram. The scene consists of a single planar object placed a large distance from the film plane.

press the light received by the hologram in terms of a Fourier transform of the light emitted by the objects. Such representations allow the computation to be performed using fast Fourier transforms (FFTs) [19, 20, 81], greatly reducing the time required.

3.4.1 Fraunhofer holograms

The very first computer-generated holograms were Fraunhofer holograms [21]. Fraunhofer holograms are made by placing the object(s) a very great distance from the holographic film. Specifically, suppose our scene consists of a single planar object lying perpendicular to the $\hat{z}$ axis, as shown in Figure 3.5. Then the Fraunhofer approximation [45, Ch. 4] requires that the distance R between it and the hologram is large enough that

$$R \gg \frac{\pi \max_s (x_s^2 + y_s^2)}{4\lambda}. \tag{3.7}$$

At this distance, the difference in path length between a point on the hologram and any two points on the object will be significantly less than the wavelength.

This is quite large, so Fraunhofer holograms are not actually made with objects at that distance. Instead, the object is placed much closer, and lenses are used to optically move the object far enough away.

This approximation allows several simplifications to be made to Equation (3.5). The magnitude of $\vec{r}$ is dominated by R, and can be approximated by the first few terms of a binomial expansion:

$$r \approx R\left[1 + \frac{1}{2}\left(\frac{x_h - x_s}{R}\right)^2 + \frac{1}{2}\left(\frac{y_h - y_s}{R}\right)^2\right]. \tag{3.8}$$

Combining Equations (3.5), (3.7), and (3.8) yields

$$\boldsymbol{F}(x_h, y_h) = \frac{e^{ikR}}{i\lambda R}\, e^{i\frac{k}{2R}(x_h^2 + y_h^2)} \iint \boldsymbol{F}(x_s, y_s)\, e^{-i\frac{2\pi}{R\lambda}(x_h x_s + y_h y_s)} dx_s dy_s \tag{3.9}$$

$$= \frac{e^{ikR}}{i\lambda R}\, e^{i\frac{k}{2R}(x_h^2 + y_h^2)}\, \mathcal{F}^{-1}_{(x_s, y_s)}\left\{\boldsymbol{F}(x_s, y_s)\right\}\left(\frac{x_h}{R\lambda}, \frac{y_h}{R\lambda}\right). \tag{3.10}$$

Equation (3.10) is just the inverse Fourier transform of $\boldsymbol{F}$, evaluated at $\left(\frac{x_h}{R\lambda}, \frac{y_h}{R\lambda}\right)$, and multiplied by a quadratic phase factor. It should therefore come as no surprise that this technique was first used to compute holograms the year after the introduction of the fast Fourier transform [33]. Using FFTs, this equation can be computed in $O({N_\delta}^2 \log N_\delta)$ time. If we add a factor of N_o to this complexity, we can make holograms of multiple planar objects at different depths. Because of their speed and simplicity, much of the early work in computer-generated holography was done with this type of hologram [21–23, 60, 61, 82]. However, while Fraunhofer holograms are useful for a number of applications, such as developing pattern recognition systems, they have several drawbacks which make them unsuitable for use in three-dimensional imaging systems.

The source of many of these problems is the large distance R between the objects and the hologram. For example, if our hologram and objects are a few centimeters across, Equation (3.7) requires that R be over two kilometers. Lenses

are used in the reconstruction process to allow the image to be seen despite this great distance, but the three-dimensionality of the objects is entirely lost. There will be no parallax, perspective, or depth of focus effects, because the light rays reaching the eye are almost perfectly parallel. For this reason, creating Fraunhofer holograms with multiple depth planes is not useful, since the difference in depth will not be apparent to a viewer.

Another problem is that the fast Fourier Transform can only approximate its continuous counterpart. In particular, it is cyclical in nature. The integral in Equation (3.10) has infinite extent, but the transform can only be applied over a finite region. The FFT operates with the assumption that the contents of this region repeat endlessly across the plane. This means that a Fourier hologram will display not just the desired image, but an infinite series of duplicates stretching out to the sides (Figure 3.6). To prevent these extra images from interfering with the appearance of the hologram, we need to extend the limits of the sampling array representing the object by adding zeroes around the edges, so as to make it large enough that the duplicates are moved out of view. This can significantly increase the computation time.

3.4.2 Fresnel holograms

The problems associated with the large distance between the objects and the hologram were greatly alleviated by moving to the Fresnel regime. The Fresnel approximation [45, Ch. 4] assumes that

$$R^3 \gg \frac{\pi}{4\lambda}\max_{s,h}\left[(x_h - x_s)^2 + (y_h - y_s)^2\right]^2. \tag{3.11}$$

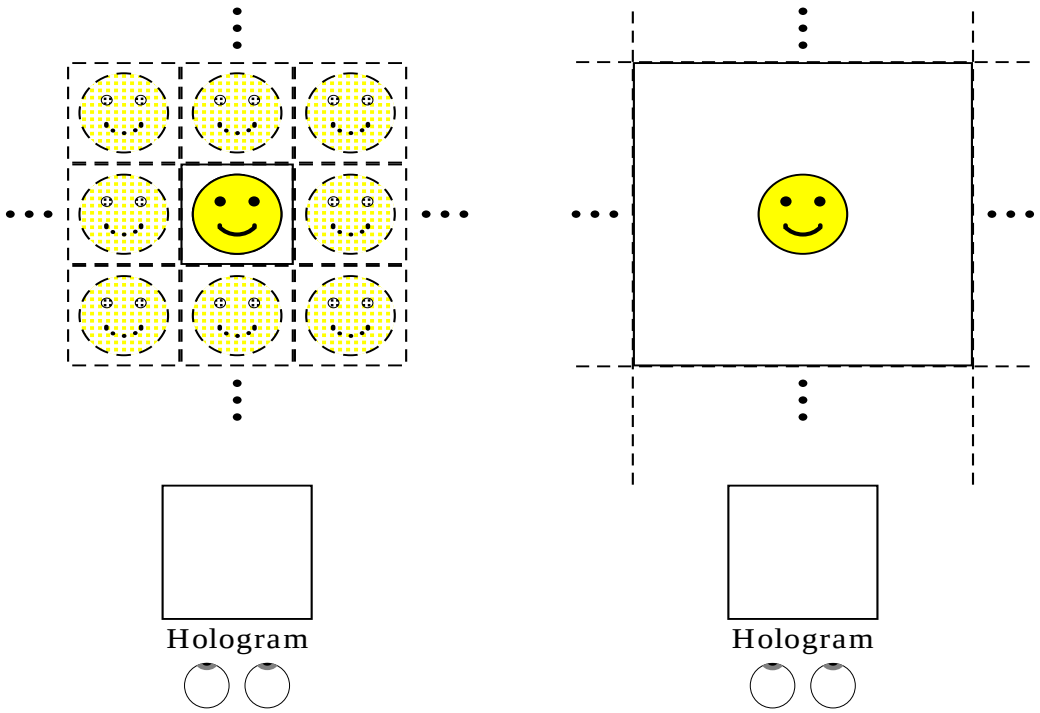

(a) Without zero padding **(b)** With zero padding

Figure 3.6: An illustration of image repetition in a Fourier hologram. Without zero padding, the viewer sees multiple copies of the objects. With zero padding, the extra images are pushed out to the sides so that they don't interfere with the main image.

This allows us to replace the spherical waves of Equation (3.5) by quadratic wavefronts. Using this approximation, Equation (3.5) becomes

(3.12)
$$\boldsymbol{F}(x_h, y_h) = \frac{e^{ikR}}{i\lambda R}\, e^{i\frac{k}{2R}(x_h^2+y_h^2)} \iint \boldsymbol{F}(x_s, y_s)\, e^{i\frac{k}{2R}(x_s^2+y_s^2)}\; e^{-i\frac{2\pi}{R\lambda}(x_h x_s + y_h y_s)} dx_s dy_s$$

(3.13)
$$= \frac{e^{ikR}}{i\lambda R}\, e^{i\frac{k}{2R}(x_h^2+y_h^2)} \mathcal{F}^{-1}_{(x_s,y_s)} \left\{ \boldsymbol{F}(x_s, y_s)\, e^{i\frac{k}{2R}(x_s^2+y_s^2)} \right\} \left(\frac{x_h}{R\lambda}, \frac{y_h}{R\lambda} \right).$$

This is identical to Equation (3.10), but for the additional quadratic phase factor within the integral. It can still be computed using an FFT, but now we take the transform of the light across the object multiplied by this phase factor. Computer-generated Fresnel holograms will suffer from the same repeti-

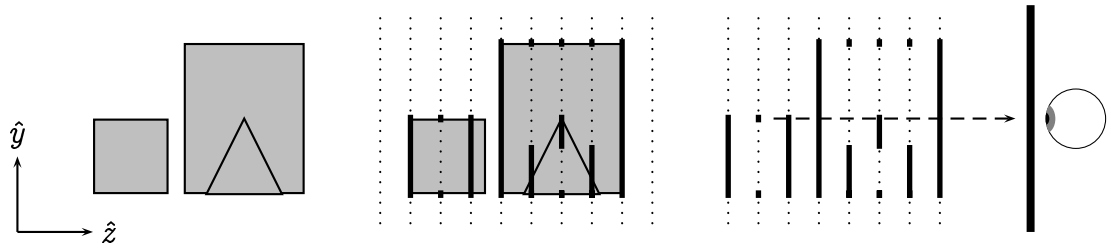

(a) Objects **(b)** Depth planes **(c)** Projection

Figure 3.7: A Fresnel hologram using multiple planar objects to simulate a three-dimensional scene. The objects are projected onto the nearest depth plane, and the hologram is computed by adding the holograms that would be produced by each of these planes individually.

tion problems as Fraunhofer holograms, requiring zero-padding, but the depth problems are greatly reduced.

For a typical hologram, Equation (3.11) requires that R be at least five meters. This is quite large, but is significantly less than the two kilometers needed for the Fraunhofer holograms. Lenses will still be necessary in the reconstruction process, but now a limited amount of depth effect will be visible. This allows holograms with several objects at different depths to be created by adding the results of multiple applications of Equation (3.13) [72, 120, 121].

This process introduces a new problem: how to produce holograms of arbitrary three-dimensional scenes using an algorithm meant only for two-dimensional objects lying parallel to the hologram plane. Two issues are involved: computing holograms of objects which are not parallel to the hologram; and computing holograms where near objects occlude farther ones.

The first method [73] used to handle non-parallel objects is illustrated in Figure 3.7. The scene is divided into several slices at different depths. Within each of these slices, the object surfaces are orthographically projected onto a

single plane. Equation (3.13) is then applied to each of these planes, and the results are summed to get the complete hologram.

This technique works well provided a sufficient number of slices are used so that the discrete depths appear continuous. If only a few depth planes are used, then the viewer will be able to see the individual slices, and the objects will not appear realistic. However, the time required, $O(N_R N_o {N_\delta}^2 \log N_\delta)$, is linearly dependent on the number of planes, N_R, so a hologram with a large number of planes will be computationally expensive.

This problem was solved when Leseberg and Frére [71] showed how Equation (3.13) could be modified to handle arbitrarily inclined planar objects. In addition to the FFT, an interpolation step is used to transform the light from the space of the inclined plane to hologram space. The extra step does not increase the computational complexity. We can now compute a hologram of any scene that can be represented solely by a set of polygons, using only one FFT and interpolation operation per polygon, so the complexity is now reduced back to $O(N_o {N_\delta}^2 \log N_\delta)$.

Both the multiplane and tilted plane techniques deal with multiple surfaces by adding the holograms each would individually produce. This prevents consideration of any occlusion that would normally be present, allowing far objects which should be blocked out by near ones to instead be visible through them. Ichioka et al. [53] showed how the first of these methods could be modified, without increasing the computational complexity, to cause the depth-planes to occlude those behind them. The technique can theoretically be applied to the algorithm used by Leseberg and Frère, but would require a series of repeated interpolation steps which would seriously degrade the final image. Thus, we

cannot get occlusion without the increased cost of the depth-plane method.

3.4.3 Image plane Fourier holograms

Although Fresnel holograms provide limited depth effects, the large distance needed between the objects and hologram is still restricting. Several recent papers [69, 113, 114] showed how Fourier holography could be applied to arbitrary planar objects, regardless of their distance to the hologram. The work described in these papers represents the state of the art in Fourier holography. It will be discussed in more detail in Chapter 6. For now, we simply note its advantages and disadvantages.

The papers provide an algorithm which can render scenes composed of arbitrary polygonal objects, regardless of their distance to the hologram, even if they intersect the film plane. It operates in $O(N_o {N_\delta}^2 \log N_\delta)$ time. However, by itself, the algorithm cannot handle occlusion. The occlusion method of Ichioka et al. can be applied, but, as in the case of Fresnel holograms of tilted planes described in the previous section, not without degrading the image quality. Furthermore, these holograms also suffer from the same unwanted image repetition as FFT implementations of Fraunhofer and Fresnel holograms. In fact, even more zero-padding will be needed here, because the tilted planes will have more duplicate images within the field of view. Because of these drawbacks, Fourier holography does not appear to provide the solution to rendering realistic scenes.

3.5 Horizontal parallax only holograms

As we move through the real world, our eyes usually lie in a horizontal plane, and our motions are predominantly horizontal as well. We therefore come to depend far more on horizontal parallax than on vertical parallax. For many three-dimensional display applications, this fact allows us to entirely eliminate vertical parallax without adversely affecting the appearance or utility of the display device. For a computer generated hologram, this not only greatly reduces the computational complexity, but also reduces the amount of data that must be stored and displayed.

Optically generated *horizontal parallax only* (HPO) holograms, also known as *rainbow holograms* [3, 15, 25], were first introduced by Stephen Benton as a step towards the development of a holovideo system [8]. They have since found wider application because of their ability to be viewed in white light and their suitability for mass production. The term *rainbow hologram* is due to the fact that this type of hologram exhibits a characteristic color shifting as the observer moves vertically.

Conceptually, the computation of an HPO hologram [70, 83, 84] is quite simple. The scene and hologram are divided into some number of horizontal slices, as shown in Figure 3.8. Each slice of the hologram is treated as an independent, one-dimensional hololine, which only receives light from the corresponding slice of the scene. Each hololine is therefore only capable of reproducing this one slice of the scene, destroying the vertical parallax. However, within each slice, every point on the hololine receives light from every object point, so full horizontal parallax is maintained.

The reconstruction of an HPO hologram is shown in Figure 3.9. Each holo-

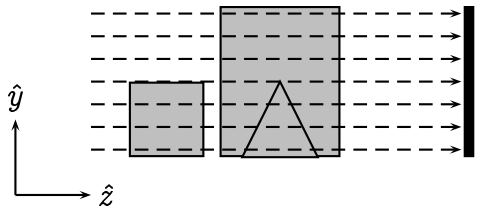

Figure 3.8: The computation of an HPO hologram. Each horizontal line of the hologram receives light only from object points at the same height.

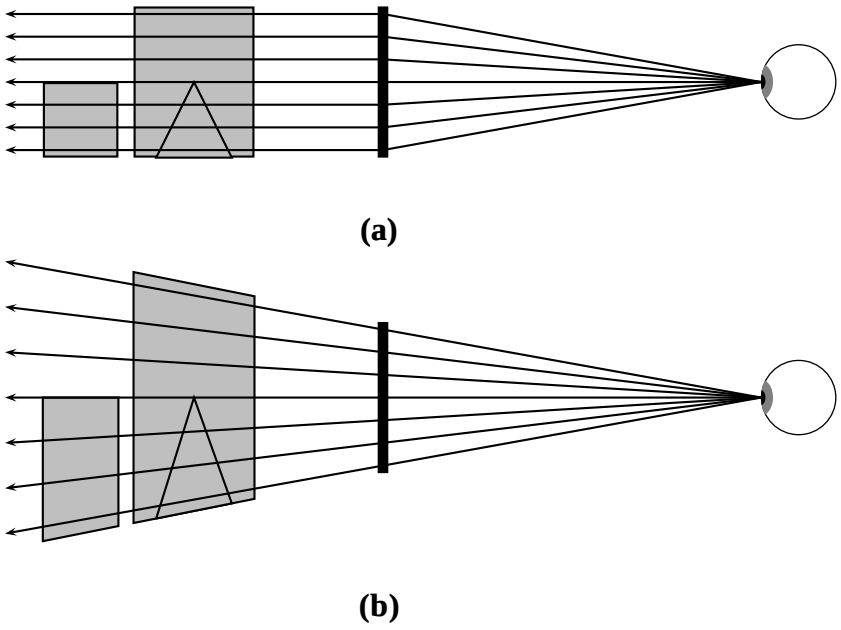

Figure 3.9: Reconstruction of an HPO hologram. (a) shows that the light appears to be bent by the hologram so that a viewer looking at a point on the hologram will see the light given off by the part of the object at the same height. (b) shows the image as it appears to the viewer.

line produces an image of the corresponding slice of the hologram, which it projects uniformly in all directions. Thus no matter what the height at which the user is positioned, the entire hologram will be visible, although the image will be shifted and distorted depending on this position. This distortion is exaggerated here for the purposes of illustration. It is normally not as pronounced, and does not interfere with the appearance of the hologram.

Because the vertical parallax has been eliminated, it is no longer necessary to sample the hologram at near wavelength scale in the vertical direction. A resolution on the order of that of an ordinary CRT display is satisfactory. We define Δ to be the new vertical spacing, and note that it is several orders of magnitude larger than δ. The number of vertical samples becomes $N_\Delta \equiv \frac{D}{\Delta}$. Modifying equation Equation (3.6) to integrate only in the horizontal direction, we find that the hologram can be computed in $O({N_o}^2 N_\Delta {N_\delta}^2)$ time, significantly less than the $O({N_o}^2 {N_\delta}^4)$ required for full parallax. In addition, the use of HPO holograms can be combined with other techniques, such as Fourier holography [66], to reduce the complexity even further.

This method is not without its drawbacks. First of all, there is the obvious fact that the holograms lack vertical parallax, as well as the slight image distortion mentioned above. A second and more subtle problem is the fact that HPO holograms cannot focus light vertically. This produces an astigmatism effect which increases with the object depth. The human visual system can only tolerate a certain amount of astigmatism, so the usable depth of an HPO hologram at which fine focus can be achieved will be limited [85, pg. 26]. Nevertheless, HPO holograms are perfectly suitable for a wide range of applications, and because of their relative computation speed and lower data size, the first few generations

of commercial holographic displays are likely to use this technique.

3.6 Holographic stereograms

First developed as a means of producing holograms of large, naturally illuminated scenes, holographic stereograms [89] provide a simple and computationally inexpensive means of producing computer generated holograms. Figure 3.10 shows a simplified overview of the optical generation of a holographic stereogram. The apparatus and geometric layout for this process can vary widely, but the general principles remain the same. A series of photographs are taken of the scene by a camera moving along a guide rail. The photographs are then projected, using a coherent light source, onto a translucent screen one at a time, and each one is used as the object to produce a thin strip of the hologram. Someone looking through the n^{th} strip will see an image of the photograph taken at the n^{th} position. Thus, someone looking at the hologram as a whole will see a series of images, each taken from a slightly different position, which will combine to produce an illusion of three-dimensionality. The effect is similar to that of the lenticular screen stereograms described in Chapter 2, but holographic stereograms can provide views from many more discrete positions.

This method can easily be adapted to computationally modeled scenes by substituting computer generated images for the photographs [48, 57]. Any suitable computer graphics software can be used to render the images. They can then be transferred to film, and combined in a hologram using the same apparatus as before. The hardware can be eliminated by computing the hologram strips directly from the rendered images using FFTs or other algorithms [90,128].

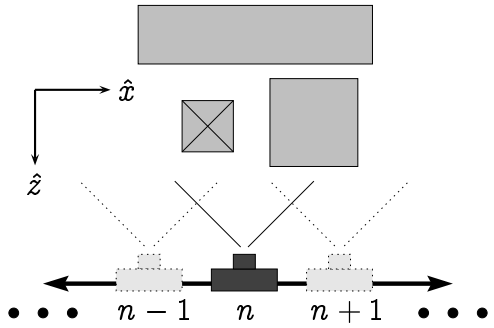

(a) Recording of images

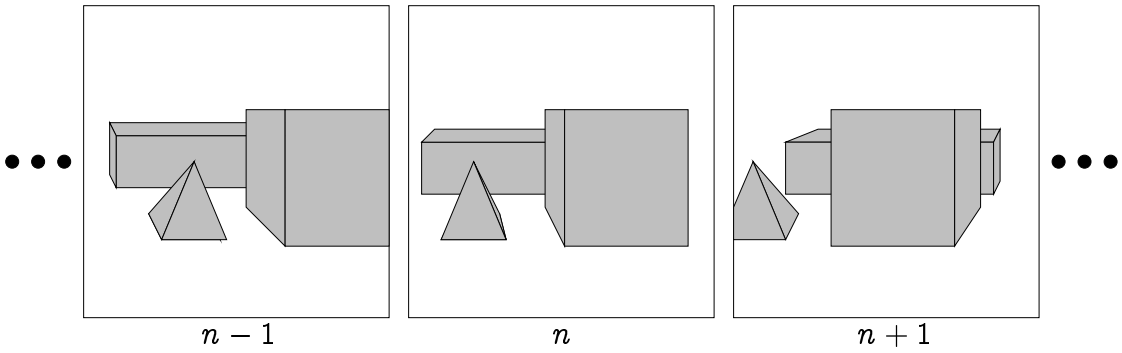

(b) Image set

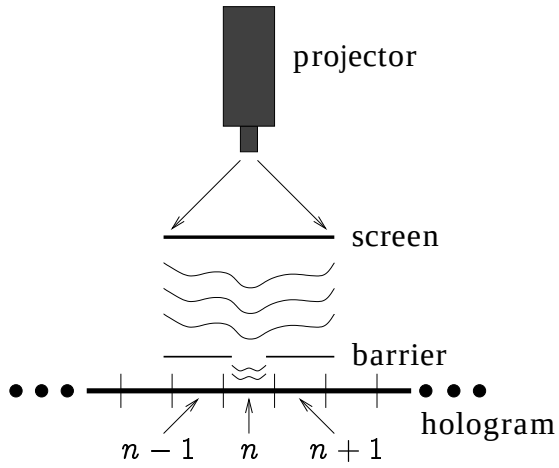

(c) Construction of hologram

Figure 3.10: Creation of a holographic stereogram. A series of photographs are taken of the scene. These photographs are then projected onto a screen, and a thin hologram is made of each of the images.

There is a sharp contrast between this method and those described in the preceding sections. In Sections 3.3 and 3.4, approximations were made in the structure of the objects, but we still attempted to accurately simulate the propagation and interference of light which produces the hologram. In Section 3.5, we subdivide the world into some number of independent slices, but within each slice we again still try to accurately simulate the interference. In the holographic stereogram, on the other hand, we are less concerned with the process that forms the hologram than we are with it's appearance to an observer. Recalling the discussion about particle vs. wave models at the beginning of this chapter, we see that the holographic stereogram method performs part of the computation (i.e. generating the images) using the particle model, and then switches to the wave model to produce the hologram. As was noted, computation can be done far more efficiently with the particle model than the wave model. This accounts for the great increase in speed offered by the stereogram.

3.7 Diffraction specific computation

In this section, we will discuss a particular holographic stereogram algorithm called *diffraction specific computation*, developed by Mark Lucente [85–87]. The name refers to the fact that the focus is on how the light is diffracted by the hologram, in contrast to *interference based computation*, which focuses on the interference phenomena which forms the hologram. Lucente described an efficient method for computing holographic stereograms and showed how existing graphics hardware could be adapted to aid in the computation process. In addition, his method also provides some simple data compression. In discussing

this work, we will take a different approach than that used by Lucente, describing it in somewhat more general terms and defining our own notation, in order to more easily build upon it in the following chapters.

3.7.1 Lumigraph

We begin by taking a brief look at two papers on two-dimensional rendering. These papers, one by Levoy and Hanrahan [74] and the other by Gortler et al. [46], appeared at the same time and describe very similar algorithms. These algorithms belong to a class known as *image-based rendering*, which uses photographs or pre-computed images from a finite number of positions to generate views from any desired position.

A camera plane and a focal plane are defined in space, as shown in Figure 3.11. Levoy and Hanrahan parameterized these planes by (s,t) and (u,v), respectively. Gortler et al. used the reverse of this notation. We will choose to parameterize the camera plane by (s,t) and the focal plane by (U,V). The reason for this decision will become clear in Chapter 5. Any ray from the camera plane that passes through the focal plane can be represented by the pair of points at which it intersects the two planes. Therefore, these coordinate pairs can be used to parameterize the light passing through the camera plane in any forward direction, defining a function $L(s,t,U,V)$. By discretizing this domain, we can store information about the light as a four-dimensional array. Levoy and Hanrahan referred to this construction as a *light field*, while Gortler et al. called it a *lumigraph*. We prefer the latter term because it emphasizes it's relation to a hologram.

The two papers describe methods for computing the lumigraph directly or

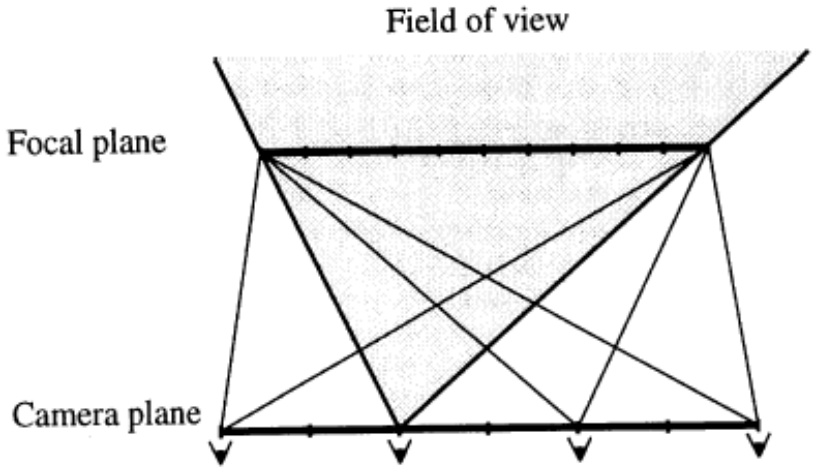

Figure 3.11: A light field / lumigraph. (figure taken from [74])

producing it by resampling photographic data. Once this array has been fully computed, it can be used to interpolate the view seen from an point in free space behind the camera plane. The quality of the images obtained will depend on how finely the 4D space is sampled.

This ability to render a scene from an arbitrary position without reference to the scene itself is very similar to what a hologram provides. In fact, a lumigraph contains all the information that we desire from a hologram. This is *not* to say that it comes close to the information content of a real hologram of the scene. The methods used to compute a lumigraph do not even begin to approximate the complex light propagation that produces a hologram. However, our real concern is not with producing physically accurate simulations of the underlying physical phenomena so much as with producing perceptually correct images. From this standpoint, the lumigraph provides a sufficient representation of the light, while being far easier to compute and compress. All that is needed is a way to convert this construct to a holographic interference pattern.

3.7.2 Hogel representation

This is, in essence, what Lucente [85] provides: a means for converting a lumigraph into a hologram. It should be noted that this work predates the light field and lumigraph papers, but we will discuss it in terms of these papers because they provide a more familiar framework for members of the computer graphics community. Before we discuss how his algorithm works, we need to define some symbols and terminology.

We begin by noting that while traditional 2D rendering algorithms compute the intensity of light, holograms are computed in terms of the magnitude of the electromagnetic field, which is proportional to the square root of the intensity. Therefore, from this point on, whenever we discuss a lumigraph L, we will actually be referring to the square root of the quantities calculated in the light field and lumigraph papers.

The two-plane parameterization used in the light field and lumigraph papers was chosen because it allowed efficient resampling to render new views. However, it is less well suited to our needs. Instead, we will parameterize the light as $L(s,t,\theta,\phi)$, where $\vec{s} = (s,t)$ is the position on the camera plane and $\vec{\omega} = (\theta,\phi)$ is the direction of the incoming light. We will derive a correspondence between the directional variation of L at a given point (s,t) on the camera plane and the value of $\boldsymbol{F}$ in the neighborhood of the point $(x_h, y_h) = (s,t)$ on the hologram.

We discretize the camera plane using a regular grid with sample spacing d, and similarly divide the hologram into square regions of this size. Recall that in Section 3.2, we defined the size of the hologram to be D, and the sample spacing to be δ. The new distance d will be small compared to D, but still quite

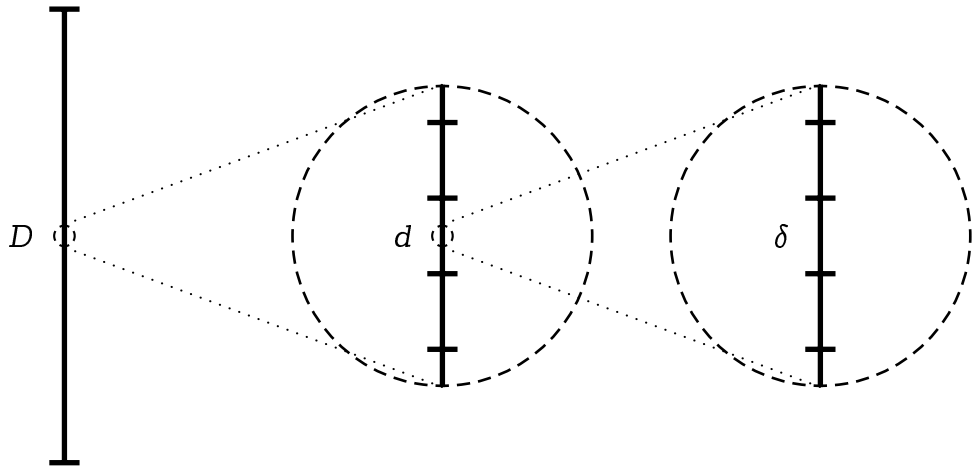

Figure 3.12: A hogel consists of many sample points but is still much smaller than the hologram

large compared to δ (Figure 3.12). Lucente referred to these subsections of the hologram as *hogels*, for "*ho*log*r*aphic *el*ement*s*".

We define $n_\delta \equiv \frac{d}{\delta}$ to be the one-dimensional number of samples per hogel and $N_d \equiv \frac{D}{d}$ to be the number of hogels along one dimension of the hologram. Note that $N_\delta = N_d \times n_\delta$. Since the hogels are two-dimensional, there are ${n_\delta}^2$ total samples per hogel and ${N_d}^2$ hogels in the hologram.

In addition, we assume that we have some discretization of $\vec{\omega}$ which provides roughly uniform angular sample spacing of ϑ. Each sample covers a solid angle of approximately $\pi \sin^2 \frac{\vartheta}{2}$, so if the viewing frustum has half-angle Θ, and assuming ϑ is small enough that $\sin(\vartheta) \approx \vartheta$, then there are $n_\vartheta \equiv 2\pi(1 - \cos\Theta)/(\frac{\pi}{4}\vartheta^2) = \frac{8(1-\cos\Theta)}{\vartheta^2}$ sample directions. The total number of samples in the lumigraph is therefore $N_\vartheta = {N_d}^2 n_\vartheta = \frac{8D^2(1-\cos\Theta)}{d^2\vartheta^2}$.

Lucente provides upper bounds on these resolutions based on the limits of the human visual system. Let R be the distance from which a hologram will

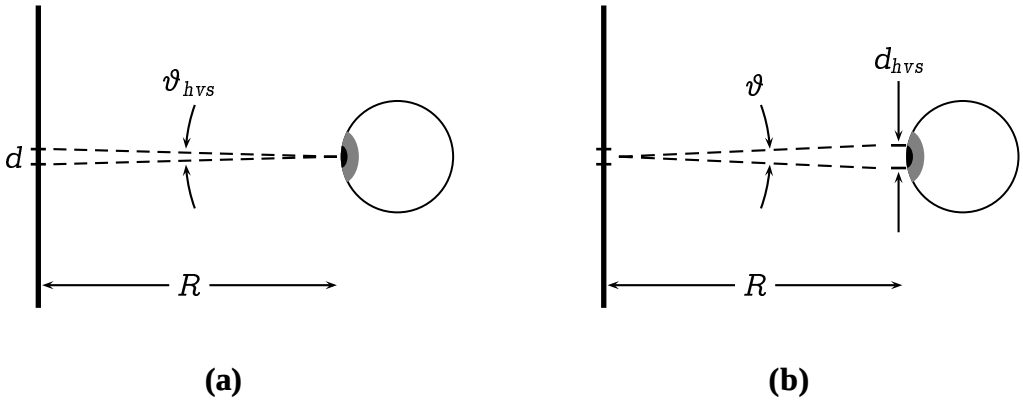

Figure 3.13: The usable resolution of a hogel representation is limited by properties of the human visual system: (a) the angular resolution of the eye; (b) the size of the pupil.

typically be viewed, and let ϑ_{hvs} and d_{hvs} be the angular resolution and pupil width of the human eye, as shown in Figure 3.13. Then a spatial sampling less than $d \gtrsim R\vartheta_{hvs}$ will produce features too small to be discernible, while an angular sampling smaller than $\vartheta \gtrsim \frac{d_{hvs}}{R}$, will be blurred out by the eye's aperture. At this sampling rate, the total number of samples becomes $N_\vartheta \lesssim \frac{8D^2(1-\cos\Theta)}{d_{hvs}^2\vartheta_{hvs}^2}$.

Average values for d_{hvs} and ϑ_{hvs} are approximately 3mm and $1'$ respectively, and typical values for R and Θ would be about 0.5m and $45°$. This yields $d \gtrsim 0.1$mm and $\vartheta \gtrsim 20'$. The number of samples required for a one square centimeter lumigraph would be $N_\vartheta \lesssim 3 \times 10^8$. This is already about one tenth of the number of samples required for a hologram with the same frustum. Of course, this is merely an upper bound. In general, it is possible to use significantly larger sample spacing, and correspondingly fewer samples, without perceptibly affecting the quality of the resulting images.

3.7.3 Conversion to an interference pattern

Lucente's research dealt primarily with horizontal parallax only holograms. Although his algorithms are equally applicable to the full parallax case, as will be discussed later, this restriction happens to be useful for the purposes of an introductory discussion. For the remainder of this chapter, we will consider the task of converting a one-dimensional lumigraph to a hololine. We restrict our attention to a fixed point s in the lumigraph $L(\theta, s)$ and the corresponding hogel in the hologram $\boldsymbol{F}(x_h)$, which lies in the range $s - \frac{d}{2} \leq x_h \leq s + \frac{d}{2}$. For simplicity, we shift our frame of reference so that $s = 0$, and use $L(\theta)$ to indicate the directional variation of the lumigraph at this point. Our goal is to find a transform $\mathcal{T}$ which generates an interference pattern across this region whose emission matches the desired lumigraph:

$$\boldsymbol{F}(x_h) = \mathcal{T}_\theta \left\{ L(\theta) \right\} (x_h) . \tag{3.14}$$

To develop this transform, we consider the inverse problem. Suppose we are given a field $\boldsymbol{F}(x_h)$ which is non-zero only in the range $-\frac{d}{2} \leq x_h \leq +\frac{d}{2}$. Then the light received by an observer at some point $\vec{x}_p$ in space is

$$\boldsymbol{F}(\vec{x}_p) = \frac{1}{i\lambda} \int \boldsymbol{F}(x_h) \frac{e^{i2\pi \frac{r}{\lambda}}}{r} (\hat{z} \cdot \hat{r}) \, dx_h, \tag{3.15}$$

where $\vec{r}$ is the vector from $\vec{x}_h$ to $\vec{x}_p$ (Figure 3.14(a)).

We know that the distance from which the hologram will be viewed is large compared to the hogel size, so we can represent $\vec{x}_p$ by a distance R and direction θ from the center of the hogel (Figure 3.14(b)), and, using approximations similar to those in Section 3.4, Equation (3.15) becomes

$$\boldsymbol{F}(\vec{x}_p) = \frac{e^{i2\pi \frac{R}{\lambda}}}{R} \frac{\cos\theta}{i\lambda} \int \boldsymbol{F}(x_h) \, e^{-i2\pi \frac{x_h \sin\theta}{\lambda}} dx_h, \tag{3.16}$$

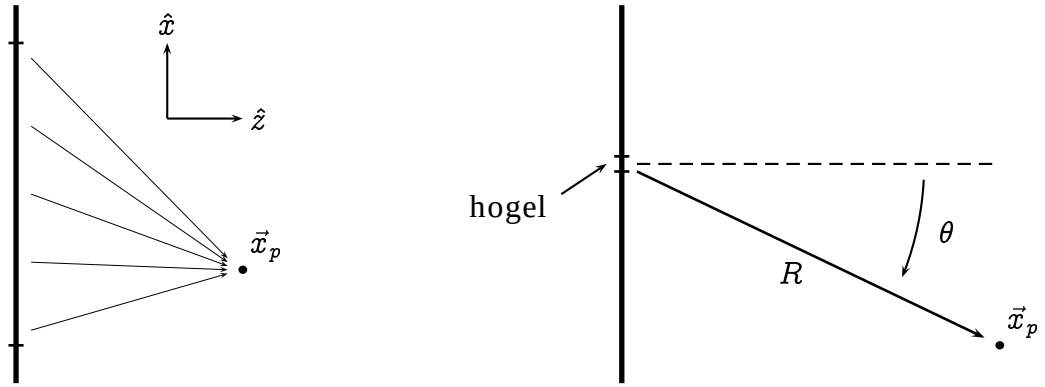

(a) Near field **(b)** Far field

Figure 3.14: To determine the light near the hogel, the contribution from every point must be summed. At larger distances, the hogel can be treated as a point source with a directionally non-uniform emission pattern.

This equation can be separated into independent functions of R and θ:

$$\begin{aligned} \boldsymbol{F}(\vec{x}_p) &= \boldsymbol{F}_R(R)\boldsymbol{F}_\theta(\theta) \\ \boldsymbol{F}_R(R) &= \frac{e^{i2\pi\frac{R}{\lambda}}}{R} \\ \boldsymbol{F}_\theta(\theta) &= \frac{\cos\theta}{i\lambda}\int \boldsymbol{F}(x_h)\, e^{-i2\pi\frac{x_h \sin\theta}{\lambda}} dx_h \end{aligned} \tag{3.17}$$

The R component is simply the function for a point light source, so, to an observer at a large enough distance, the hogel acts like a point source with a directionally non-uniform emission, which is exactly the behavior we expect from a point on a lumigraph. Therefore, the θ part of Equation (3.17) corresponds to $L(\theta)$.

We can now define

$$\boldsymbol{L}(\theta) = \mathcal{T}_{x_h}^{-1}\left\{\boldsymbol{F}(x_h)\right\}(\theta) \equiv \frac{\cos\theta}{i\lambda}\int \boldsymbol{F}(x_h)\, e^{-i2\pi\frac{x_h \sin\theta}{\lambda}} dx_h. \tag{3.18}$$

Note that the quantity $\boldsymbol{L}$ above is complex-valued, while a lumigraph L is only real-valued. In order to convert a lumigraph to an interference pattern, we will

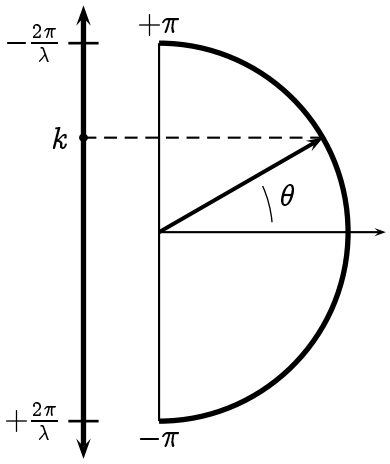

Figure 3.15: There is a direct correspondence between the frequency space decomposition of the light across the hogel and its far-field directional emission. For a given point in frequency space, the corresponding direction vector can be found by mapping the point onto the base of a hemicircle and projecting onto the circle.

need to first transform it into a complex function by multiplying by a phase factor, so that $\|\boldsymbol{L}\| = L$. This phase factor can be chosen randomly, or it can be used to add additional constraints which make the interference pattern better behaved [85].

A closer examination of Equation (3.18) reveals that the integral part is an inverse Fourier transform of $\boldsymbol{F}$ evaluated at $\frac{\sin\theta}{\lambda}$:

$$\mathcal{T}_{x_h}^{-1}\left\{\boldsymbol{F}(x_h)\right\}(\theta) = \frac{\cos\theta}{i\lambda}\mathcal{F}_{x_h}^{-1}\left\{\boldsymbol{F}(x_h)\right\}\left(\frac{\sin\theta}{\lambda}\right). \tag{3.19}$$

This indicates that there is a direct correlation between the directional variation of light emitted by the hogel and its representation in frequency space. This is illustrated in Figure 3.15. If we map the spatial frequency domain $-\frac{2\pi}{\lambda} \leq k \leq +\frac{2\pi}{\lambda}$ to points along the diameter of a hemicircle, and the directional domain $-\pi \leq \theta \leq +\pi$ to angles from its center, then we can convert from one domain to the other by projecting orthographically.

Now, suppose that we have sampled the hogel at n_δ points, $x_i = i \cdot \delta$, to obtain an array $\boldsymbol{F}_i = \boldsymbol{F}(x_i)$, and that we wish to obtain the value of $\boldsymbol{L}$ at some set of discrete angles θ_j. The integral in Equation (3.18) becomes a summation

$$\boldsymbol{L}_j = \boldsymbol{L}(\theta_j) = \frac{\delta \cos\theta_j}{i\lambda} \sum_i \boldsymbol{F}_i \, e^{-i2\pi \frac{x_i \sin\theta_j}{\lambda}}. \tag{3.20}$$

Since Equation (3.18) can be written as an inverse Fourier transform, we should be able to compute Equation (3.20) as a discrete Fourier transform as long as we choose the sample points so that the summation matches that in the definition of the inverse DFT (Equation (3.4)). That is,

$$\boldsymbol{L}_j = \frac{\delta \cos\theta_j}{i\lambda} \mathcal{F}_i^{-1} \left\{ \boldsymbol{F}_i \right\}_j = \frac{\delta \cos\theta_j}{i\lambda} \sum_i \boldsymbol{F}_i e^{-i2\pi \frac{ij}{n_\delta}}. \tag{3.21}$$

Combining Equations (3.20) and (3.21) we have

$$\begin{aligned} \frac{x_i \sin\theta_j}{\lambda} &= \frac{ij}{n_\delta} \\ \frac{i\delta \sin\theta_j}{\lambda} &= \frac{ij}{n_\delta} \\ \theta_j &= \arcsin\left(\frac{j\lambda}{\delta n_\delta}\right) = \arcsin\left(\frac{j\lambda}{d}\right). \end{aligned} \tag{3.22}$$

Using this sampling for θ, we now have an expression for the inverse of $\mathcal{T}$ in terms of the inverse Fourier transform. We can invert it to obtain the desired transform

$$\mathcal{T}_j \left\{ \boldsymbol{L}_j \right\}_i = \frac{i\lambda}{\delta} \mathcal{F}_j \left\{ \frac{\boldsymbol{L}_j}{\cos\theta_j} \right\}_i, \tag{3.23}$$

which can be computed with an FFT. Note that for $|j| > \frac{d}{\lambda}$, θ_j is undefined. We define the function values at these sample points to be zero.

3.7.4 Hogel basis functions

Instead of computing $\boldsymbol{F}$ from L via a direct application of Equation (3.23), Lucente proposed an alternative method. He defined a set of piecewise constant

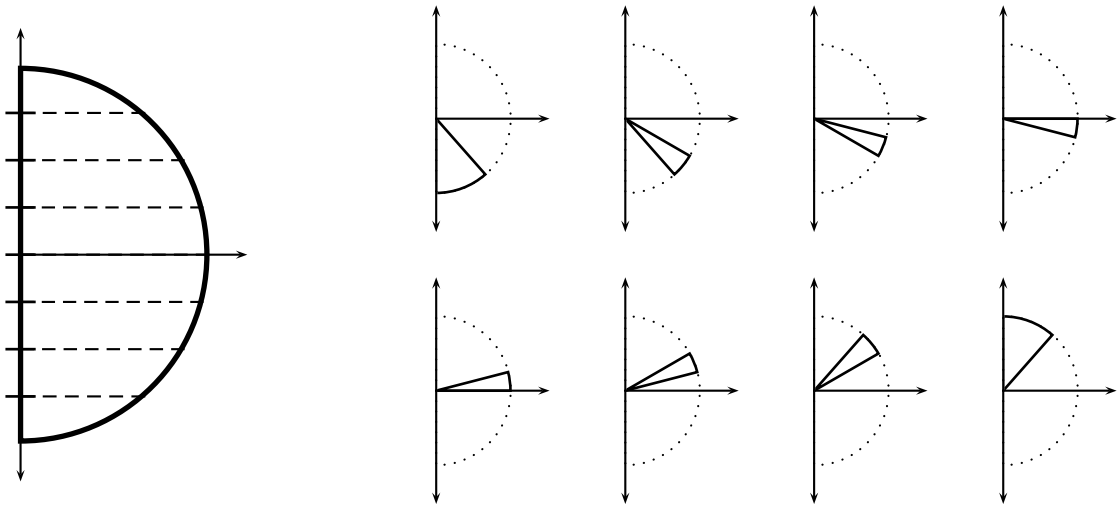

Figure 3.16: Lucente's basis functions with $n_\xi = 8$. Frequency space is divided into equal portions, each corresponding to a set of incoming directions which can be found by projecting onto the unit hemicircle (as shown on the left). Each basis function has a value of 1 over one of these regions and 0 elsewhere (as shown on the right).

basis functions, which we will call $\xi_m(\theta)$, over the directional hemicircle, as illustrated in Figure 3.16. These functions are defined by uniformly dividing frequency space into n_ξ regions and projecting them onto the hemicircle. Each function $\xi_m(\theta)$ has a value of one over the m^{th} region and zero elsewhere. Using this basis, a lumigraph can be represented by a vector of coefficients $[c_m]$, such that $L(\theta) \approx \sum c_m \xi_m(\theta)$. Lucente referred to $[c_m]$ as a *hogel vector*.

For each of these basis functions, we can compute a corresponding interference pattern $\Xi_m(x) = \mathcal{T}_\theta \{\xi_m(\theta)\}(x)$. Lucente called these *basis fringes*. This can be done as a pre-process, and the results can then be placed in permanent storage. Given a hogel vector corresponding to some L, we can now compute the

interference pattern as the weighted sum

$$\boldsymbol{F}_i = \sum c_m \Xi_{m,i}. \tag{3.24}$$

This method provides several advantages over computation via FFT. First, as noted earlier, $L(\theta)$ can be accurately represented with far fewer samples than $\boldsymbol{F}(x)$. However, evaluating Equation (3.23) with an FFT requires the same number of samples for both L_j and $\boldsymbol{F}_i$, forcing us to do extra work in computing the lumigraph, which can be avoided with Lucente's method.

Second, computation with Equation (3.23) requires $O(n_\delta \log n_\delta)$ time, while Equation (3.24) requires $O(n_\delta n_\xi)$. For $n_\xi \lesssim \log n_\delta$, $\boldsymbol{F}_i$ can be computed more rapidly by summation than FFT. By taking advantage of existing specialized hardware, such as an accumulation buffer [31,47,122], the savings become even greater.

Finally, the hogel vector provides a much more compact representation than the sampled interference pattern. By decreasing n_ξ, we can compress the data as much as desired, albeit at the cost of accuracy.

Using this algorithm, Lucente was able to produce small, HPO holograms in near real-time. In the following chapters, we will build on this, extending it to full parallax, improving the compression characteristics, and decreasing the computation time.

Chapter 4

Representation and Compression

In the previous chapter, we derived equations to convert between a point in a one-dimensional lumigraph and a holographic line segment. To handle the more general case of full-parallax holograms, we must extend these equations to 2D. The lumigraph at a single point now becomes $L(\theta, \phi)$, and the interference pattern across the corresponding region of the hologram is $\boldsymbol{F}(x, y)$. These functions are sampled at spatial and directional points:

$$\begin{aligned} \vec{x}_{\vec{i}} &\equiv (i_1 \cdot \delta, i_2 \cdot \delta) \\ \vec{\omega}_{\vec{j}} &\equiv (\theta_{\vec{j}}, \phi_{\vec{j}}) \\ &\equiv \left(\arcsin\left(\|\vec{j}\| \, \frac{\lambda}{d} \right), \arctan\left(\frac{j_2}{j_1} \right) \right) \end{aligned} \tag{4.1}$$

The transforms become

$$\boldsymbol{F}_{\vec{i}} = \mathcal{T}_{\vec{j}} \{ \boldsymbol{L}_{\vec{j}} \}_{\vec{i}} \equiv \frac{i\lambda}{\delta} \mathcal{F}_{\vec{j}} \left\{ \frac{\boldsymbol{L}_{\vec{j}}}{\cos\theta_{\vec{j}}} \right\}_{\vec{i}} \tag{4.2}$$

$$\boldsymbol{L}_{\vec{j}} = \mathcal{T}_{\vec{i}}^{-1} \{ \boldsymbol{F}_{\vec{i}} \}_{\vec{j}} \equiv \frac{\delta \cos\theta_{\vec{j}}}{i\lambda} \mathcal{F}_{\vec{i}}^{-1} \{ \boldsymbol{F}_{\vec{i}} \}_{\vec{j}} \tag{4.3}$$

With the added sampling dimension introduced by moving to the full parallax case, efficient compression becomes even more important. In this chapter,

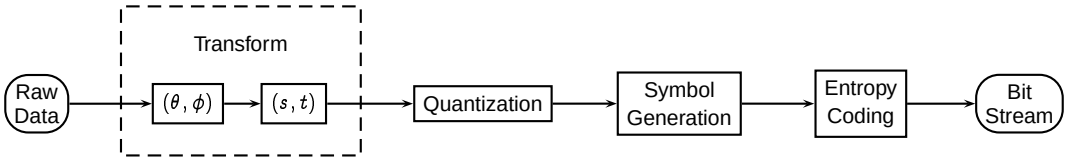

(a) Lumigraph compression

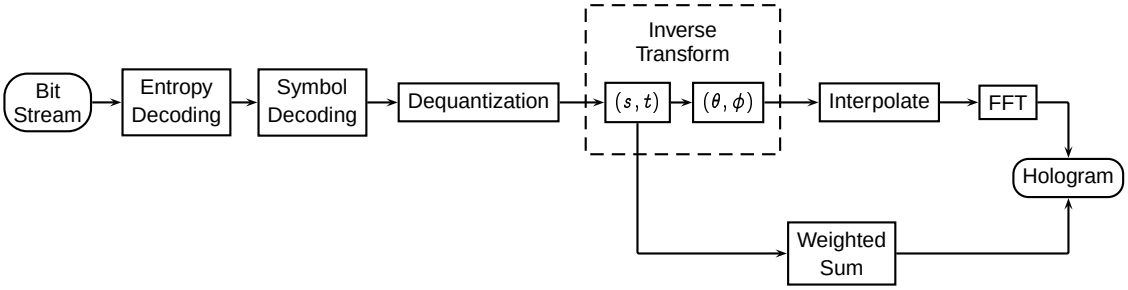

(b) Two possible ways to convert to a hologram

Figure 4.1: Overview of lumigraph compression and conversion to holographic interference pattern

we will examine and compare several schemes for representing and compressing the lumigraph. We will seek to take advantage of coherence not only within each individual hogel, but also between adjacent hogels. That is, we will perform compression in the entire 4D space (s, t, θ, ϕ) of the lumigraph, instead of just the directional dimensions (θ, ϕ), as Lucente did.

The overall structure of our compression algorithm will follow fairly standard procedures (Figure 4.1(a)). First a linear transform is applied to the sampled data. Ideally, this transform should concentrate the information represented by the original data into only a few terms, leaving most of the transformed data entries negligible. Except for small roundoff errors, this transform is invertible and, in general, lossless. Next, the data is quantized to produce a set of integer coefficients. These coefficients are then compressed into a string of

symbols from one or more alphabets to encode large scale patterns in the data (such as blocks of zeros) into small sets of symbols. Finally, the symbols are converted into a string of bits such that the most common symbols require the least number of bits to represent.

The key to achieving a high compression ratio is the choice of transformation. A transform well-suited to the data can result in compression to a fraction of the original size, while a very poorly chosen transform can actually increase the storage requirements. In this chapter, we will discuss several possibilities for this choice. We will limit our attention to transforms which can be decomposed into two separate transforms, one operating on the directional, (θ, ϕ), dimensions, and the other on the spatial, (s, t), dimensions. In so doing, we may eliminate from consideration some very efficient compression schemes. However, this ensures that the lumigraph at every point is represented by a fixed set of basis functions, which is necessary if we wish to convert it to a hologram via Equation (3.24).

This conversion can take two possible paths, as seen in Figure 4.1(b). We begin by inverting the entropy coding, symbol generation, and quantization steps, as well as the spatial part of the transform step. At this point, one possibility is to also invert the directional transform, restoring the original data. We can then interpolate the data to the sample points required for an FFT, and apply Equation (4.2) to obtain the hologram. Alternatively, if we have a set of precomputed basis functions corresponding to the directional transform, then we can use Equation (3.24) to calculate the hologram via a weighted sum.

The choice of which of these methods to use depends largely on the characteristics of the chosen transform. The FFT has complexity $O(n_\delta{}^2 \log n_\delta)$, while

weighted sums is $O({n_\delta}^2 n'_\xi)$, where $n'_\xi \leq n_\xi$ is the number of non-negligible hogel vector coefficients. The cost of the interpolation step required for the FFT can vary widely depending on the sample points used by the transform. For a poorly chosen transform, we can have $n'_\xi \approx n_\xi \approx {n_\delta}^2$, making weighted sums very inefficient compared to the FFT. However, with a good transform, n'_ξ can become small enough to make weighted sums faster, especially where interpolation is expensive. This advantage can be further increased by the use of specialized hardware. While both Equation (4.2) and Equation (3.24) can be efficiently implemented in hardware, this may not be possible for the interpolation step.

In this chapter, we will provide the details of this flowchart. We will begin by discussing the sample space used to represent the lumigraph domain. Next we will describe a number of possible transforms which can be applied to the sampled data. We will then describe the quantization and encoding method which we developed to convert the transformed data into a compact bit stream. Finally, we will compare the compression ratios resulting from the various transforms to determine which ones are the most effective for our application.

4.1 Sampling domain

Before selecting a transform, we must first define the set of sample points over which it will be defined. We choose independent discretizations for the spatial and directional dimensions. For the (s,t) plane, we will use a regular Cartesian grid with sample spacing of d in the $\hat{s}$ direction and either d or Δ in the $\hat{t}$ direction depending on whether the parallax of the hologram is full or hori-

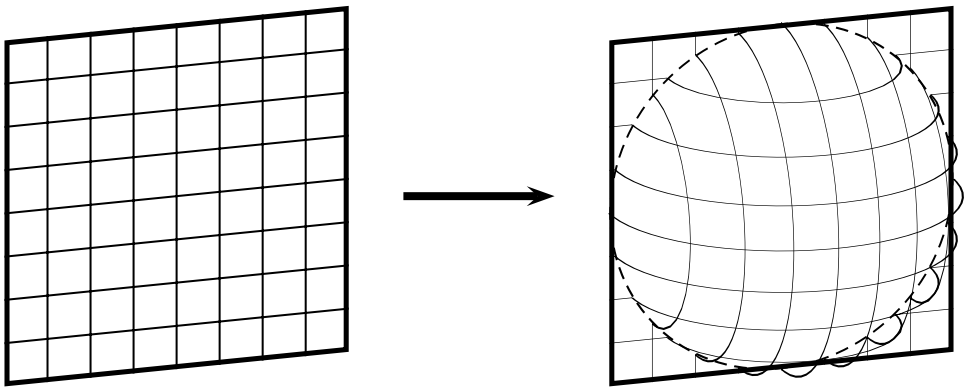

Figure 4.2: The directional dimensions of the lumigraph can be discretized using a regular frequency space subdivision and projecting onto the hemisphere.

zontal only. Although other discretizations of the plane are possible, this is the most natural, allows the widest variety of compression methods, and matches the parameterization of the display technology.

For the two directional dimensions, we have a number of options. The simplest choice is to use the $(\theta_{\vec{f}}, \phi_{\vec{f}})$ points defined in Equation (4.1). This is equivalent to a two-dimensional extension of the discretization used by Lucente. A uniform rectilinear grid is laid out in frequency space and then projected onto the directional hemisphere (Figure 4.2). As with the (s,t) discretization, this grid allows a wide variety of transforms to be applied to the data.

However, this method does not provide a good representation for functions over the hemisphere. As the figure shows, the coverage of the hemisphere is very non-uniform, with the sample spacing varying widely. About one fifth of the samples do not correspond to points on the hemisphere at all, and are therefore wasted.

Fortunately, this discretization is only required for the Fourier transform.

We are free to choose a different set of sample points for the lumigraph and, as discussed briefly above, perform an interpolation when it comes time to do the conversion. This extra step can add to the computational cost of the conversion, as well as introduce some small errors into the data, but these costs may be worth paying in exchange for better compression. Of course, if conversion is performed using weighted sums, then no interpolation will be necessary except when the basis fringes are computed as a preprocess.

We have chosen to use a hemicube representation for the directional dimensions (Figure 4.3). This provides significantly more uniform coverage of the hemisphere than the previous scheme, while maintaining the rectilinear structure. This mesh is easy to work with, allows rapid interpolation to the sample points of Equation (4.1), and should already be familiar to computer graphics programmers. In addition, it can readily be adapted to horizontal-parallax only holograms, by using a hemisquare, and to holograms with arbitrary viewing frusta, by adjusting the size of the side and front faces. In particular, for the common case of holograms with maximum viewing angle Θ equal or less than 45 degrees, the side faces can be completely eliminated, and the mesh reduces to a 2D perspective image.

4.2 Transforms

Once a set of discrete sample points for the lumigraph has been chosen, we can select a pair of transforms to apply to the sampled data, one for the (θ, ϕ) dimensions, and another for (s, t). As we have already stated, these transforms form the heart of the compression algorithm. In addition, the (θ, ϕ) transform

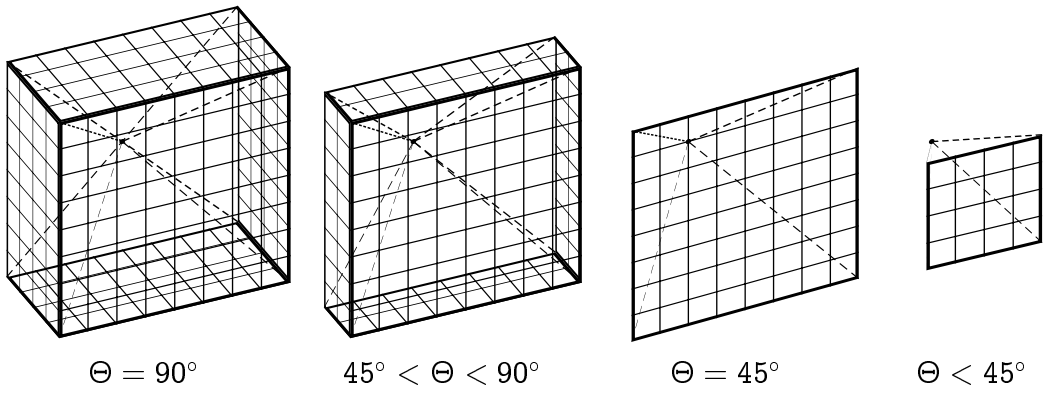

Figure 4.3: Representation of the directional dimensions with a hemicube. As the maximum viewing angle decreases, the sides faces shrink and then disappear altogether.

implicitly defines the basis functions $\xi_m(\theta, \phi)$, and the data resulting from its application forms the hogel vector used by Equation (3.24). Ideally, the chosen transform should reduce the data to a relatively small number of non-zero (or at least non-negligible) components. This will both allow a high compression ratio and reduce the computation time required to convert the lumigraph to a hologram using weighted sums. Because the lumigraph is essentially a four-dimensional image, we will concentrate on several transforms which have previously been used for image compression.

4.2.1 Windowed discrete cosine transform

The discrete cosine transform (DCT), a relative of the Fourier transform, operates on a one-dimensional, n–point array f_j to produce the coefficients $c_i = \sum_{j=0}^{n-1} f_j \cos(\frac{i(2j+1)\pi}{2n})$. It can be applied to higher-dimensional data sets by performing one-dimensional DCTs on each dimension in succession. A windowed DCT breaks the array up into smaller blocks and performs a DCT on each one independently. The result is a localized frequency analysis of f. Figure 4.4 shows

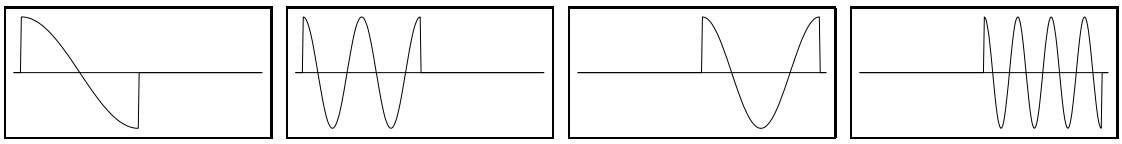

Figure 4.4: Several of the basis functions generated by the windowed DCT

a few of the basis functions derived from the use of this transform.

This operation lies at the heart of the highly successful JPEG [97, 117] image compression standard, which uses 8-by-8 point DCTs. For any given region of a typical image, most of the higher frequency (detail) coefficients are likely to be insignificant, and those which are significant require only a coarse representation to provide a perceptually accurate reconstruction. This allows the transformed image to be represented with significantly fewer bits than the untransformed image.

4.2.2 Wavelets

A more sophisticated frequency analysis can be obtained through the use of wavelet transforms. A comprehensive discussion [28, 29, 36] of wavelet theory is beyond the scope of this thesis. We will only provide a general overview here.

A wavelet transform uses a pair of one-dimensional analysis filters, $\tilde{h}$ and $\tilde{g}$, and a complementary pair of synthesis filters, h and g. Let the original data array be given by $\lambda_{j_0,k}$, where j_0 is some arbitrary fixed value. Then one step of the wavelet transform generates two arrays half the size of the original:

$$\lambda_{j-1,l} = \sum_k \tilde{h}_{k-2l} \lambda_{j,k} \tag{4.4}$$

$$\gamma_{j-1,l} = \sum_k \tilde{g}_{k-2l} \lambda_{j,k} \tag{4.5}$$

$\lambda_{j-1,l}$ represents a set of average terms, while $\gamma_{j-1,l}$ provides detail terms. By

repeatedly applying the above equations, we obtain a small array λ_0 and several arrays γ_j, for $0 \leq j \leq j_0$. A step of the inverse transform is given by

$$\lambda_{j,k} = \sum_l h_{k-2l}\lambda_{j-1,l} + \sum_l g_{k-2l}\gamma_{j-1,l} \tag{4.6}$$

Similarly, through repeated application of this equation, we can obtain the original data.

The filters h and g implicitly define two functions, φ and ψ. φ, the *scaling function*, is given by $\varphi(x) = \sum_k h_k \varphi(2x - k)$, while ψ, the *wavelet function*, is given by $\psi(x) = \sum_k g_k \varphi(2x - k)$. The dilations and translations of these functions, $\varphi_{j,k}(x) = \varphi(2^j x - k)$ and $\psi_{j,k}(x) = \psi(2^j x - k)$, are the basis functions corresponding to the transformed coefficients $\lambda_{j,k}$ and $\gamma_{j,k}$, respectively. As j increases, the functions represent higher frequency details over smaller regions. This is in contrast to the discrete cosine transform, which does not change scale as the frequency changes.

For a well chosen set of filters, only a small percentage of the detail terms will be significant, allowing the data to be compressed. We experimented with several common wavelets, illustrated in Figures 4.5 through 4.9.

4.2.3 Applying transforms in higher dimensions

2D

As mentioned above, the discrete cosine transform can be applied to a two-dimensional image by transforming in each dimension independently. That is, the one-dimensional DCT is applied to each of the rows of the image, and then subsequently to each of the columns. Wavelet transforms can be applied to a 2D array in the same way, but the results will not be optimal. Most wavelet-based

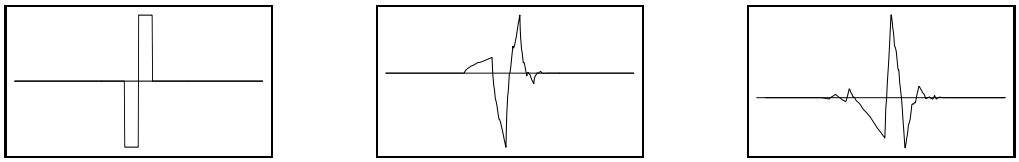

D2 (Haar) D4 D6

Figure 4.5: Daubechies orthonormal wavelets [35]

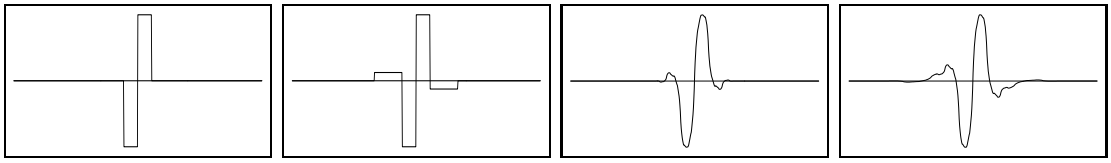

(1,1) (1,3) (3,1) (3,3)

Figure 4.6: Average-interpolating wavelets [38, 102]

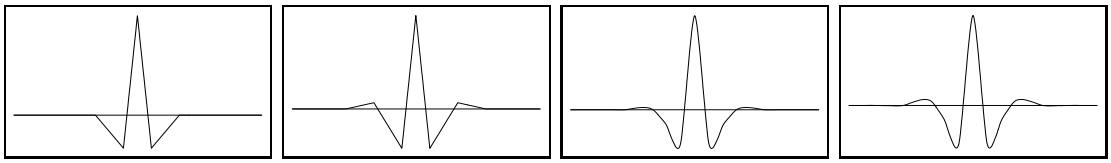

(2,2) (2,4) (4,2) (4,4)

Figure 4.7: Interpolating wavelets [37, 102]

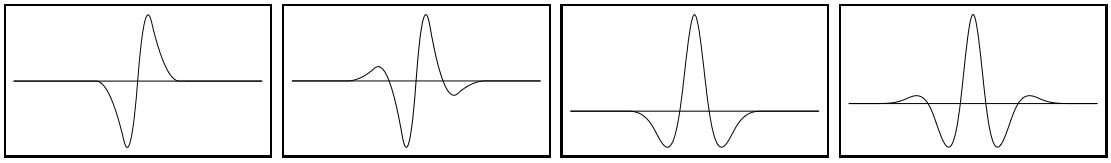

(3,1) (3,3) (4,2) (4,4)

Figure 4.8: Cohen-Daubechies-Feauveau biorthogonal wavelets [32]

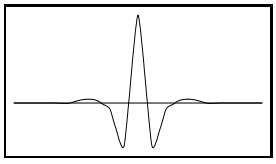

Figure 4.9: (9,7) spline variant wavelet [2]

compression algorithms interleave the two transforms to obtain better compression. We iterate over all j a single time, at each step applying Equations (4.4) and (4.5) first in one dimension, then the other. In general, the resulting wavelet functions provide a better fit to the data than those generated by iterating over each dimension separately.

Hemicube

For the directional dimensions, we must apply a transform to the hemicube. Since the hemicube is composed of five rectangular faces, we can simply apply a two-dimensional transform to each face (Figure 4.10). However, in this case, compression and subsequent decompression can introduce discontinuities at the boundaries between the faces. We therefore take some additional steps.

We begin by unfolding the hemicube and embedding it in a single 2D array (Figure 4.11(a)), which is then transformed and compressed. After decompression, the corner regions are discarded and the hemicube refolded. This eliminates the discontinuities between the front face and the four side faces. However, it can actually worsen discontinuities between adjacent side faces. Furthermore, it increases the size of the array by one third.

To solve the first problem, we copy a thin strip (8 to 16 pixels wide) from the edges of the side faces to the opposing edges of the corner regions (Figure 4.11(b)). This provides the desired continuity during compression. Afterwards, the added data is discarded along with the rest of the corner region.

The second problem is handled by setting the value in the remaining portion of each corner region to a constant equal to the average over the corresponding quadrant of the array (Figure 4.11(c)). This ensures that, after the transform is

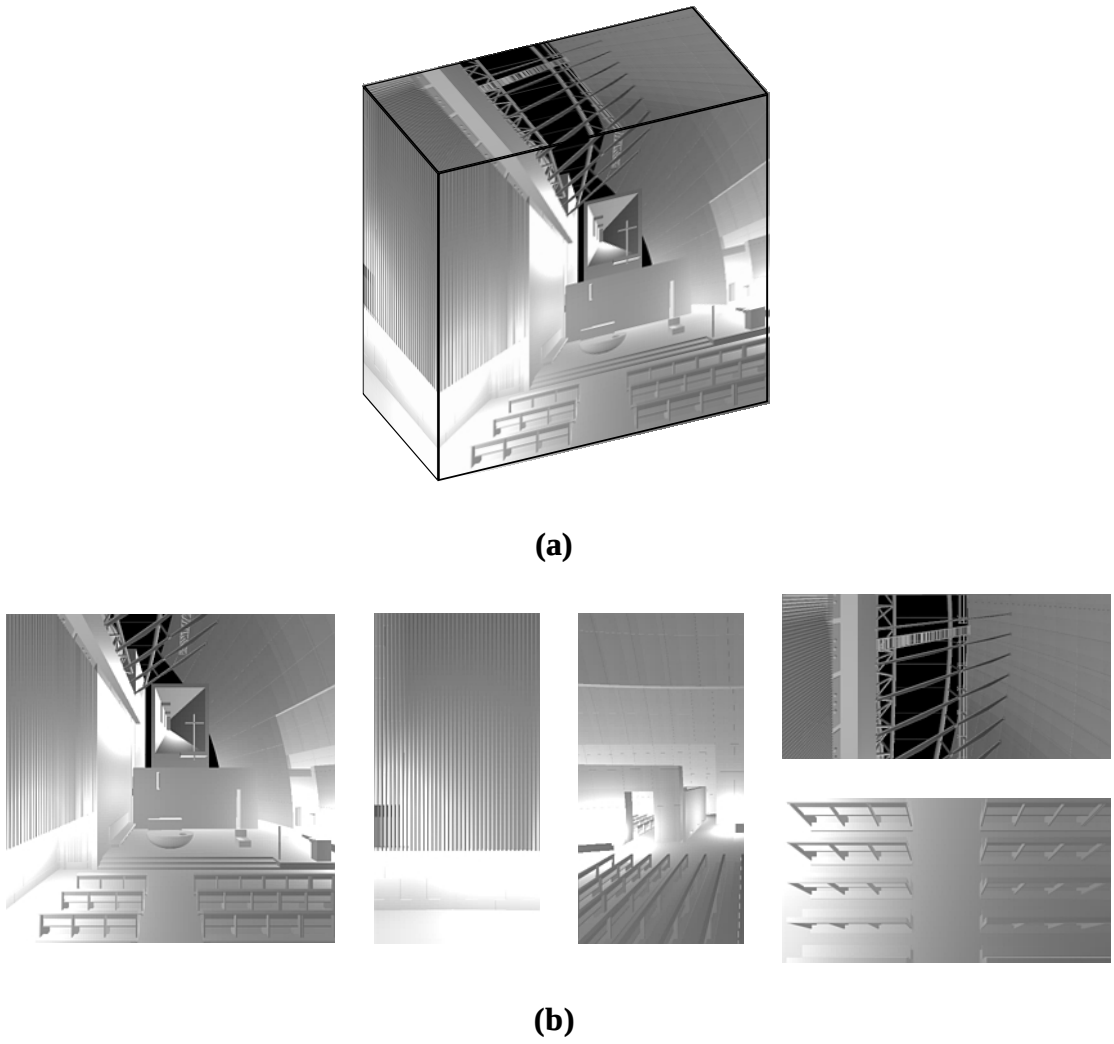

(a)

(b)

Figure 4.10: One way to apply a transform to the hemicube is to separate it into its individual faces and apply the transform to each.

applied, relatively few additional terms will be needed to represent these regions, despite the increase in the size of the raw data. The only remaining difficulty lies at the boundary of this constant region, where the sharp edge can require a relatively large number of terms. To alleviate this, we apply a cubic interpolation function to the strips added at the edges to smoothly blend them between the original data and the constant region (Figure 4.11(d)).

This procedure does not guarantee continuity of the function over the hemi-

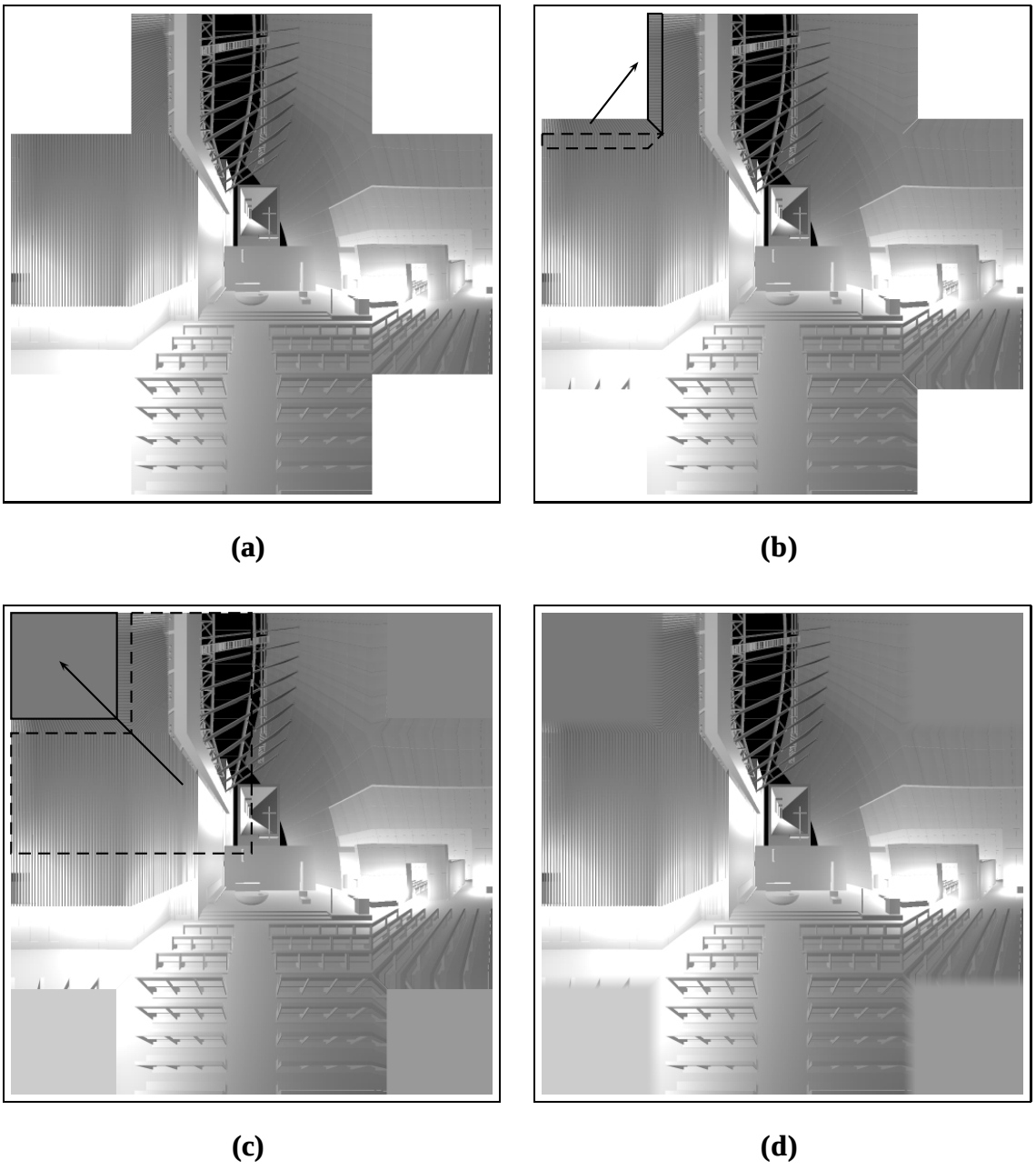

Figure 4.11: The hemicube is unfolded into a single array and the corner regions are filled in so as to eliminate discontinuities caused by compression.

cube in any rigorous mathematical sense. However, we have found that, in practice, it produces a visually smooth representation of the data even at high compression ratios, while not significantly increasing the compressed data size. Of course, in the common case where the viewing frustum is less than 45 degrees, only the front face is needed, and we can dispense with these extra measures.

4D

When applying a transform in four dimensions, as with two, better compression can generally be gained by interleaving all four transforms. However, recall from Figure 4.1(b) that when the interference pattern is computed via weighted sums, we only need to perform the inverse transform in the spatial dimensions. In this case we cannot interleave transformation in the spatial dimensions with that in the directional ones, and must treat them independently.

4.3 Entropy Coding

Before examining what to do with the data once it has been transformed, let us skip to the end of the compression process and discuss entropy coding. Suppose we have a message consisting of a string of symbols from some alphabet. If we wish to store the message electronically, we can assign a binary number to each symbol and use these to convert the message into a string of bits. This requires $\lceil \log_2(A) \rceil$ bits per symbol, where A is the size of the alphabet. Entropy coding is a generic term for a class of algorithms that assign fewer bits to more common symbols and more bits to rarer symbols, so as to reduce the total size of the

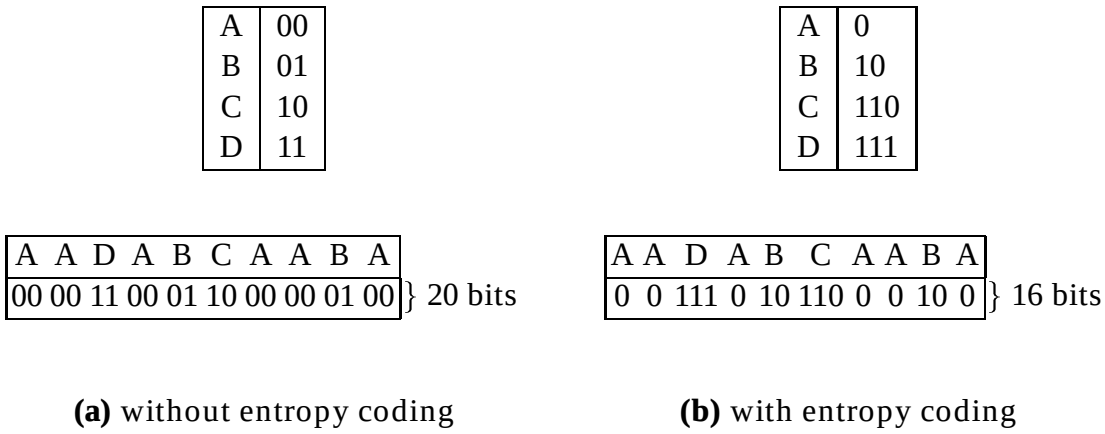

(a) without entropy coding **(b)** with entropy coding

Figure 4.12: Encoding a message as a binary string with and without entropy coding

message.

This is best explained by example. Consider an alphabet consisting of the letters A, B, C, and D. We can assign a two-bit number to each of these (Figure 4.12(a)). A message consisting of 10 symbols will therefore require 20 bits. However, suppose we know that the letter A composes 60% of the message, B accounts for 20%, and C and D only 10% each. We can instead assign 1 bit to A, 2 bits to B, and 3 to C and D (Figure 4.12(b)). Now the total number of bits required is 16, a 20% savings. More sophisticated schemes assign non-integral numbers of bits to each symbol, allowing even more compression. In our implementation, we will use one such algorithm, known as arithmetic encoding [127].

In the following section, we discuss several algorithms which encode the structure of the transformed data in a compact form using one or more sets of symbols. Some of these sets are quite large, but will be designed so that a few symbols are common while most occur only infrequently. This will allow us to efficiently compress them using entropy coding.

16	11	10	16	24	40	51	61
12	12	14	19	26	58	60	55
14	13	16	24	40	57	69	56
14	17	22	29	51	87	80	62
18	22	37	56	68	109	103	77
24	35	55	64	81	104	113	92
49	64	78	87	103	121	120	101
72	92	95	98	112	100	103	99

Figure 4.13: Example quantization table for use in JPEG compression

4.4 Quantization and Symbol Generation

As we have stated, the purpose of the transform is to separate the data into a few significant components and a large number of insignificant ones. To take advantage of this for the sake of compression, we need to encode the fact that these entries are insignificant using a relatively small number of bits. We utilize two different methods. For the discrete cosine transform, we use a 4D extension of the JPEG compression scheme, while for the wavelet transforms, we use an algorithm based on Shapiro's zerotree encoding.

4.4.1 JPEG-based encoding

As we have discussed, JPEG [97, 117] transforms an image by dividing it into 8-by-8 blocks and performing a two-dimensional DCT on each one. To encode this transformed data, each element of each block is divided by the corresponding element of an integer quantization table, such as the one in Figure 4.13. This helps compress the data by zeroing out many of the frequency components and reducing the number of bits required to represent the remaining terms.

This process is lossy, and care must be taken in choosing the quantization

coefficients. Larger entries provide more compression, but introduce larger errors. The JPEG standard does not require any specific matrix be used, but it does provide the above matrix as an example. This table was derived by performing a set of perceptual experiments on how much each frequency component can be changed before producing a just noticeable difference in the image. In general, errors in high frequency components are less noticeable than those at lower frequencies, allowing the quantization values to be correspondingly larger.

This quantization can be trivially extended to the lumigraph with a four-dimensional matrix. We chose to use the matrix formed by taking the outer product of two copies of the matrix in Figure 4.13. To increase or decrease the compression ratio (at the cost of introducing greater error) we multiply the entire array by a scalar factor.

After quantization, JPEG traverses the data block in the zigzag fashion seen in Figure 4.14, performing run-length encoding of the zero entries. For each non-zero element we output a tuple, (z, b), containing the number of consecutive zero entries preceding it and the number of bits required to represent it. This is followed by the number of bits containing the value of the entry. By examining the data, we can obtain a maximum possible value, $b_{\max}$, for the number of bits, while a maximum, $z_{\max}$, for the number of zeroes can be arbitrarily chosen. If the actual number of consecutive zeroes exceeds this maximum, then one or more pairs of the form $(z_{\max}, 0)$ can be generated prior to the tuple representing a non-zero entry.

These tuples combine to form a finite alphabet with $(z_{\max} + 1)(b_{\max} + 1)$ members. Due to the quantization, we expect the tuples with large z and small b will be far more common than the others. As we have discussed, this will

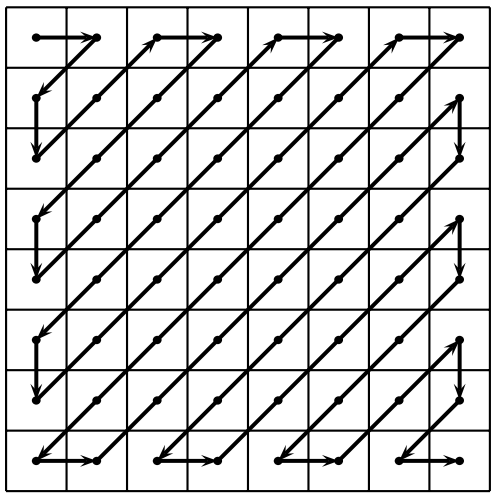

Figure 4.14: JPEG traverses each 8-by-8 block in a zigzag fashion

allow the data to be represented very compactly once entropy coding has been applied.

4.4.2 Wavelet encoding

For the wavelet transforms, we use a more sophisticated scheme which takes advantage of an important feature of these transforms. As we have stated, each successive application of Equation (4.5) produces half as many detail terms as the previous iteration. These terms can be organized into a binary tree (Figure 4.15), with $\gamma_{j,k}$ as the parent of $\gamma_{j+1,2k}$ and $\gamma_{j+1,2k+1}$. In two dimensions, this becomes a set of quadtrees, and so on for higher dimensions.

In general, the magnitude of any given node in the tree will tend to be less than that of its parent. This means that if one node is insignificant, the entire subtree below it can often be dismissed as insignificant. The embedded zerotree wavelet (EZW) compression algorithm of Shapiro [105] is based on this fact. Our own method is designed to yield comparable compression ratios but operate at

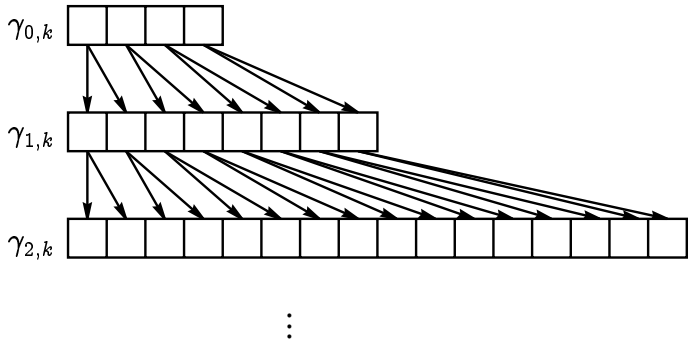

Figure 4.15: Wavelet coefficient hierarchy

a faster rate. We will first summarize Shapiro's algorithm, and then describe our own variation.

EZW

Let $T_{\max}$ be the magnitude of the largest entry in the transformed data. The EZW algorithm begins by setting an initial threshold $T = \frac{1}{2}T_{\max}$. The tree is traversed in a breadth-first manner, and each node is categorized using one of four symbols which is sent to the output. Figure 4.16(a) illustrates this for a sample tree. If the magnitude of the node is greater than T and its sign is positive, it is labeled as positive significant (POS). Similarly, if its magnitude is greater than T and its sign is negative, it is labeled negative significant (NEG). If the magnitude is less than or equal to T, but some entry in the node's subtree is significant, it is labeled as an isolated zero (IZ). Finally, if the magnitude of the node and every node below it is less than or equal to T, it is labeled as a zero tree (ZT). In this last case, we can skip the rest of the nodes in the subtree.

Once the entire tree is categorized, T is reduced by half, and we traverse the tree again. This time, we ignore any node which was previously labeled as

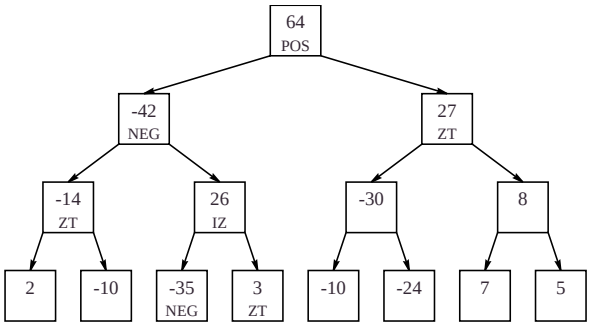

Output:	POS	NEG	ZT	ZT	IZ	NEG	ZT

(a) $T = 32$

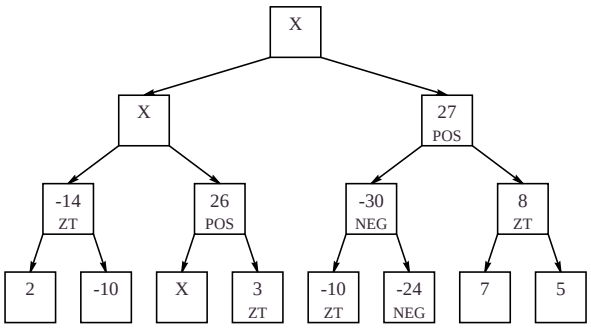

Output:	POS	ZT	POS	NEG	ZT	ZT	ZT	NEG

(b) $T = 16$

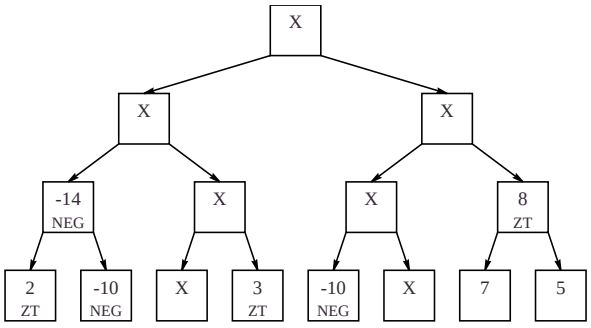

Output:	NEG	ZT	ZT	NEG	ZT	NEG

(c) $T = 8$

Figure 4.16: Several iterations of the main pass of the EZW algorithm

significant (Figures 4.16(b) and 4.16(c)). We can repeat this process indefinitely until every node has been detected as significant.

If we read in these symbols, we obtain an estimate for the value of every element of the data set. Given the current threshold T at the time a node is detected as significant, then the reader knows that its value lies in the interval $(T, 2T]$ (or $[-2T, T)$ for negative significant nodes). To get a better estimate, we add a refinement pass between each traversal of the tree. At any given time, based on the symbols previously generated, we can determine the value of every data point to within an interval of size T. During the refinement pass, we output, for each node which has previously been detected as significant, a single bit indicating whether it lies in the upper or lower half of the current bounding interval.

In this way, we obtain a progressively more and more accurate representation of the data. We continue this until a desired threshold, a maximum output size, or some more sophisticated stopping condition is met. At this point, a special END symbol is generated and the compression halts. This allows a very high degree of control over the tradeoff between compression ratio and error.

Three-pass method

The iterative refinement provided by the EZW algorithm requires that the entire data array be processed many times. For a two-dimensional image, the time required is not significant, but in 4D, the cost can be quite prohibitive. We therefore desire a new algorithm which provides comparable compression, but with only a few passes through the data. To achieve this, we will sacrifice our ability to specify the compression ratio exactly.

As with EZW, we begin by determining the maximum magnitude, $T_{\max}$, in

the transformed data. Next, we traverse the tree from leaves to root, calculating two numbers, which we call p_t and p_n, for each node (Figure 4.17(a)). For a node with a value of x, p_n is calculated as $p_n = \left\lfloor \log_2 \left(\frac{T_{\max}}{|x|} \right) \right\rfloor$. It is equal to the number of passes that would be required by the EZW algorithm before the node was detected as significant. p_t is set to the minimum value of p_n over all members of the node's subtree, inclusive. It is equal to the number of EZW passes before the node is categorized as either significant or an isolated zero.

We traverse the tree again, this time from root to leaves, assigning two new numbers, Δp_t and Δp_n, to the nodes (Figure 4.17(b)). Δp_t is the difference between the p_t values of the node's parent and of the node itself. For the purposes of this computation, the p_t value of the root node's parent is assumed to be zero. Δp_n is the difference between the node's p_t value and its p_n value. Δp_t and Δp_n encode the same information as p_t and p_n, but in a relative, rather than absolute form.

Now let us assume that we have some number of bits, $b_{\max}$, defining the accuracy, $T_{\min} = \left(\frac{1}{2}\right)^{b_{\max}} T_{\max}$, at which the data will be output. We will discuss how $b_{\max}$ is determined shortly. Given $b_{\max}$, we can define two finite alphabets, whose symbols consist of the numbers from -1 to $b_{\max} - 1$, to represent Δp_t and Δp_n.

We traverse the tree one more time, generating a set of symbols for each node (Figure 4.17(c)). If $p_n < b_{\max}$, the node is significant, and we output the values of Δp_t and Δp_n, a single bit indicating the sign of the node's value, and $b_{\max} - p_n - 1$ bits containing the node's value quantized by $T_{\min}$. (Only $b_{\max} - p_n - 1$ rather than $b_{\max} - p_n$ bits are required because the highest order bit is always 1.) For a significant leaf node, the symbol for Δp_n can be omitted, because $p_n = p_t$. If

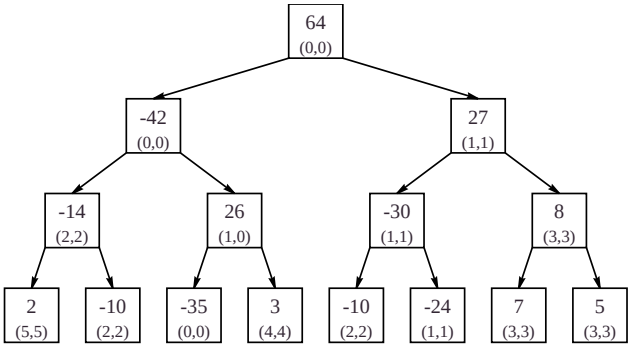

(a) (p_t, p_n) for each node

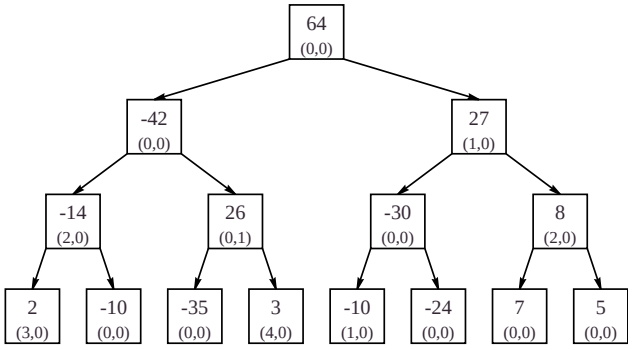

(b) $(\Delta p_t, \Delta p_n)$ for each node

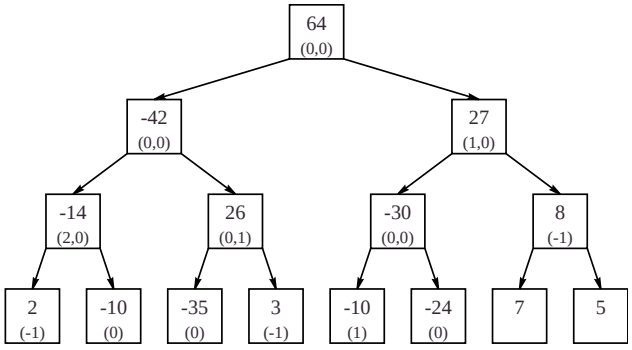

(c) The symbols output for each node given $b_{\max} = 3$

Figure 4.17: Wavelet tree compression using three-pass method

$p_t < b_{\max} \leq p_n$, the node is an isolated zero, and we output the value of Δp_t and a special -1 symbol for Δp_n. Finally, if $b_{\max} \leq p_t$, the node is a zero tree root. In this case, we output a -1 for Δp_t, and we skip processing any nodes in its subtree.

Recall that the values of the nodes of a subtree tend to be less than the value of the root. This means that Δp_n will tend to be zero. Because Δp_t gives the node's p_t value relative to that of its parent, it too will tend to be small. This means that, when entropy coding is applied to the symbols, significant compression will be gained.

We now consider how to select $b_{\max}$. We construct a histogram $h(p_n)$ of the frequency with which each value p_n appears in the data. For any given $b_{\max}$, a significant node with a given p_n will require $b_{\max} - p_n$ bits, plus some overhead to represent the structure of the tree. If we assume that this overhead is a constant, c, for all significant nodes, then the entire tree requires $\sum_{p_n=0}^{b_{\max}-1} h(p_n)(b_{\max} - p + c)$ bits to represent. For a desired compression ratio, we substitute different values of $b_{\max}$ into the above equation to find which one yields a compression size that most closely matches our needs. Only an approximate value is required for c, and this can be found by experimentation with typical data sets.

In our application, this algorithm yields error vs. compression ratio statistics roughly equivalent to those of EZW (Figure 4.18), but requires only three passes through the data set. The first pass determines the value of $T_{\max}$. The second computes p_n and p_t, and accumulates the histogram $h(p_n)$, after which $b_{\max}$ can be chosen. Finally, the third pass computes Δp_t and Δp_n, and generates the output. This speed comes at the cost of the precise control over compression ratio provided by EZW. Our algorithm only allows the compression to be specified

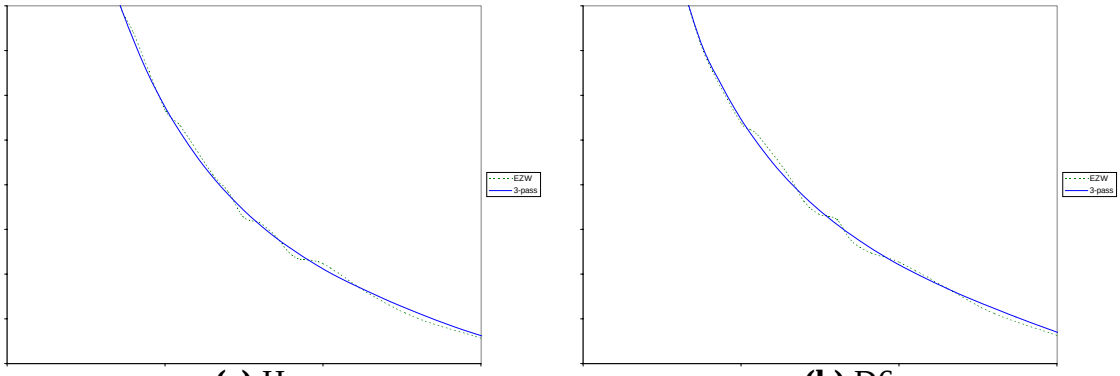

(a) Haar **(b)** D6

Figure 4.18: We plot image quality versus compression ratio (using the metrics described in the following section) for both Shapiro's EZW encoding scheme and our 3-pass version for two different wavelet transforms. As the graphs show, the two methods produce roughly equivalent results.

approximately.

4.5 Results

4.5.1 Error metric

To evaluate our compression algorithm, we need to select an error metric. The most commonly used metrics for evaluating image compression algorithms are peak signal to noise ratio (PSNR) and signal to quantization noise ratio (SQNR). Let f_i be the original data set, and f_i' be the result of applying compression and decompression to f_i. Then these two error metrics are given by

$$\text{PSNR} = 10 \log_{10} \left(\frac{N(\max_i(f_i))^2}{\sum_{i=0}^{N-1}(f_i - f_i')^2} \right) \tag{4.7}$$

$$\text{SQNR} = 10 \log_{10} \left(\frac{\sum_{i=0}^{N-1} f_i^2}{\sum_{i=0}^{N-1}(f_i - f_i')^2} \right) \tag{4.8}$$

These metrics are almost equivalent, differing only in the decision as to

whether to use the peak or average value of the data set to normalize the results. When comparing different compression methods on the same image, this choice is irrelevant. It only becomes significant when comparing the error across different images. In this case, SQNR is generally the better option, and is what we will use for our error metric.

The value of the SQNR has no precise physical meaning. Rather, it serves as a relative measure by which different compression schemes can be compared. Most algorithms typically operate in a range between 40 (roughly a 1% error in each pixel) and 20 (roughly a 10% error).

The SQNR simply measures the total error without regard to the resulting data's appearance. Because the human visual system is more sensitive to certain types of errors, several more sophisticated, perceptually-based error metrics have been proposed. However, the problem of extending a perceptual metric for a two-dimensional image to a four-dimensional lumigraph is not trivial. Recall that the lumigraph consists of numerous 2D images, and that the image seen by someone viewing it is composed of samples drawn from many of them. It is unclear how perceptually large or small errors in these individual images may affect the overall view. They may interfere positively to produce large errors, or negatively to be barely noticeable, and this interaction may vary depending on the viewer's position. For this reason, we prefer to rely on the non-subjective metric provided by the SQNR.

4.5.2 Compression metric

We choose to compute and represent the lumigraph in floating point form, rather than fixed point, in order to take full advantage of the capabilities of a

holographic display system. An ordinary two-dimensional monitor or printer has a rather narrow dynamic range, allowing images for it to be represented using only eight bits per color channel. A holographic display is much less limited. Recall that when we view a point on a hologram, we are actually looking at a finite region which, although very small, is still composed of many holographic pixels. The light that reaches our eyes is the result of interference between all of these pixels. Even if the individual pixels possess only a single bit of resolution, their combination can have, in theory, a dynamic range of well over a million to one. Of course, in practice, a real holographic display would be hard-pressed to achieve this limit. However, we can still expect a potential dynamic range significantly larger than that of an ordinary monitor, and we therefore choose not to limit our computed lumigraph to a fixed precision.

This makes the term "compression ratio" somewhat meaningless, since there is no well-determined size requirement for the original data with which to compare the compressed data. We can, at best, bound the original data by saying that it lies between eight bits (a typical grey-scale image) and 32 bits (standard floating point representation) per pixel. Nevertheless, we can still define a metric proportional to compression ratio by using the number of pixels per bit in the compressed data.

4.5.3 Results

Due to memory constraints, we were unable to apply compression to a full-size four-dimensional lumigraph. Instead, we used three-dimensional lumigraphs with 512 samples in U and V, and 128 or 256 samples in s. We tested each of the transforms on lumigraphs of two models. The first was a simple jack-o-lantern

which produces relatively low frequency images; the second was a complex church model which yields images with more high-frequency details. Errors were measured over a large range of compression values, from a fraction of a pixel per bit (no compression) to over 100 ppb ($\gtrsim$ 1000:1 compression).

The resulting errors are charted in Figures (4.19) and (4.20). For a visual comparison, Figures (4.21) through (4.28) show the results of compressing the lumigraphs with each of the transforms to about 8 ppb. These figures show a single two-dimensional slice of each of the lumigraphs. Recall that in order to achieve fast compression, we sacrificed our ability to precisely specify the output size, so it is not possible to apply the different transforms to exactly the same degree of compression. Nevertheless, they are close enough to allow a rough comparison. The compression chosen yields a SQNR of roughly 30 for the better transforms. At this point, errors are becoming noticeable, but the image quality remains quite high.

As the graphs and images show, the interpolating and average interpolating wavelets tended to perform better than the other compressors. The highest overall performance was from the (3,3) average interpolating wavelet, and this is what we chose to adopt for our needs. In Figure 4.29, we see the affect of varying the compression rate on the lumigraph quality with this transform.

One issue of which we must take special note is the relatively low performance of the JPEG-based compression. It is likely that this is due at least in part to a poor choice of quantization matrix. A great deal of research is being done on algorithms for finding the optimal JPEG quantizer for a given image. If such an optimizer could be adapted to operate on lumigraphs, we expect that significantly better performance could be achieved. Nevertheless, we do not believe

that it would perform as well as the best of the wavelet transforms.

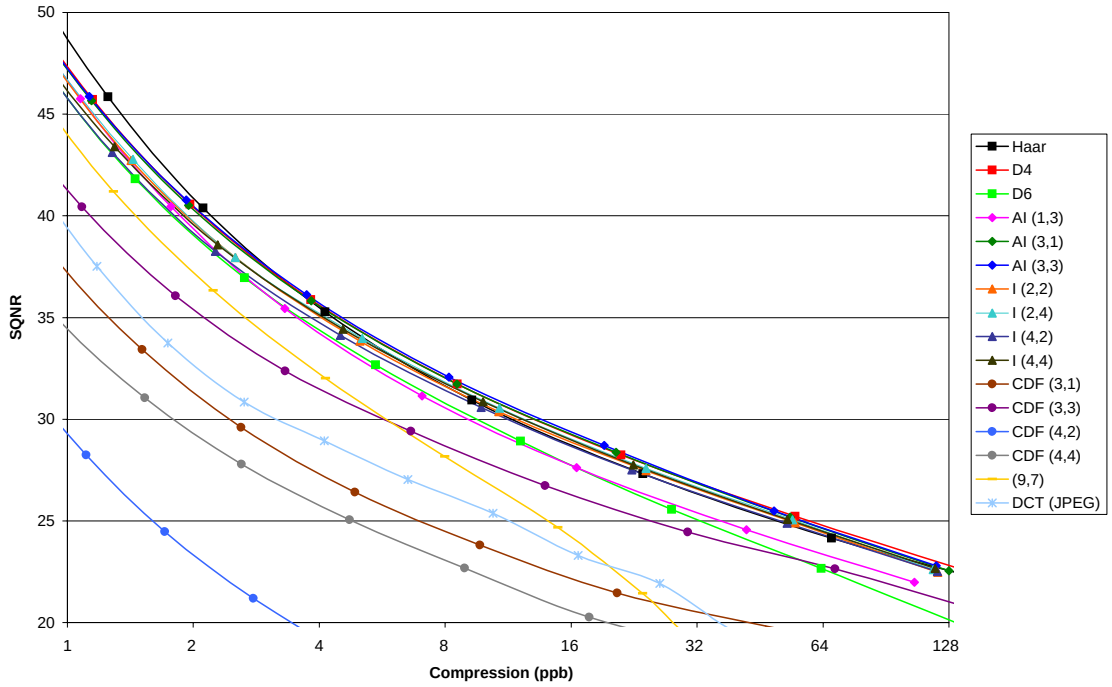

Figure 4.19: Compression statistics for jack-o-lantern

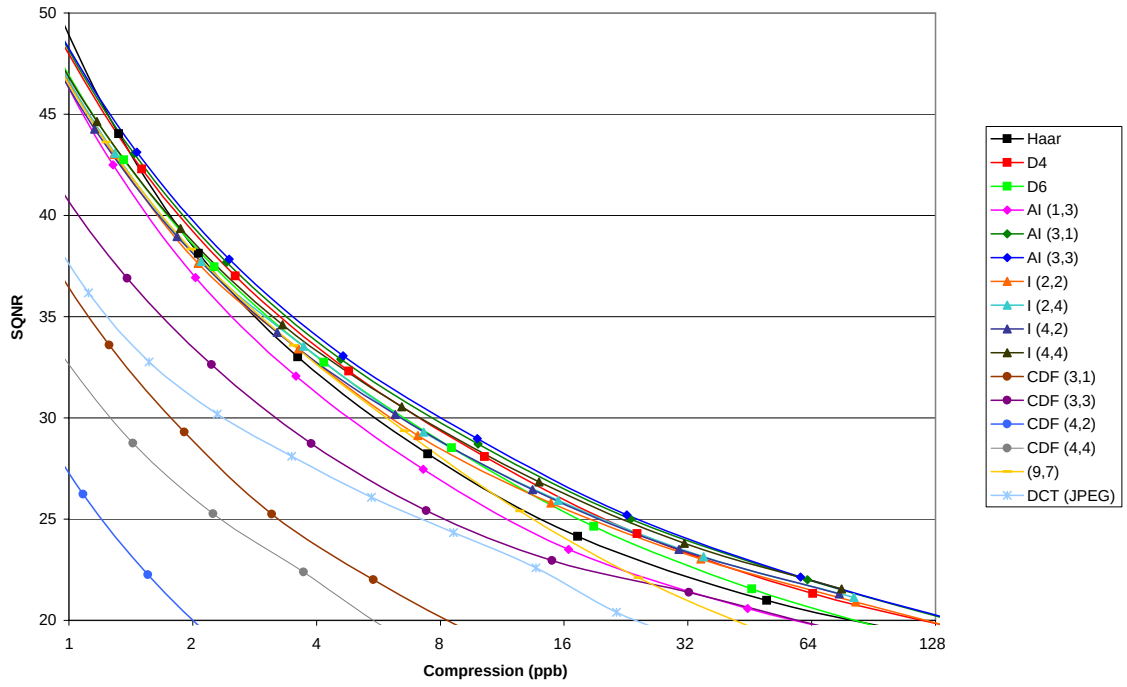

Figure 4.20: Compression statistics for church

Haar
5.2 ppb

(1,3) average interpolating
8.9 ppb

(3,1) average interpolating
5.5 ppb

(3,3) average interpolating
5.8 ppb

Figure 4.21: Comparison of transforms for compression of jack-o-lantern (model by Dave Edwards)

(2,2) interpolating
7.5 ppb

(2,4) interpolating
8.3 ppb

(4,2) interpolating
7.0 ppb

(4,4) interpolating
7.6 ppb

Figure 4.22: Comparison of transforms for compression of jack-o-lantern (cont.)

CDF (3,1)
11.6 ppb

CDF (3,3)
8.0 ppb

CDF (4,2)
7.0 ppb

CDF (4,4)
6.7 ppb

Figure 4.23: Comparison of transforms for compression of jack-o-lantern (cont.)

Daubechies 4
5.4 ppb

Daubechies 6
6.4 ppb

(9,7)
7.2 ppb

JPEG
7.4 ppb

Figure 4.24: Comparison of transforms for compression of jack-o-lantern (cont.)

Haar
9.2 ppb

(1,3) average interpolating
10.3 ppb

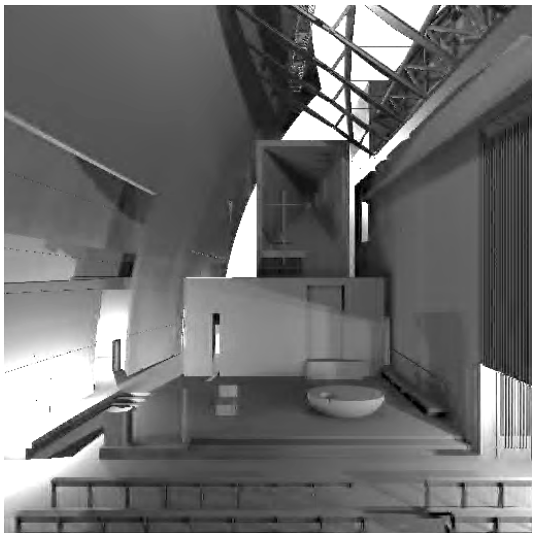

(3,1) average interpolating
5.1 ppb

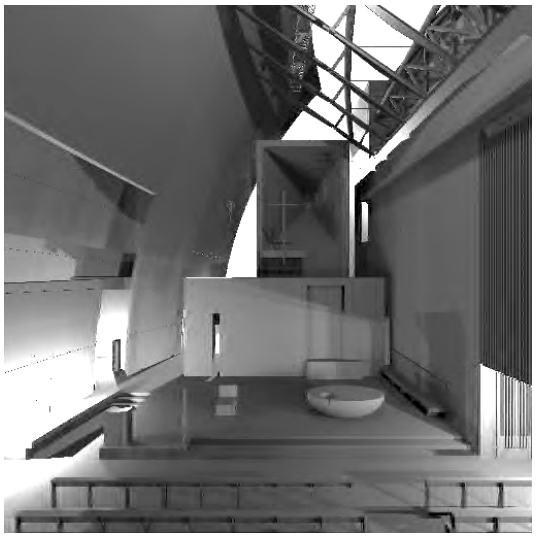

(3,3) average interpolating
5.5 ppb

Figure 4.25: Comparison of transforms for compression of church scene (model by Richard Meier Associates)

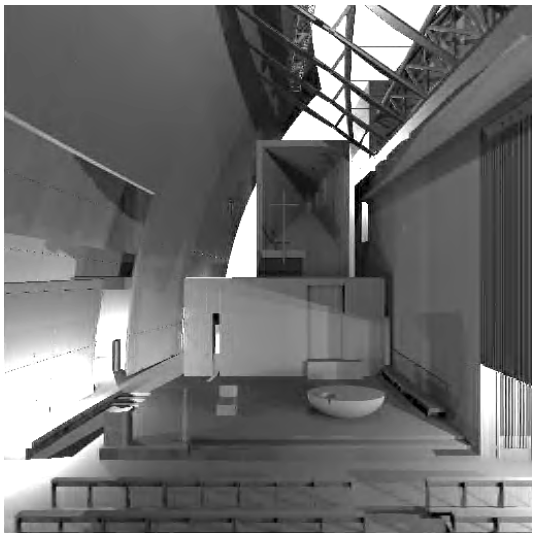

(2,2) interpolating
6.7 ppb

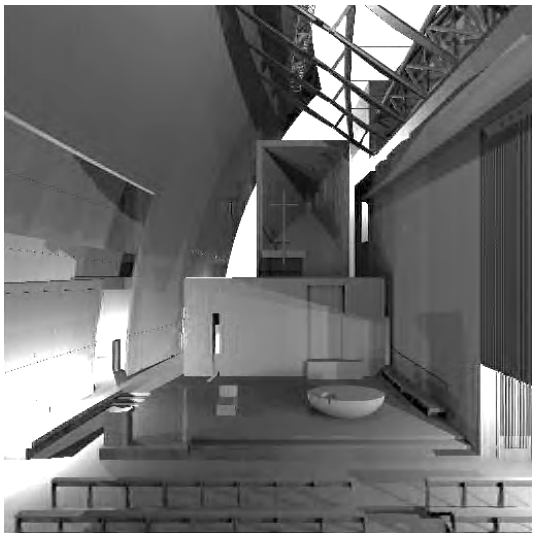

(2,4) interpolating
7.4 ppb

(4,2) interpolating
6.3 ppb

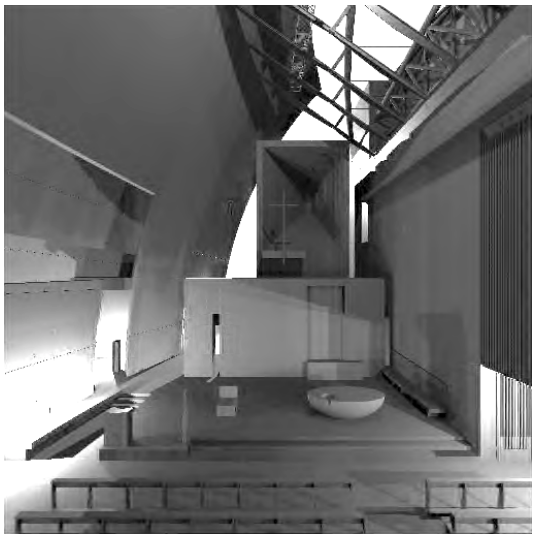

(4,4) interpolating
6.8 ppb

Figure 4.26: Comparison of transforms for compression of church scene (cont.)

CDF (3,1)
10.6 ppb

CDF (3,3)
7.7 ppb

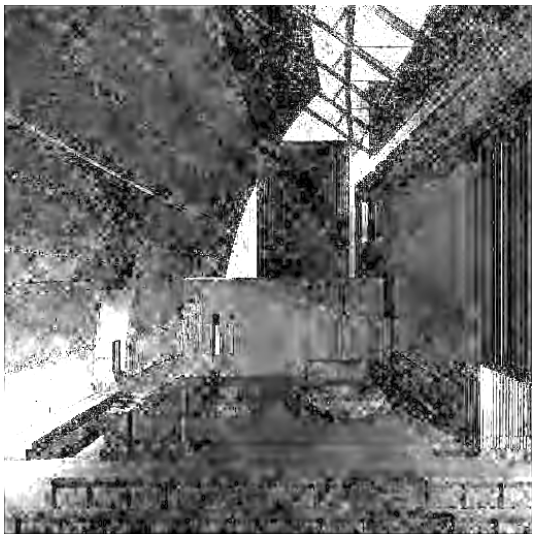

CDF (4,2)
6.1 ppb

CDF (4,4)
9.6 ppb

Figure 4.27: Comparison of transforms for compression of church scene (cont.)

Daubechies 4
11.8 ppb

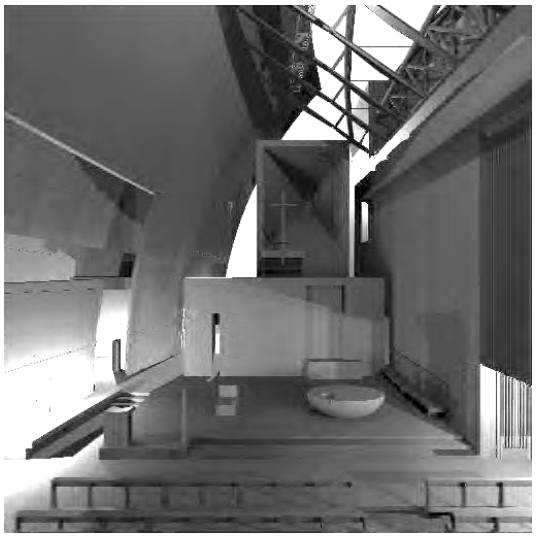

Daubechies 6
7.5 ppb

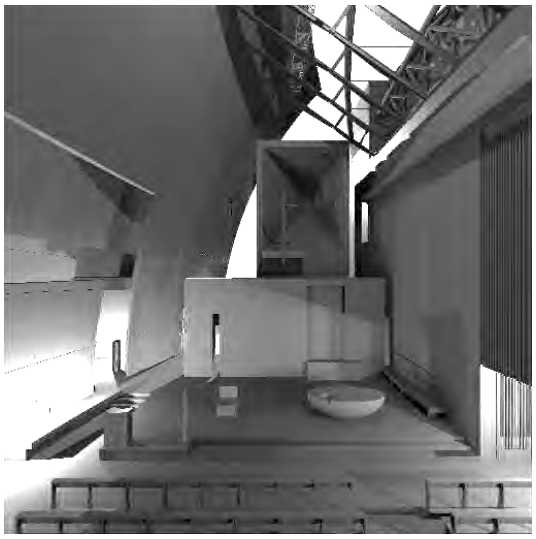

(9,7)
7.1 ppb

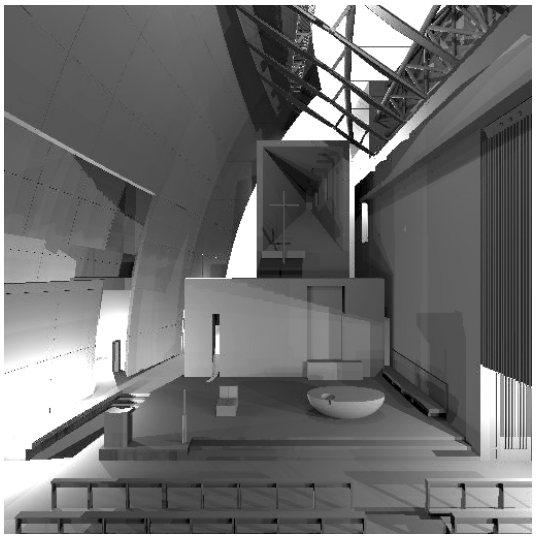

JPEG
8.5 ppb

Figure 4.28: Comparison of transforms for compression of church scene (cont.)

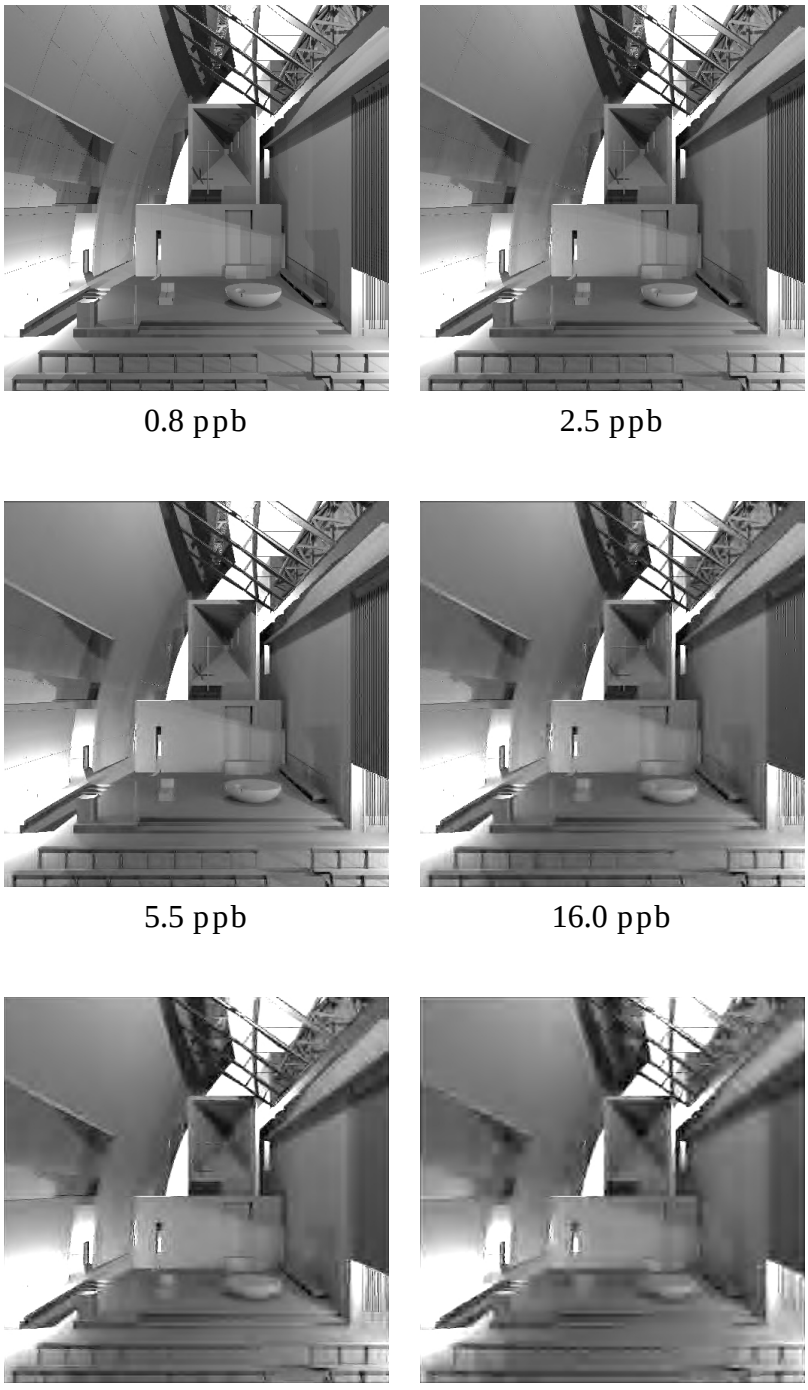

Figure 4.29: Comparison of lumigraph quality at several degrees of compression using (3,3) average interpolating wavelets applied to the church scene

Chapter 5

Rendering

Having determined how we will represent and compress the lumigraph, we now turn to the problem of computing it. Most previous methods for generating a lumigraph from a scene description have utilized multiple applications of standard two-dimensional rendering algorithms. However, in order to make full use of a holographic display, we must be able to compute a lumigraph at near real-time rates. This requires rendering speeds orders of magnitude greater than current methods allow. We can expect that a portion of this deficit will be eliminated by general improvements in processing power achieved by the time an electronic holographic display becomes a commercial reality. Nevertheless, a significant gap will remain, which can only be overcome by developing new algorithms specifically designed for the four-dimensional case.

The key to reducing rendering time is to take maximum advantage of coherence in the lumigraph to speed or eliminate related and redundant computations. Previous methods have made use of coherence in only a few dimensions of the lumigraph. In this chapter, we will develop an algorithm which uses all four dimensions. Our method parallels, wherever possible, the operations of

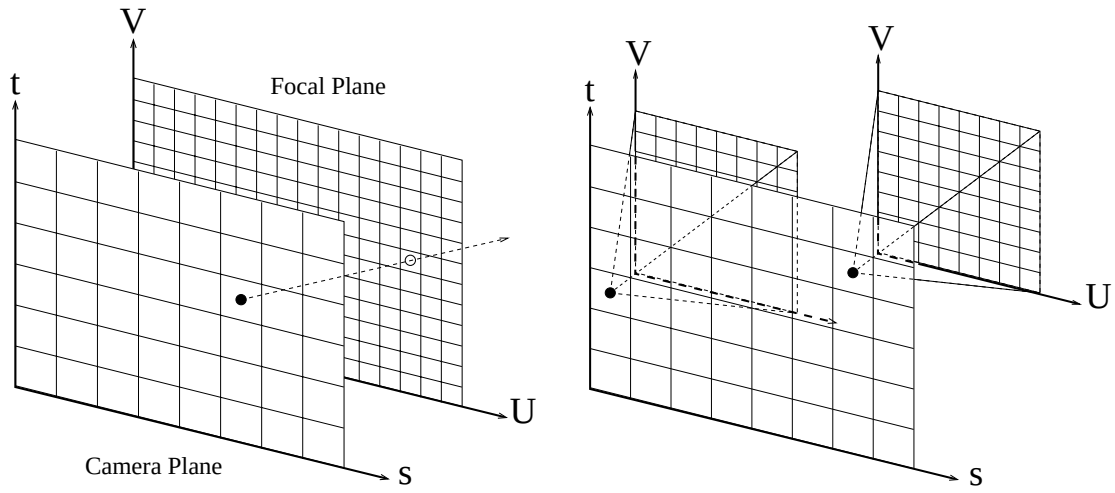

(a) fixed focal plane **(b)** local focal plane

Figure 5.1: The lumigraph is parameterized using a camera plane and a focal plane.

the standard rendering pipeline used by most real-time graphics hardware. We believe it should translate, in a relatively straightforward fashion, into a hardware implementation, allowing it to drive a holographic display system.

5.1 Generalized Lumigraph Rendering

The lumigraph, or light-field, as originally described by Gortler et.al. [46], and Levoy and Hanrahan [74], consisted of two fixed planes: a camera plane and a focal plane (Figure 5.1(a)). We discretize these planes with rectangular coordinate grids (s, t) and (U, V), respectively. The reasons for this odd notation will become apparent later. The lumigraph is stored as a four-dimensional array with data point (s, t, U, V) receiving the value of the light traveling from the scene, through point (U, V), and arriving at point (s, t). We modify the geometry used by Gortler and Levoy slightly by allowing the (U, V) plane to move

so that it is always centered on the current (s,t) point (Figure 5.1(b)). Perceptually, this will affect the parallax exhibited by the lumigraph. With the original geometry, objects near the focal plane will tend to maintain a fixed (U,V) position for all (s,t). With ours, as (s,t) changes, objects will tend to move at a rate inversely proportional to their depth. Note that this choice is made out of convenience, not necessity, and that the algorithms discussed in this chapter can be used, with a few alterations, with either layout. For lumigraphs with less than a 90 degree viewing frustum, this geometry is equivalent to the sample domain described in the previous chapter.

To understand what the computation of the lumigraph involves, we consider the rendering of a single triangle, as illustrated in Figure 5.2. Figure 5.3 shows the perspective views of the triangle from four points on the camera plane with fixed t and varying s. As we can see, the image shifts and distorts as s increases. If we do this for all s and stack the results, we see that the triangle sweeps out a volume in (s,U,V) space (Figure 5.4). If we allow t to vary as well, we obtain a four-dimensional hyper-volume in (s,t,U,V) space. We refer to this region as the triangle's *projected volume*.

Computing the lumigraph of this triangle requires determining all of the sample points that lie within the projected volume and setting the value of the appropriate data point. This process can be viewed as a set of four nested loops, one for each of the four dimensions. For a scene consisting of many triangles, we must, in the most naive case, perform this for every polygon, p. Thus, the basic structure of a lumigraph computation algorithm consists of five nested loops.

Of course, iterating over all possible combinations of s, t, U, V, and p would

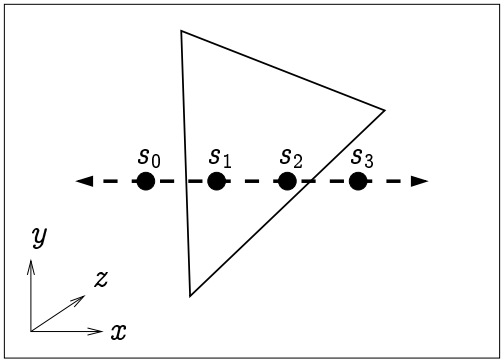

Figure 5.2: A triangular polygon positioned in space in front of the camera plane. It is tilted with respect to the lumigraph so that the top vertex is farthest and the bottom is closest. We examine the image seen from four points along a single horizontal row on the camera plane.

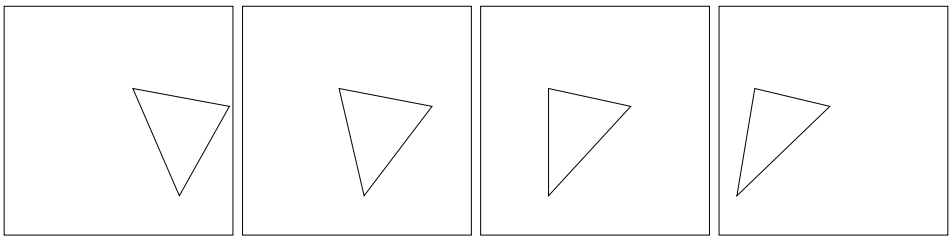

(a) s_0 **(b)** s_1 **(c)** s_2 **(d)** s_3

Figure 5.3: The perspective projection of the polygon as seen from each of the points in Figure 5.2. As we move from left to right, the projection shifts from right to left, and its shape changes due to the varying depths of the vertices.

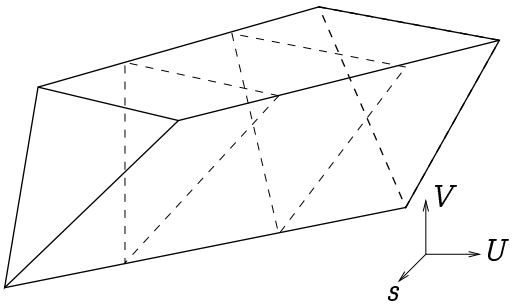

Figure 5.4: The triangle's projected volume. By stacking the projections from all s, we see that the polygon sweeps out a volume in (s, U, V) space. If we allow t to vary as well, we obtain a 4-dimensional volume in (s, t, U, V).

be prohibitively expensive. We therefore use a variety of operations, such as clipping, back-face culling, and spatial subdivision to limit the number of projection points which must be explicitly evaluated. In addition, when a similar operation is required for several points, all or part of the computation can be performed in an outer loop, allowing the results to be reused. By analyzing the basic structure of a particular lumigraph computation algorithm in terms of the loop nesting order and how these basic operations fit into the hierarchy, we can gain an understanding of how well the algorithm takes advantage of coherency. In the following section, we perform this analysis for several previous methods for generating lumigraphs.

5.2 Previous Work

In this section, we examine several lumigraph computation algorithms. Note that we are concerned only with their basic structure. A great number of key implementation details are omitted for the sake of brevity.

5.2.1 Ray Tracing

Gortler [46] used ray tracing to generate his lumigraphs. Conceptually, this is perhaps the simplest method available. For each (s, t, U, V) point, a ray is fired from (s, t) through (U, V), and the closest polygon intersection is found. Typically, some sort of spatial subdivision is used to limit the number of polygons which must be checked against the ray. This algorithm is summarized in Figure 5.5. The ordering of the outer loops is of no consequence. The important observation to make here is that the bulk of the work is performed in the inner-

```
for all (s, t, U, V) do
    for all p' ∈ {p'} ⊆ {p} determined by spatial subdivision do
        if intersect(p', s, t, U, V)
            shade(p', s, t, U, V)
        fi
    od
od
```

Figure 5.5: Basic structure of ray-tracing based lumigraph computation.

most loops. No effort is made to take advantage of coherence between adjacent (s, t, U, V) points.

5.2.2 2D Rendering

Another way to compute the lumigraph is to use multiple applications of a two-dimensional rendering algorithm (Figure 5.6(a)). We iterate over all points on the camera plane, generating perspective images for each point, each of which forms an (s, t) slice of the lumigraph. This allows us to exploit the same coherencies as the 2D routine, and to take advantage of graphics acceleration hardware. Levoy and Hanrahan [74] computed their light-fields in this way, using RenderMan to compute the 2D images.

Lucente [85] used a variation of this technique. His holograms had only horizontal parallax, so they possessed no V dimension. Instead of the making s and t the outermost loops, he used them as the inner loops (Figure 5.6(b)). For each V direction, the 2D renderer is used to generate an image with an oblique projection.

To see how such an algorithm takes advantage of coherency, we will examine the specific case of a generic z-buffer algorithm following the standard graphics

```
for all (s, t) do
    compute (U, V) image with perspective projection
od
```

(a)

```
for all V do
    compute (s, t) image with oblique projection
od
```

(b)

Figure 5.6: Computing a lumigraph as a series of independent two-dimensional images. (a) With (U, V) as the inner loop, we generate perspective images. (b) With (s, t), we use oblique projections.

pipeline. This is of particular interest to us, since it will later provide the inspiration for our own method. An outline of the algorithm is shown in Figure 5.7.

Following the example of Figure 5.6(a), the outermost loop iterates over all (s, t). For each one, a transformation matrix which converts from world space to camera space coordinates is constructed. Two-dimensional depth and color buffers are also initialized.

The enclosed 2D renderer proceeds to iterate over every polygon in the scene. Each is transformed into camera space, and back-face culling is applied to skip those not facing the camera point. That portion of the shading computation which can be interpolated across the polygon is performed at the vertices. The nature of these computations depends on the shading/lighting models used. The values obtained can be interpolated to any point on the polygon and used to determine the light reflected by that point towards the camera.

Next, the polygon is converted into (U, V) coordinates with a perspective transformation matrix and clipped against the U and V boundaries of the lumi-

```
for all (s, t)
    initialize buffers
    for all p
        transform to camera space
        back-face culling
        (partial) shading
        perspective transform
        clipping
        for all V within polygon bounds
            determine intersection of polygon with scan-line V
            for all U within slice bounds
                if depth(p, s, t, U, V) < zbuffer(U, V)
                    complete shading and update buffers
                fi
            od
        od
    od
    copy color buffer to lumigraph
od
```

Figure 5.7: Overview of lumigraph computation with 2D z-buffer.

graph. It is then scan converted to obtain all sample points within its interior. The depth at each point is compared with the corresponding entry in the depth buffer. If it is closer, the shading computation is completed and used to set the color buffer entry, while the depth buffer entry is updated with the new depth value. Once all points on all polygons have been processed, the color buffer is copied to the (s, t) slice of the lumigraph, and the process begins again with the next camera point.

As we can see from the figure, this algorithm takes advantage of coherence in the (U, V) dimensions by performing as much of the computation as possible outside of the U and V loops. It has the additional benefit that z-buffer renderers are available in hardware for most computers, allowing a moderately efficient lumigraph renderer to be constructed. Nevertheless, this is still essentially a 2D

method, and cannot utilize coherence in s and t. This is unfortunate, as the differences between images from adjacent camera points will be small, suggesting a large source of potential savings in computation time.

5.2.3 Multiple Viewpoint Rendering

Halle's [49] multiple viewpoint rendering (MVR) algorithm utilizes coherence in additional dimensions while still performing primarily two-dimensional operations that can take advantage of graphics hardware. An overview is shown in Figure 5.8.

We begin by performing view-independent shading computations for each vertex in the scene, storing the results with the polygons. We then iterate over all the t rows of the lumigraph, rendering each. For a given t, we begin by initializing a set of slice tables, one for each V value. These tables will contain a list of the polygons that intersect image row V as seen from camera row t.

We fill in these tables by iterating over all polygons in the scene. For each one, we perform a perspective transformation of the polygon as seen from the minimum and maximum s values along row t. Given a row V, we can determine its intersection with these two projected polygons, obtaining a pair of line segments. From these, we can interpolate the intersection of the polygon with V as seen from any point s along this row of the lumigraph. We do this for every V, storing a record of the line segments in the corresponding slice table.

Once every polygon has been sliced, we process each slice table, scan converting all of its members. We initialize an ordinary set of two-dimensional color and depth buffers. Each record in the table defines a "polygon slice track", a four-sided polygon in s and U. This can be scan converted just like any other

```
for all p
    view-independent lighting/shading
od
for all t
    initialize slice tables
    for all p
        perspective transform
        for all V within polygon bounds
            slice polygon and add to table V
        od
    od
    for all V
        initialize buffers
        for all slice tracks in table V
            back-face culling
            for all s
                determine intersection of slice track with scan-line s
                for all U within slice bounds
                    if depth(p, s, t, U, V) < zbuffer(s, U)
                        do view-dependent shading and update buffers
                    fi
                od
            od
        od
        copy color buffer to lumigraph
    od
od
```

Figure 5.8: Overview of Halle's MVR algorithm

polygon. For each interior point, a depth comparison is performed, and if it passes, view-dependent shading is performed for the point and the buffers are updated. Once all entries in the slice table have been processed, the color buffer is copied to the (t, V) slice of the lumigraph, and we proceed to the next V.

This algorithm takes advantage of coherence in three and four dimensions, but does so at the cost of requiring additional memory. For example, the view-independent shading computations are performed only once, instead of once

for each value of (s, t), but we need sufficient storage to hold the results for every polygon. Perspective transformation and the vertical scanning can be performed once per t, rather than per (s, t), but the transformed and sliced polygons must be kept in slice tables until they are needed. The shading information requires storage proportional to the number of polygons, while the slice tables require storage proportional to the number of polygons multiplied by the number of V slices. Halle utilized existing graphics hardware to implement portions of his algorithm, but these memory requirements will make it very difficult to design an efficient, completely hardware-based implementation. The number of polygons is theoretically unbounded, so unless we place an arbitrary limit on it, we will need to rely on the computer's own memory for this additional storage.

Although this algorithm performs significantly better than that of the previous section, it still does not take full advantage of coherence in the lumigraph. Primarily, the t dimension remains largely unexploited. In addition, texture and shader information for a polygon must be loaded every time a slice of the polygon is processed. This can be done more efficiently if all slices from a polygon are handled at once. Finally, MVR does not utilize clipping, which can quickly eliminate many polygons, or portions of polygons, with minimal computation.

5.3 Proposed Algorithm

There is a limit to what can be achieved by adapting existing rendering systems to the problem of generating a lumigraph. We believe that the only way to perform this computation at the speed required by a real-time three-dimensional

```
initialize buffers
for all p
    transform to hologram space
    clip to near plane
    view-independent shading of vertices
    back-face culling
    determine projected volume
    clipping
    (partial) view-dependent shading of vertices
    for all (s, t, U, V)
        if depth(p, s, t, U, V) < zbuffer(s, t, U, V)
            complete shading and update buffers
        fi
    od
od
```

Figure 5.9: General overview of our algorithm. A more detailed description can be found in Figure 5.21.

display is to develop new hardware and software specifically designed for the lumigraph. We propose a new algorithm which utilizes a 4D, rather than 2D, z-buffer. We parallel, as much as possible, the standard rendering pipeline (Figure 5.7), but make use of coherence in all four dimensions. Our goal is to produce an algorithm which can be implemented in hardware to form the basis of a holographic graphics accelerator.

Our algorithm's basic structure is shown in Figure 5.9. The polygon iteration has been made the outermost loop, and the shading, projection, culling, and clipping operations have been moved with it. Given the current trend towards scenes consisting of many small polygons, these operations account for the bulk of the computation time required for a polygon. By performing them on the polygon's entire projected volume at once, rather than on individual two-dimensional slices of it, we can obtain significant savings. At the same time, we

minimize overhead by requiring each polygon, and its accompanying texture and shader information, to be loaded only a single time. Once the projection has been obtained, it is scan-converted in a manner similar to the 2D case.

5.4 Projected Volume

Implementing this algorithm requires the ability to represent, manipulate, and scan convert a polygon's projected volume. Recall that we define the projected volume of a polygon to be all points (s, t, U, V) such that (U, V) lies within the perspective projection of the polygon as seen from camera point (s, t).

To define the perspective transformation, we use the matrix of Blinn [16, page 188]

$$P_{(0,0)} = \begin{bmatrix} \cos\Theta & 0 & 0 & 0 \\ 0 & \cos\Theta & 0 & 0 \\ 0 & 0 & \frac{\sin\Theta}{1-\frac{z_n}{z_f}} & -\frac{z_n \sin\Theta}{1-\frac{z_n}{z_f}} \\ 0 & 0 & \sin\Theta & 0 \end{bmatrix},$$

where Θ is the limit of the viewing frustum, and z_n and z_f are the near and far clipping planes, respectively. Applying this matrix to a point $[x, y, z]^T$ yields screen space coordinates $[u, v, z', w]^T = P_{(0,0)}[x, y, z, 1]^T$. We apply a factor of $\frac{1}{w}$ to obtain homogeneous coordinates $(U, V, Z, Q) = (\frac{u}{w}, \frac{v}{w}, \frac{z'}{w}, \frac{1}{w})$. (U, V) is the point's projected position on the screen, while Z provides a measure of it's depth, and Q can be used to convert back from homogeneous to real space.

To perform a perspective projection from an arbitrary point, (s, t), on the

camera plane, we must first translate by $(-s, -t, 0)$, yielding the new matrix:

$$P_{(s,t)} = \begin{bmatrix} \cos\Theta & 0 & 0 & 0 \\ 0 & \cos\Theta & 0 & 0 \\ 0 & 0 & \frac{\sin\Theta}{1-\frac{z_n}{z_f}} & -\frac{z_n \sin\Theta}{1-\frac{z_n}{z_f}} \\ 0 & 0 & \sin\Theta & 0 \end{bmatrix} \begin{bmatrix} 1 & 0 & 0 & -s \\ 0 & 1 & 0 & -t \\ 0 & 0 & 1 & 0 \\ 0 & 0 & 0 & 1 \end{bmatrix}$$

$$= \begin{bmatrix} \cos\Theta & 0 & 0 & -s\cos\Theta \\ 0 & \cos\Theta & 0 & -t\cos\Theta \\ 0 & 0 & \frac{\sin\Theta}{1-\frac{z_n}{z_f}} & -\frac{z_n \sin\Theta}{1-\frac{z_n}{z_f}} \\ 0 & 0 & \sin\Theta & 0 \end{bmatrix}.$$

Thus, given a real-space point (x, y, z) and camera point (s, t), we obtain a set of lumigraph coordinates with associated depth and Q values:

$$(s, t, U, V;\ Z, Q) = \left(s, t, \cot\Theta\frac{(x-s)}{z}, \cot\Theta\frac{(y-t)}{z};\right.$$
$$\left.\left(\frac{z-z_n}{z}\right)\left(\frac{z_f}{z_f-z_n}\right), \frac{1}{z\sin\Theta}\right).$$

The trigonometric factors, as well as the factor of $\frac{z_f}{z_f - z_n}$, are identical for all camera and world space points. For brevity and the sake of simplifying this discussion, we therefore temporarily omit these terms, bearing in mind that we must still include them in an actual implementation of this algorithm. This yields

$$(s, t, U, V;\ Z, Q) = \left(s, t, \frac{x-s}{z}, \frac{y-t}{z};\ \frac{z-z_n}{z}, \frac{1}{z}\right).$$

Let us consider the projected volume of a triangle with vertices $\vec{x}_i = (x_i, y_i, z_i)$, $i \in \{0, 1, 2\}$, as seen from a triangular region of the lumigraph with vertices $\vec{s}_i = (s_j, t_j)$, $j \in \{0, 1, 2\}$. Projected volumes involving polygons or lumigraph regions with more vertices can be constructed by adding smaller regions of

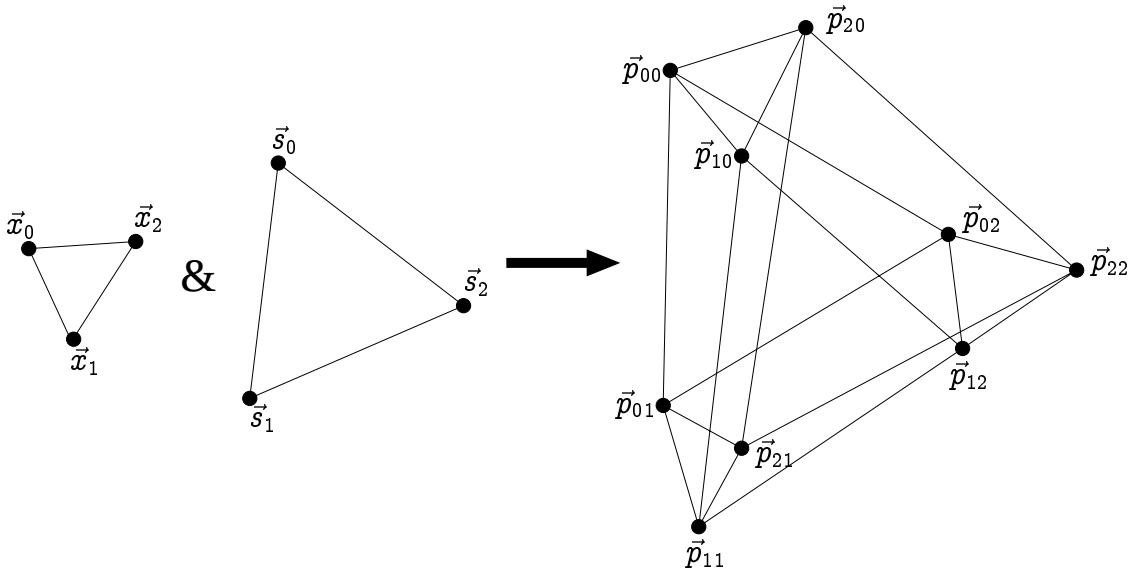

Figure 5.10: The projected volume of a triangular polygon as seen from a triangular portion of the camera plane. This is a four-dimensional region, shown here projected orthographically into 2D.

this form. This volume (Figure 5.10) has nine vertices formed by the projection of each polygon vertex from each corner of the lumigraph region, $\vec{p}_{ij} = \left(s_j, t_j, \frac{x_i - s_j}{z_i}, \frac{y_i - t_j}{z_i}; \frac{z_i - z_n}{z_i}, \frac{1}{z_i}\right)$. These vertices are connected by 18 edges of two different types (Figure 5.11). The first type is formed by the projection of an edge of the polygon from a corner of the lumigraph, while the second is formed by a corner of the polygon as seen from an edge of the lumigraph. Similarly, these edges combine to form 15 faces of three different types (Figure 5.12), which in turn bound 6 volumes of two types (Figure 5.13). These volumes form the hyperfaces of the complete, four-dimensional projected volume.

It is well known that perspective transformations map lines to lines and polygons to polygons. Therefore, the first type of edge and the first type of face will be straight and planar, respectively, because they correspond to the projection of the polygon from a fixed camera point. We can easily see that this

(a) **(b)**

Figure 5.11: Examples of the two types of edges in the projected volume. (a) A polygon edge seen from a lumigraph vertex. (b) A polygon vertex seen from a lumigraph edge.

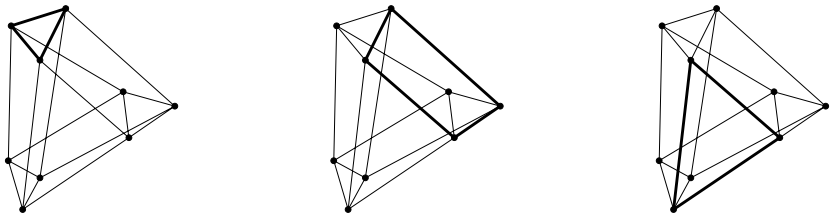

(a) **(b)** **(c)**

Figure 5.12: Examples of the three types of faces in the projected volume. (a) The polygon as seen from a lumigraph vertex. (b) An edge of the polygon as seen from an edge of the lumigraph. (c) A vertex of the polygon as seen from the entire lumigraph.

(a) **(b)**

Figure 5.13: Examples of the two types of hyperfaces in the projected volume. (a) The polygon as seen from an edge of the lumigraph. (b) An edge of the polygon as seen from the entire lumigraph.

will also hold for the second type of edge and the third type of face by observing that as the camera moves in a linear fashion, the projection of a single point in the scene will move across the screen linearly.

However, the second type of face will not be planar. This is most easily proved by example. Consider polygon vertices $(0,0,2)$ and $(0,1,3)$, and lumigraph vertices $(0,0)$ and $(1,1)$. If we let $z_n = 1$, then the corresponding projected points become $(0,0,0,0;\ \frac{1}{2},\frac{1}{2})$, $(0,0,\frac{1}{3},0;\ \frac{2}{3},\frac{1}{3})$, $(1,1,-\frac{1}{2},-\frac{1}{2};\ \frac{1}{2},\frac{1}{2})$, and $(1,1,0,-\frac{1}{3};\ \frac{2}{3},\frac{1}{3})$. These points are clearly not coplanar, so any face containing them must be curved. Specifically, they form a portion of a hyperbolic paraboloid. We therefore conclude that, in general, the projected volume of a polygon is not a hyper-polyhedron.

In four dimensions, even a polyhedron can require quite complex data structures. If the volume is curved, it will be very difficult to represent and manipulate. We could approximate it as a polyhedron, as is often done when rendering curved surfaces, but the resulting lumigraph will have very noticable gaps between polygons, as well as other more subtle errors. We therefore would like to find a way to transform the projected volume so that its faces become planar.

5.5 Homogeneous Projected Volume

To transform the projected volume into a more tractable form, we convert the s and t dimensions to homogeneous coordinates as well as u and v. We obtain

$$(S,T,U,V;\ Z,Q) = (\frac{s}{z},\frac{t}{z},U,V;\ Z,Q) \tag{5.1}$$

$$= \left(\frac{s}{z},\frac{t}{z},\frac{x-s}{z},\frac{y-t}{z};\ \frac{z-z_n}{z},\frac{1}{z}\right). \tag{5.2}$$

Note that this is no longer in the same space as that used to discretize the lumigraph. We will need to take this fact into account when we come to the scan conversion step. However, this does, as we shall prove, have the desired effect: the projected volume is now a hyper-polyhedron.

Consider a point, $\vec{x}$, on the polygon. We can represent this point as a weighted sum, with coefficients a_i, of the corner vertices:

$$\vec{x} = \sum a_i \vec{x}_i \qquad 0 \le a_i \le 1 \qquad \sum a_i = 1. \tag{5.3}$$

Similarly, any point in the lumigraph region can be represented as a weighted sum of the lumigraph corners:

$$\vec{s} = \sum b_j \vec{s}_j \qquad 0 \le b_j \le 1 \qquad \sum b_j = 1. \tag{5.4}$$

Combining Equations (5.2), (5.3), and (5.4) yields a point in the projected volume given by

$$\vec{p} = \left(\frac{\sum b_j s_j}{\sum a_i z_i}, \frac{\sum b_j t_j}{\sum a_i z_i}, \frac{(\sum a_i x_i) - (\sum b_j s_j)}{\sum a_i z_i}, \frac{(\sum a_i y_i) - (\sum b_j t_j)}{\sum a_i z_i}; \frac{(\sum a_i z_i) - z_n}{\sum a_i z_i}, \frac{1}{\sum a_i z_i} \right). \tag{5.5}$$

A bit of algebraic manipulation transforms this to

$$\begin{aligned} \vec{p} &= \sum_i \sum_j \frac{a_i b_j z_i}{a_0 z_0 + a_1 z_1 + a_2 z_2} \left(\frac{s_j}{z_i}, \frac{t_j}{z_i}, \frac{x_i - s_j}{z_i}, \frac{y_i - t_j}{z_i}; \frac{z_i - z_n}{z_i}, \frac{1}{z_i} \right) \\ &= \sum_i \sum_j \frac{a_i b_j z_i}{a_0 z_0 + a_1 z_1 + a_2 z_2} \vec{p}_{ij}. \end{aligned}$$

This tells us that any point in the projected volume can be written as a weighted sum of the volume's corner points. Furthermore, given the constraints on a_i and b_j, and the condition that $z_i > 0$, we can easily show that the weighting coefficients, $c_{ij} = \frac{a_i b_j z_i}{a_0 z_0 + a_1 z_1 + a_2 z_2}$, obey $0 \le c_{ij} \le 1$ and $\sum c_{ij} = 1$. Therefore, all

point in the projected volume lie inside the polyhedron formed by connecting the volume's vertices by linear / planar edges / faces.

Conversely, suppose we have a point, $\vec{p}$, within this polyhedron. In general, there are an infinite number of ways to represent this as a weighted sum of the corner points:

$$\vec{p} = \sum c_{ij}\vec{p}_{ij} \qquad 0 \le c_{ij} \le 1 \qquad \sum c_{ij} = 1. \tag{5.6}$$

One possible way is to find coefficients a'_i and b'_j, where $0 \le a'_i \le 1$, $0 \le b'_j \le 1$, $\sum a'_i = \sum b'_j = 1$, such that coefficients $c_{ij} = a'_i b'_j$ satisfy Equation (5.6). In regions where the projected volume is degenerate (i.e. when two vertices coincide or where it folds through itself) these coefficients may not be unique, but at least one solution exists for all possible $\vec{p}$. From this, we can obtain coefficients, $a_i = \frac{a'_i Q_i}{a'_0 Q_0 + a'_1 Q_1 + a'_2 Q_2}$ and $b_j = b'_j$, which satisfy Equations (5.3) through (5.5). This means that they define points in the polygon and lumigraph, respectively, which together project to $\vec{p}$. Thus, any point in the polyhedron formed by the projected volume's corners is a member of the projected volume.

These two facts combine to prove that the projected volume, in (S, T, U, V) space, is a polyhedron. These equations further show that the Z and Q values associated with each point in the volume can be found with the same summation coefficients. This tells us that these values will vary linearly between any two points in the projection, just as in the case of an ordinary, two-dimensional, perspective projection. The depth is not the only thing that can be interpolated in this way. Again just as with a 2D projection, we can multiply shading, texture coordinates, or other values by $\frac{1}{w}$, interpolate them linearly, and divide by Q to obtain their value at any point in the projected volume.

The projected volume will either be convex or consist of two convex lobes.

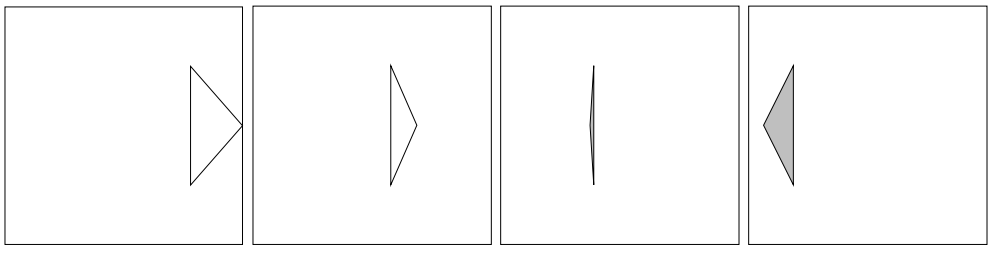

(a) **(b)** **(c)** **(d)**

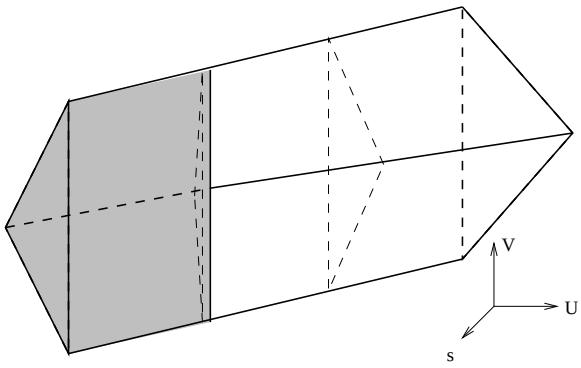

(e)

Figure 5.14: As in Figures (5.2)–(5.4), we see multiple projections of a polygon, this time one that is nearly perpendicular to the camera plane. (a)–(d) As the camera moves, we see first the front face of the polygon, and then the back face. (e) The projected volume folds through itself, forming two lobes.

The latter case occurs when both the front and back faces of the polygon are visible from different points on the lumigraph. The volume will appear to fold through itself at the point(s) where the polygon is seen edgewise. This is shown in Figure 5.14 for fixed T. Back-face culling can be performed by eliminating the corresponding lobe.

5.6 Simplices and Simploids

Even in polyhedral form, the projected volume is still quite complex, and we can expect it to become even more so after applying clipping. Note that in all the algorithms discussed in Section 5.2, at no time are any operations performed on a cross-section of the volume with dimensionality higher than two. There is a very good reason for this. A polygon can be represented with nothing more than a number of vertices and an ordered vertex list. If we restrict ourselves to triangles, as many renderers do, then even the vertex count is unnecessary. The connectivity between vertices is implicitly defined by the list. Each is connected to exactly two others, the ones immediately preceding and following it. This structure makes it very easy to perform operations on polygons.

By contrast, as we move to higher dimensions, the complexity increases rapidly. The connectivity is no longer implicit, requiring us to store a list of edges. For a three-dimensional polyhedron, we also need to know how these edges connect to form faces. In four dimensions, we must have all of this, plus information about how the faces combine to form hyperfaces. At this point, the objects become difficult to even conceptualize, let alone encode algorithmically. Performing operations on them requires a great deal of bookkeeping involving highly convoluted data structures. Trying to implement this in hardware would be virtually impossible.

We therefore wish to find a more tractable way to represent a projected volume. To do this, we will turn to *simplices* and *simploids* to act as the fundamental geometric primitives of our rendering system. We provide a brief overview of these structures here. For more information, we refer the reader to Hanson [50] and Moore [93].

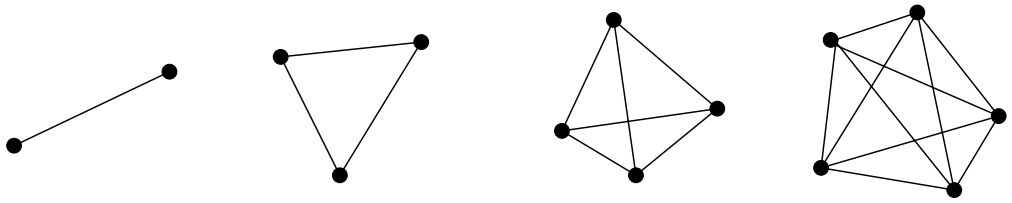

(a) 1-simplex **(b)** 2-simplex **(c)** 3-simplex **(d)** 4-simplex

Figure 5.15: An n-simplex is an n-dimensional polyhedron with $n+1$ vertices and an edge between every vertex pair.

An n-simplex is the simplest possible n-dimensional polyhedron. It is composed of $n+1$ vertices, with an edge between every vertex pair. For example, a one-dimensional simplex is a line segment, a 2-simplex is a triangle, and a 3-simplex is a tetrahedron (Figure 5.15). Because of this uniform connectivity, simplices can be represented with only an unordered vertex list, and are very easy to manipulate.

A simploid is a polyhedron that is isomorphic to the product of one or more simplices. Let $n_1, n_2, \ldots n_m$ be positive integers and let $N = \sum_1^m n_j$. Then an $(n_1, n_2, \ldots n_m)$-simploid is an N-dimensional polyhedron with $\prod_1^m (n_j + 1)$ vertices. We label these vertices $i_1 i_2 \ldots i_m$, where $0 \leq i_j < n_j$. Two vertices in the simploid are connected by an edge if and only if their labels differ in only one index. An n-simplex is a special case of an n-dimensional simploid. Figure 5.16 shows the remaining types of simploids up to four dimensions, and illustrates their relation to lower dimensional simplices. The (2,2)-simploid should look familiar, as this is structure of the projected volume which we have been discussing, that of a triangle as seen from a triangular region of the lumigraph. In addition, we note that the (2,1,1)-simploid corresponds to the projected volume of a triangle as seen from a rectangular region.

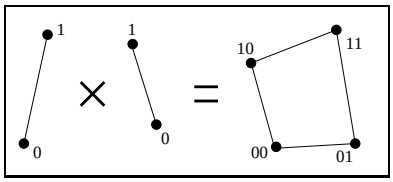

(a) (1,1)-simploid

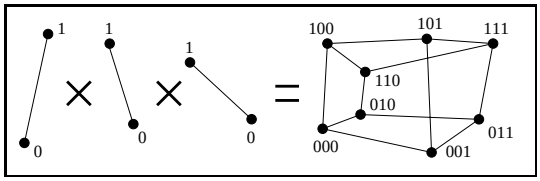

(b) (1,1,1)-simploid

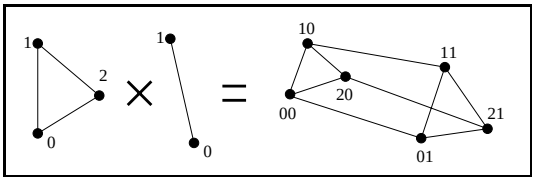

(c) (2,1)-simploid

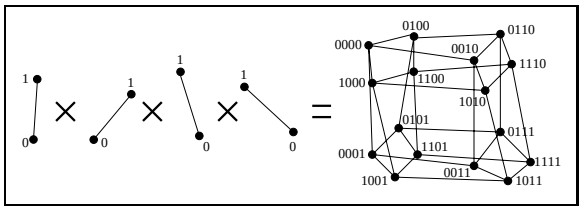

(d) (1,1,1,1)-simploid

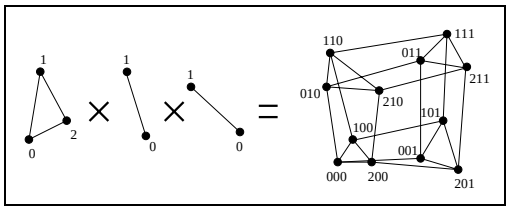

(e) (2,1,1)-simploid

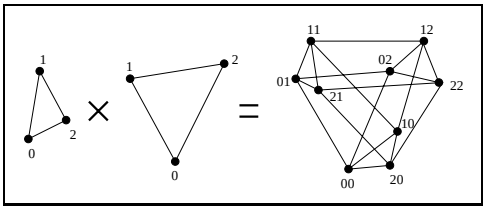

(f) (2,2)-simploid

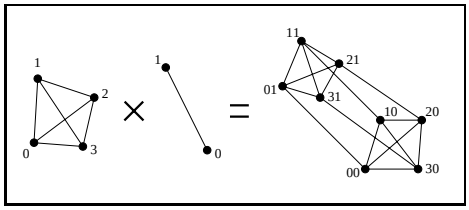

(g) (3,1)-simploid

Figure 5.16: A simploid is isomorphic to the product of one or more simplices.

5.6.1 Subdivision of a simploid

Any simploid can be subdivided into a set of simplices [93]. The algorithm for performing this operation for an arbitrary simploid is relatively simple, but given the rather small number of simploid types that we will be using, and their low dimension, it is more efficient for us to simply use a lookup table for each type of simploid. Figure 5.17 provides subdivisions for (2,1,1)-, (2,2)-, and (2,1)-simploids. These subdivisions are not unique, as can easily seen by examining the symmetries in the simploids. In general, one might wish to choose between the possible subdivisions for a given simploid based on some optimization criteria, such as which produces simplices with the lowest eccentricity. However, in our implementation, we opt to use a single subdivision for all simploids of a given type.

5.6.2 Clipping and slicing a simplex

Suppose we intersect an n-simplex with a plane, so that n_1 vertices lie on one side of the plane and $n_2 = n - n_1 + 1$ lie on the other. The plane divides the simplex into an $(n_1, n_2 - 1)$-simploid and an $(n_2, n_1 - 1)$-simploid. The region of intersection is an $(n_1 - 1, n_2 - 1)$-simploid. These simploids can be subdivided into simplices as in the previous subsection. Thus, clipping or slicing a simplex yields a new set of simplices. Figure 5.18 lists the simplices resulting from the different ways a 4-simplex can be clipped against a plane. Figure 5.19 and Figure 5.20 show the results of taking a slice of a 4- or 3-simplex, respectively.

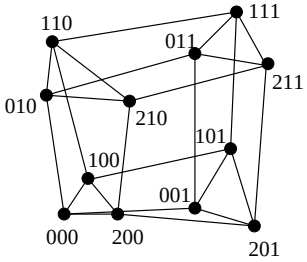

(000, 001, 011, 111, 211)
(000, 001, 101, 111, 211)
(000, 001, 101, 201, 211)
(000, 010, 011, 111, 211)
(000, 010, 110, 111, 211)
(000, 010, 110, 210, 211)
(000, 100, 101, 111, 211)
(000, 100, 101, 201, 211)
(000, 100, 110, 111, 211)
(000, 100, 110, 210, 211)
(000, 100, 200, 201, 211)
(000, 100, 200, 210, 211)

(a) Subdivision of a (2,1,1)-simploid into twelve 4-simplices

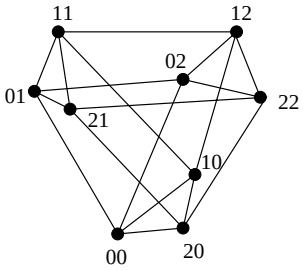

(00, 01, 02, 12, 22)
(00, 01, 11, 12, 22)
(00, 01, 11, 21, 22)
(00, 10, 11, 12, 22)
(00, 10, 11, 21, 22)
(00, 10, 20, 21, 22)

(b) Subdivision of a (2,2)-simploid into six 4-simplices

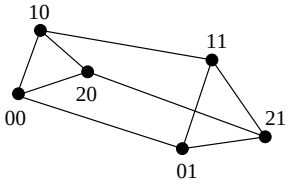

(00, 01, 11, 21)
(00, 10, 11, 21)
(00, 10, 20, 21)

(c) Subdivision of a (2,1)-simploid into three 3-simplices

Figure 5.17: The three types of simploids which our algorithm uses and their corresponding subdivision into sets of simplices.

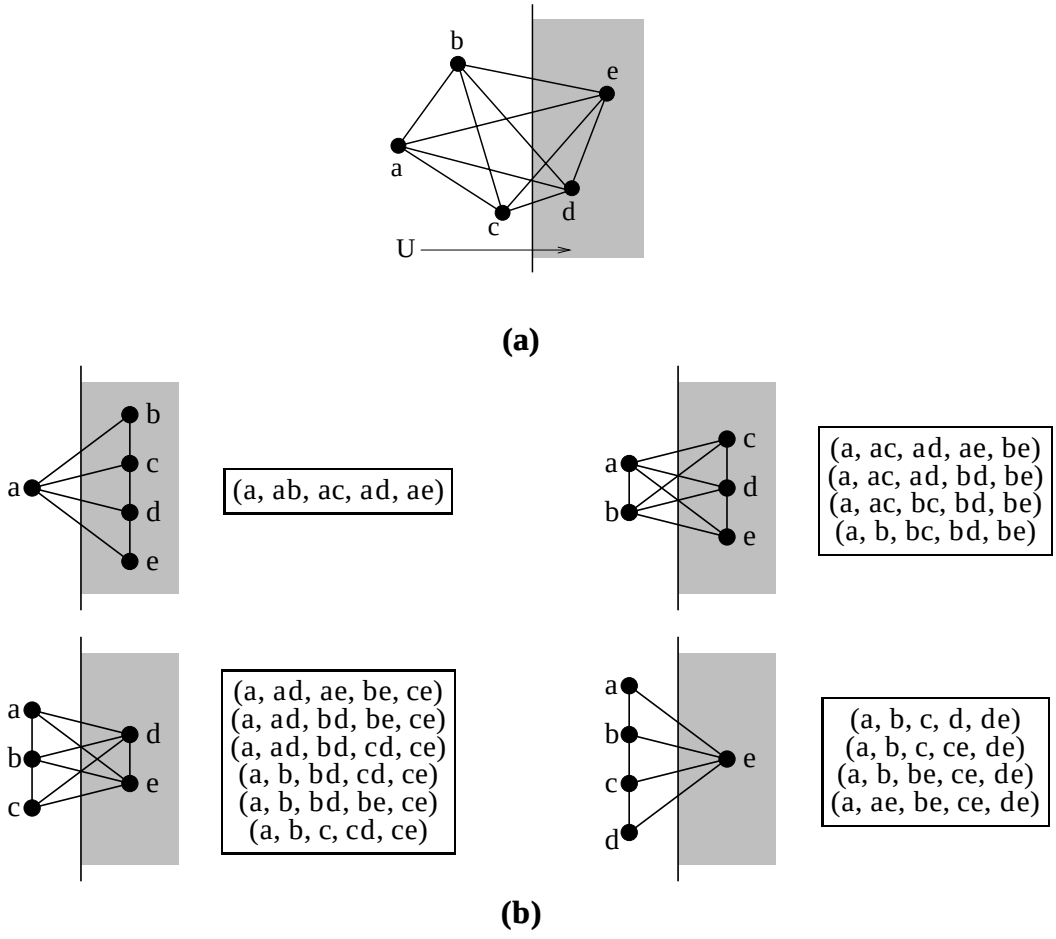

Figure 5.18: Clipping of a 4-simplex is shown here for the specific case of the upper U clipping plane. The other planes are handled similarly. (a) The vertices are sorted in order of increasing U, and labeled 'a' through 'e'. (b) We assign label 'ab' to the point at which the plane intersects the edge between a and b, and so on for all the vertex pairs. Depending on the number of vertices inside the plane, different sets of simplices result, as shown.

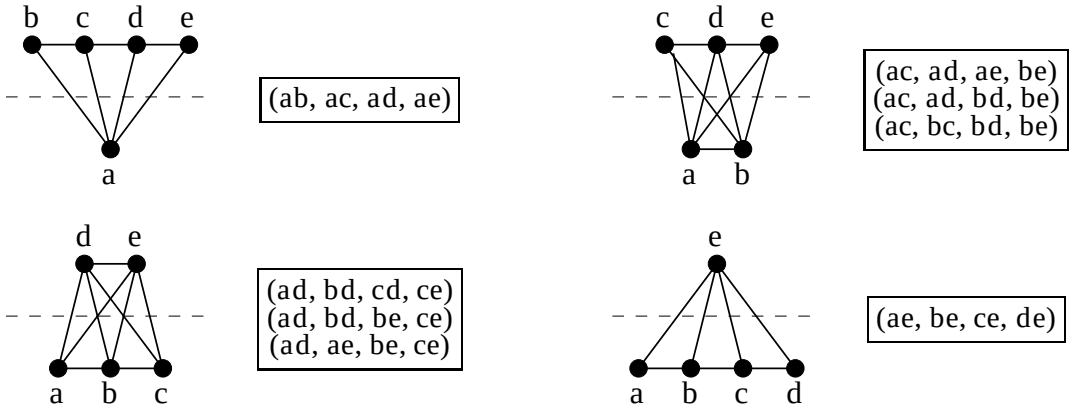

Figure 5.19: Slicing a 4-simplex yields one or three 3-simplices.

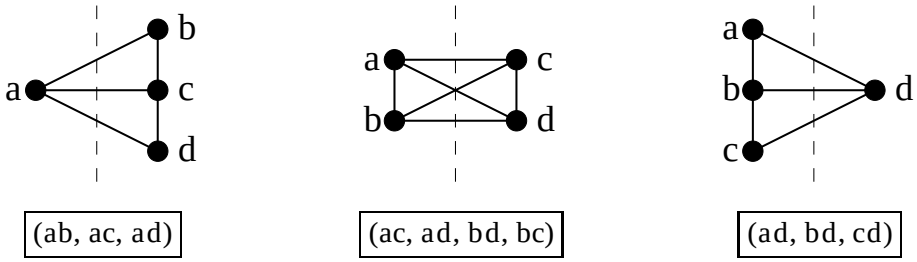

Figure 5.20: Slicing a 3-simplex yields a triangle or quadrilateral.

5.7 Complete Algorithm

We are now ready to discuss our algorithm (Figure 5.21) in detail. We begin by initializing a set of four-dimensional depth and color buffers. We then iterate over each triangle in the scene, transforming it into hologram space and clipping it the the near plane. Depending on the shading model, all or part of the view-independent shading computation is now performed at the triangle's vertices.

5.7.1 Projection / Back-face culling

Next, we compute the projected volume while performing back-face culling. Recall from Figure 5.14 that, when both the front and back faces of the polygon

```
initialize buffers
for all p
    transform to hologram space
    clip to near plane
    view-independent shading of vertices
    determine projected volume with back-face culling
    partial view-dependent shading
    subdivide into queue of 4-simplices
    for all members of queue
        clip against U and V bounds
    od
    for all members of queue
        for all V within simplex bounds
            slice 4-simplex at V, generating queue of 3-simplices
            for all 3-simplices
                for all U within simplex bounds
                    slice 3-simplex at U, generating one or two triangles
                    for each triangle
                        convert from (S, T) to (s, t)
                        for all t within triangle bounds
                            determine endpoints for slice at t
                            for all s within slice
                                if depth(p, s, t, U, V) < zbuffer(s, t, U, V)
                                    complete shading and update buffers
                                fi
                            od
                        od
                    od
                od
            od
        od
    od
od
```

Figure 5.21: Our complete rendering algorithm.

are visible from different points on the lumigraph, the projected volume can fold through itself, yielding front- and back-face lobes. The region at which this fold occurs corresponds to the points on the lumigraph at which the polygon is seen edge on. This is simply the line at which the polygon and camera planes intersect. We can therefore perform back-face culling by considering only the lumigraph region on the appropriate side of this line.

Figure 5.22 illustrates the five basic cases for this line to cross the lumigraph's (s,t) range. If the entire range is in the back-face half-plane, the triangle is culled. Otherwise, we obtain a triangular or quadrilateral lumigraph region, or a five-sided region which can be split into one of each of these two types. Given a triangular polygon, these regions will produce projected volumes that are (2,2)- and (2,1,1)-simploids, respectively.

We compute the projection of the triangle's vertices from each of the corners of this region to obtain the vertices of the projected volume. Again depending on the shading model, those portions of the view-dependent shading which can be interpolated between viewpoints are now computed for each projection point. We then use the subdivision scheme defined in Section 5.6.1 to convert the projected volume into a queue of 4-simplices. The resulting simplices are listed in Figure 5.22.

5.7.2 Clipping

Next, we iterate four times over the queue we have created, performing clipping for each of the U and V boundaries of the lumigraph. During the first iteration, any simplex which lies entirely outside the upper U bound is simply discarded, while any that lies entirely inside is left alone. Those that intersect the edge

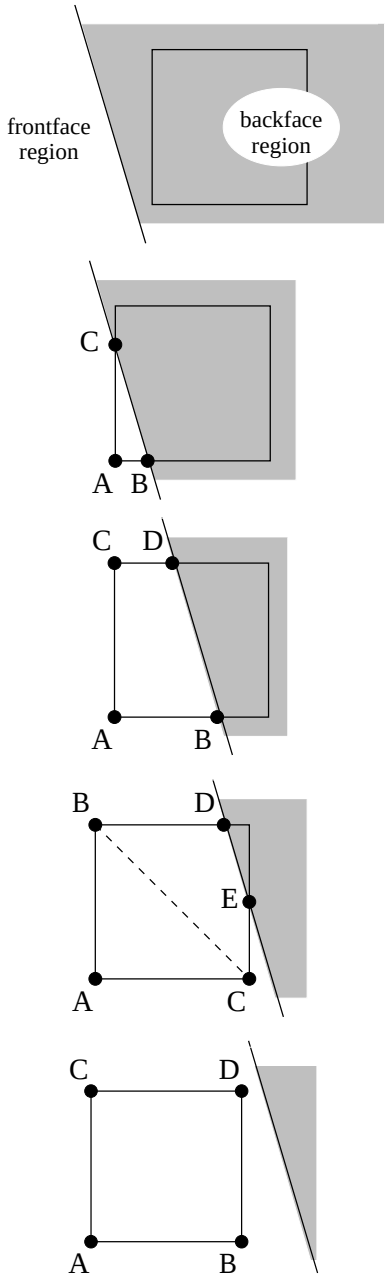

polygon discarded

(A0, A1, A2, B2, C2)	
(A0, A1, B1, B2, C2)	
(A0, A1, B1, C1, C2)	
(A0, B0, B1, C1, C2)	
(A0, B0, B1, B2, C2)	
(A0, B0, C0, C1, C2)	

(A0, A1, A2, B2, D2)	(A0, A1, A2, C2, D2)
(A0, A1, B1, B2, D2)	(A0, A1, B1, D1, D2)
(A0, A1, C1, C2, D2)	(A0, A1, C1, D1, D2)
(A0, B0, B1, B2, D2)	(A0, B0, B1, D1, D2)
(A0, B0, D0, D1, D2)	(A0, C0, C1, C2, D2)
(A0, C0, C1, D1, D2)	(A0, C0, D0, D1, D2)

(A0, A1, A2, B2, C2)	(A0, A1, B1, B2, C2)
(A0, A1, B1, C1, C2)	(A0, B0, B1, C1, C2)
(A0, B0, B1, B2, C2)	(A0, B0, C0, C1, C2)
(B0, B1, B2, C2, E2)	(B0, B1, B2, D2, E2)
(B0, B1, C1, C2, E2)	(B0, B1, C1, E1, E2)
(B0, B1, D1, D2, E2)	(B0, B1, D1, E1, E2)
(B0, C0, C1, C2, E2)	(B0, C0, C1, E1, E2)
(B0, C0, E0, E1, E2)	(B0, D0, D1, D2, E2)
(B0, D0, D1, E1, E2)	(B0, D0, E0, E1, E2)

(A0, A1, A2, B2, D2)	(A0, A1, A2, C2, D2)
(A0, A1, B1, B2, D2)	(A0, A1, B1, D1, D2)
(A0, A1, C1, C2, D2)	(A0, A1, C1, D1, D2)
(A0, B0, B1, B2, D2)	(A0, B0, B1, D1, D2)
(A0, B0, D0, D1, D2)	(A0, C0, C1, C2, D2)
(A0, C0, C1, D1, D2)	(A0, C0, D0, D1, D2)

Figure 5.22: Back-face culling is performed by determining where the plane of the polygon intersects the camera plane. If the lumigraph region lies entirely in the back-face half-plane, the polygon is discarded. Otherwise, the projected volume of the polygon (whose vertices are labeled 0 through 2) is found as seen from the portion of the lumigraph within the front-face half-plane. Depending on the number of vertices of this region, the projected volume is split into 6, 12, or 18 4-simplices, as shown.

are clipped as per Section 5.6.2, and replaced in the queue by a new set with between one and six simplices. This process is then repeated for the lower U bound and both V bounds.

5.7.3 Scanning in U and V

We now proceed to iterate over every simplex in the queue, scan converting them into the buffers. For each one, we sort its vertices in order of increasing V. This separates the simplex into 4 regions between each pair of vertices. In each of these intervals, we increment over all integral values of V, slicing as in Figure 5.19, obtaining a new queue of one or three 3-simplices.

We perform a similar process on the 3-simplices. The vertices of each one is sorted in order of increasing U. We then iterate over all U values within the simplex's range, slicing as in Figure 5.20 to obtain one or two triangles.

5.7.4 Scanning in s and t

Before we scan convert these triangles, we must convert them from homogeneous (S, T) coordinates to the (s, t) coordinates used to discretize the lumigraph by dividing them by their associated Q value. Unfortunately, after this transformation the triangle is no longer polygonal (Figure 5.23). However, the curves that form its edges are constrained in such a way that it will still be possible to scan convert it in a manner similar to an ordinary polygon.

Let $(S_0, T_0;\ Z_1, Q_0)$ and $(S_1, T_1;\ Z_1, Q_1)$ be the endpoints of a line segment in

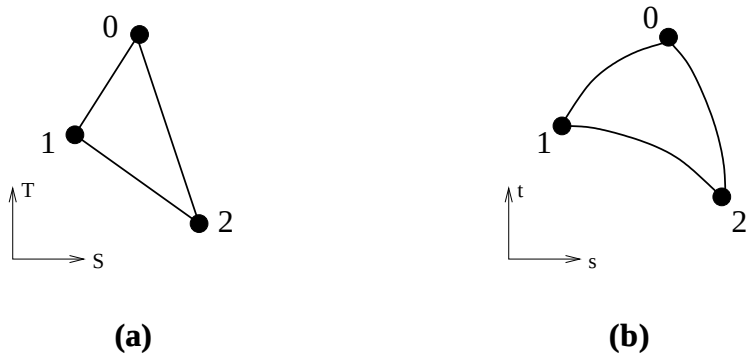

Figure 5.23: (a) A polygon in (S,T) space (b) becomes curved when converted back to (s,t).

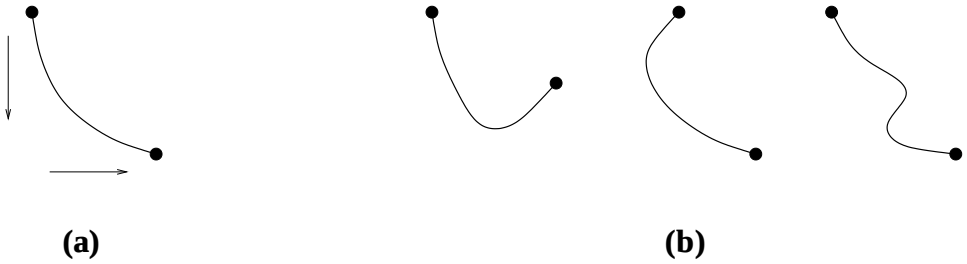

Figure 5.24: (a) The curves bounding the polygon will monotonically increase or decrease in s and t. (b) Curves containing local minima or maxima in s and/or t, such as these, will not occur. We can therefore scan vertically or horizontally from one endpoint to the other and be guaranteed that each scan-line will intersect the curve exactly once.

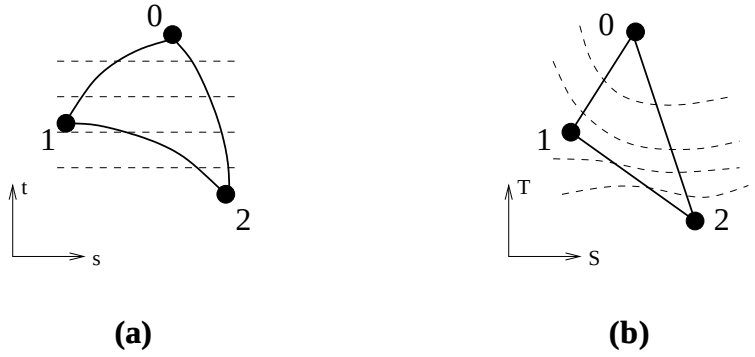

Figure 5.25: (a) We scan across the curved shape for each value of t. (b) Each scan-line becomes a curve in (S,T).

(S, T) space. Then in (s, t) space, the line becomes

$$(s, t;\ Q, Z) = \left(\frac{a_0 S_0 + (1 - a_0) S_1}{a_0 Q_0 + (1 - a_0) Q_1}, \frac{a_0 T_0 + (1 - a_0) T_1}{a_0 Q_0 + (1 - a_0) Q_1}; \right. \\ \left. a_0 Z_0 + (1 - a_0) Z_1, a_0 Q_0 + (1 - a_0) Q_1 \right) \tag{5.7}$$

where a_0 ranges from 0 to 1. This curve is guaranteed to monotonically increase or decrease in both s and t. That is, it will not form any local maxima or minima (Figure 5.24).

This fact allows us to scan convert the transformed triangle in a relatively straightforward fashion. We convert the vertices of the triangle into (s, t) space, determine the maximum and minimum t values, and proceed to iterate over all t within this interval (Figure 5.25). At each one, we find the points of intersection between this slice and the shape's edges. To do this, we must solve for a_0 in Equation (5.7) for the given value of t. This yields

$$a_0 = \frac{tQ_1 - T_1}{(tQ_1 - T_1) - (tQ_0 - T_0)}$$

We use this to find the values of s where the edges cross the slice, as well as to interpolate the depth and other associated values at these points.

Once the endpoints of the slice have been found, we iterate over all s within the slice, comparing the depth at each point with the current value in the depth buffer, and, if necessary, shading these points and entering their values into the color buffer. However, we cannot linearly interpolate the depth values between the two endpoints as we can in the case of an ordinary polygon, because a scan line in (s, t) space corresponds to a curve in (S, T), If we represent a point on the triangle as a weighted sum of the vertices with coefficients a_i, such that $a_0 + a_1 + a_2 = 1$, then the corresponding (s, t) point is given by

$$(s, t, Q, Z) = \left(\frac{\sum a_i S_i}{\sum a_i Q_i}, \frac{\sum a_i T_i}{\sum a_i Q_i}, \sum a_i Z_i, \sum a_i Q_i \right).$$

Inverting this yields

$$a_0 = \frac{a'_0}{a'_0 + a'_1 + a'_2} \qquad a_1 = \frac{a'_1}{a'_0 + a'_1 + a'_2} \qquad a_2 = \frac{a'_2}{a'_0 + a'_1 + a'_2}$$

$$a'_0 = t'_1 s'_2 - t'_2 s'_1 \qquad a'_1 = t'_2 s'_0 - t'_0 s'_2 \qquad a'_2 = t'_0 s'_1 - t'_1 s'_0$$

$$s'_i = S_i - sQ_i$$

$$t'_i = T_i - tQ_i.$$

Using these coefficients, we can interpolate the correct depth for a given (s, t) point, as well as the shading, texture coordinates, and any other desired values. This process makes the inner loop more computationally expensive than in the case of ordinary 2D scan conversion, but not excessively so.

5.8 Results

We implemented our algorithm on an IBM SP2 cluster consisting of 120 and 135 MHz processors, each with between 256 and 2048 MB of RAM. Although in practice we use coarse-grained parallelism to speed the computation, the times given here are for a single 120 MHz processor. For comparison, we also produced software to compute the lumigraph using repeated applications of an ordinary two-dimensional zbuffer. In addition, we implemented a version of our algorithm which scan converts 3-simplices into a three-dimensional buffer. It exploits coherence in the s, U, and V dimensions, but treats each t slice independently, and is suitable for horizontal parallax only holograms. We can expect its performance to be somewhere between that of the 2D and 4D cases.

We tested this software on five models of varying complexity. For each one, we generated lumigraphs with a size of 360×360 samples in (s, t), and either

256×256 or 512×512 in (U, V). Due to memory constraints, it was not possible to generate the entire lumigraph at once. Instead, the (s, t) dimensions were divided into square regions and the 4D zbuffer was applied to each one independently. The size of these regions was varied and the resulting computation times are plotted in the graphs shown in Figures (5.26) through (5.30). The horizontal axis provides the size of each side of the (s, t) regions, so the total number of samples is given by the square of this number. The vertical axis plots the average cost for each (U, V) sub-image of the lumigraph (i.e. a single (s, t) point). We also subdivided (s, t) into linear regions to test the application of the 3D algorithm.

As the graphs show, when applied to a region of size one, our algorithm is considerably more expensive than scan converting in two dimensions. However, as the number of camera points increases, this additional cost is quickly amortized over the entire region. The computation time drops significantly, before eventually leveling off.

The degree of improvement over two-dimensional scan conversion depends primarily on two factors. The most significant is the cost of the shading operation which must be performed for each visible surface point. This computation forms the heart of the innermost loops of the algorithm, and the total time required for it is fixed regardless of whether 2D or 4D scan conversion is used. If this cost is large relative to that of the rest of the computation, few savings will be obtained. On the other hand, if shading can be performed very quickly, then our method becomes much more efficient.

This is most easily observed by comparing Figures (5.26) and (5.27). These show the same scene shaded by two very different methods. The model in Fig-

ure 5.26 was shaded by performing direct lighting computations from 30 lights sources. Precomputed depth maps were used to provide shadowing. Each visible surface was checked against each of the light sources to determine its radiant exitance. No interpolation was used to speed this process. The shading cost was therefore very large relative to that of the rest of the algorithm. As a result, our method performs only slightly better than two-dimensional scan conversion.

The model in Figure 5.27 is a precomputed global illumination solution of the previous model. The shading operation consists simply of interpolating the radiant exitance values found for each of the corners. In this case, the inner loop is very inexpensive, allowing us to achieve an speed increase of over twenty to one, and based on the slope of the curve, an even greater improvement could have been attained had sufficient memory been available to enlarge the size of the region.

The other examples show varying degrees of improvement lying somewhere between these two extremes. It should be noted that our shader software was designed for experimental purposes, with an emphasis on generality rather than efficiency. With a more practical implementation , we should see speed increases for most scenes that are significantly higher than the 20:1 ratio of Figure 5.27.

The second limitation on the speed of our algorithm is the amount and speed of the memory available to us. We have already mentioned that without enough memory, it is not possible to process the entire lumigraph at once, forcing us to break it up into smaller sections. This limits the extent to which we can take advantage of coherence in the (s, t) dimensions. In addition, the nature of the scan conversion process requires us to access memory in a rather incoherent fashion as we sample points throughout the array for each polygon scanned.

This causes a great deal of memory page swapping, which can slow down the computation. As a result, the time plots in the figures level off at a higher point than they would if memory access were not a concern, and some even begin to increase as the memory becomes completely full.

Therefore, in order to take full advantage of our algorithm, we require a very large amount of fast random access memory. While this requirement is still somewhat beyond the limits of current technology, it is not unreasonable. Recall that our goal is to provide an algorithm which can drive an electronic holographic display system, and that, as large as the lumigraph is, a hologram is even larger. A frame buffer for such a display would need even more memory than we have described. Therefore, it is safe to assume that by the time a holographic display becomes commercially available, the memory which we need to efficiently implement our rendering algorithm will be available as well.

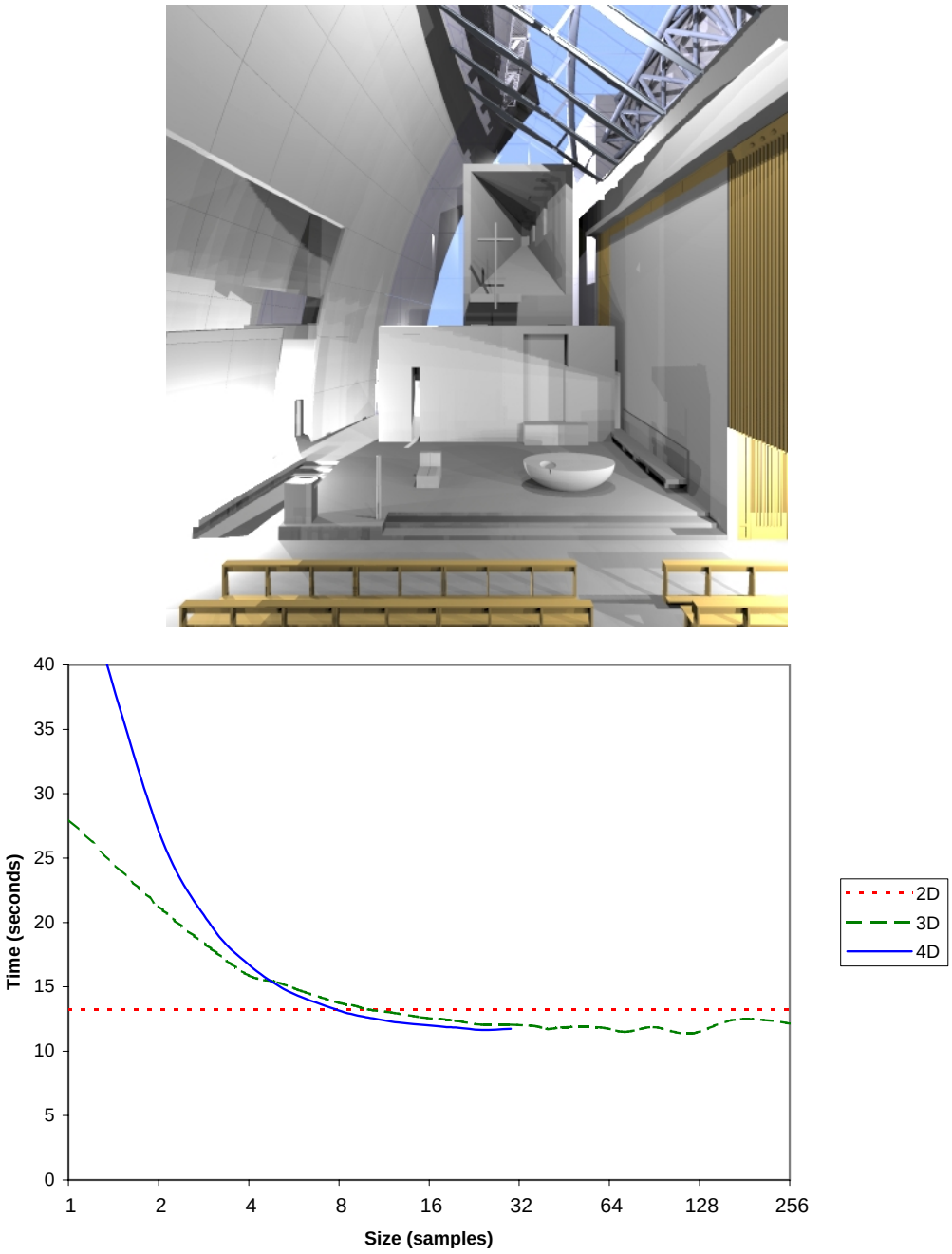

Figure 5.26: A church model consisting of 93,459 triangles and 30 light sources. Shading is computed using direct illumination from each of the light sources. Precomputed depth maps provide shadowing. Because of the high cost of the shading operation, our algorithm provides only a marginal improvement. (model by Richard Meier Associates)

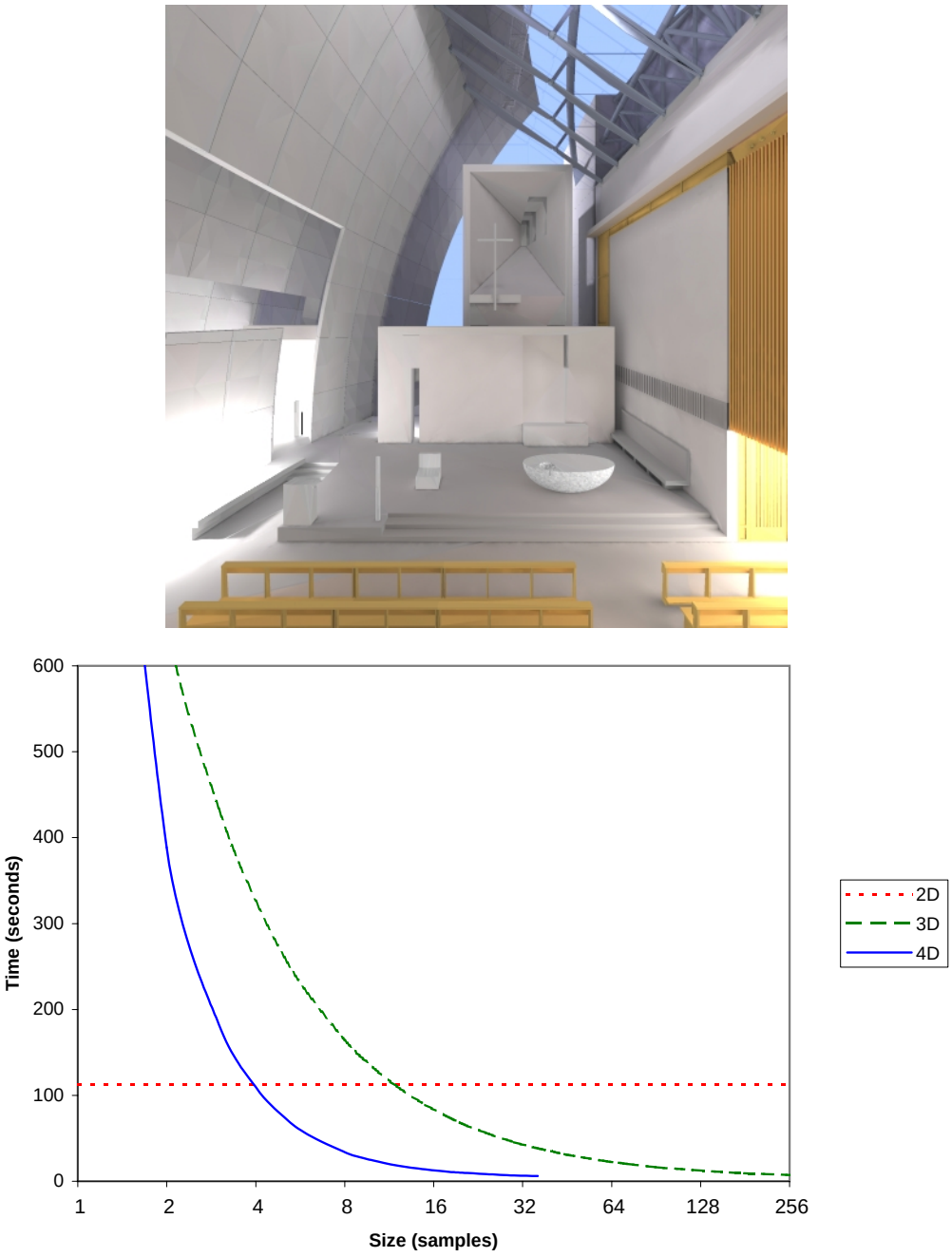

Figure 5.27: A global illumination solution of the same scene as in the previous figure, consisting of 3,320,101 triangles with radiant exitance information stored for each vertex. Shading is performed by interpolating between the vertex values. Because of the relatively low cost of this operation, a speedup of over 20:1 is gained. The computation time is still dropping at the point at which we run out of memory, indicating that with larger regions, even more improvement can be gained.

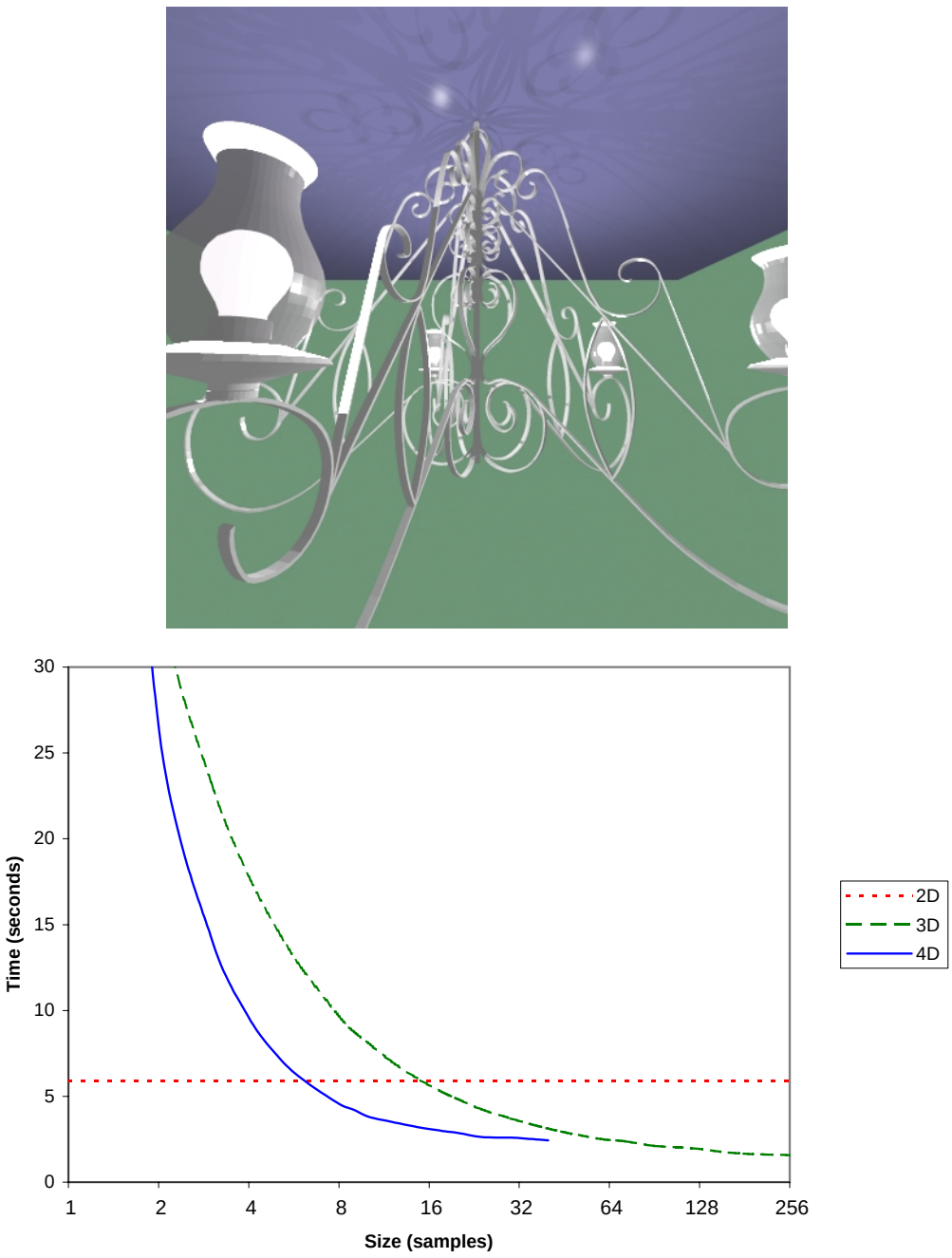

Figure 5.28: A chandelier consisting of 113,338 triangles and 5 light sources. Shading is performed as in Figure 5.26. (model by Luis Filipe)

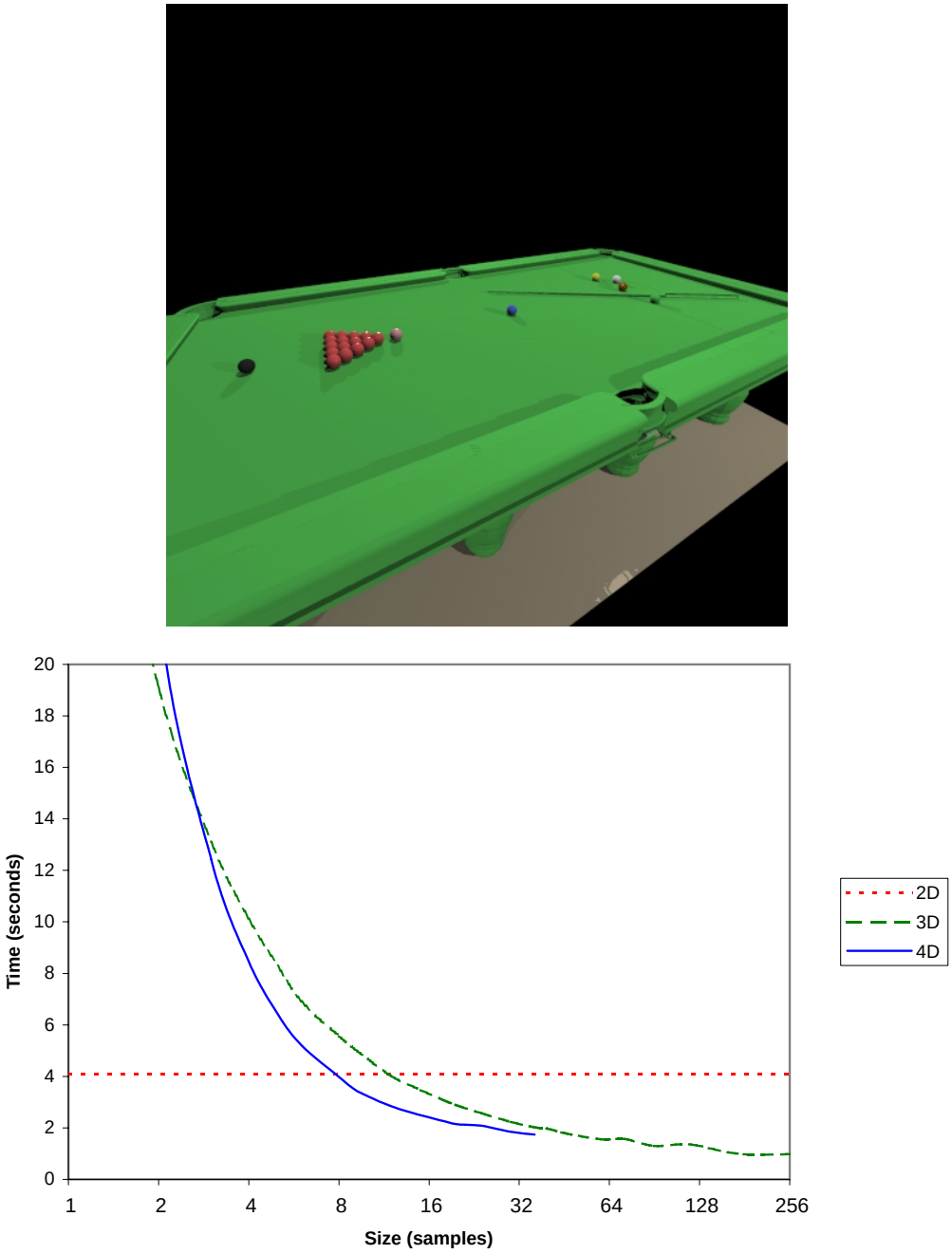

Figure 5.29: A pool table consisting of 64,444 triangles with 4 light sources. Shading is computed for each vertex of the triangles and then interpolated across their faces, where they are then modulated by shadow depth maps. (model by Barry Driessen)

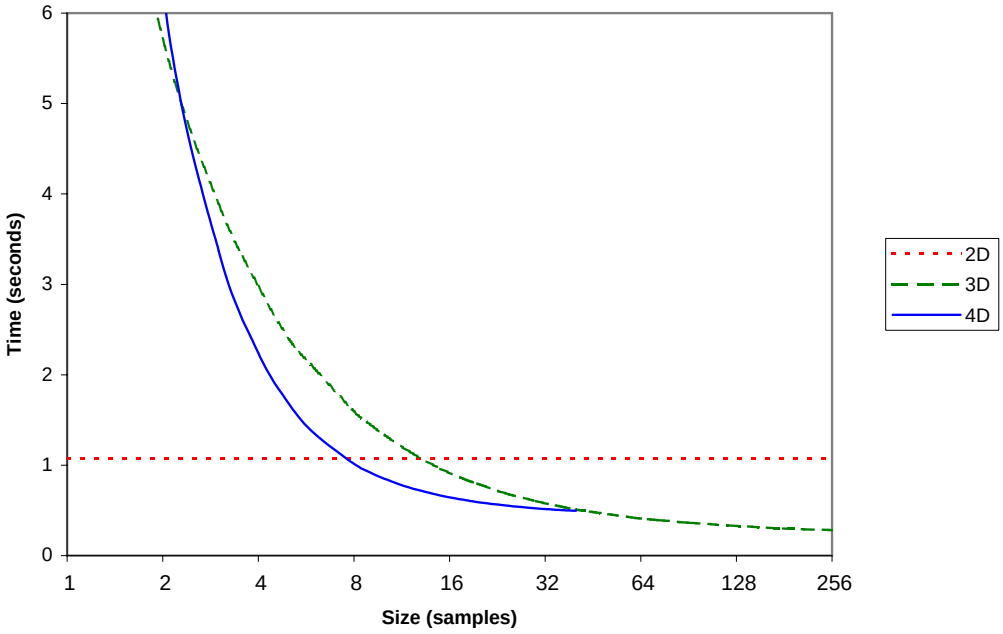

Figure 5.30: A jack-o-lantern consisting of 16,318 triangles and 2 light sources. Shading is computed at the vertices and interpolated across the triangles. (model by Dave Edwards)

Chapter 6

Holographic Image Preview

As previously stated, electronic holographic displays capable of generating full parallax images do not yet exist. Even horizontal parallax displays are available only as experimental prototypes. Several methods for producing hardcopy output of holographic interference patterns exist, but these are too slow, and often too expensive as well, to be used interactively, making them suitable only for the display of final results. In the absence of an output device capable of providing feedback within a reasonable time frame, how can we debug holographic rendering algorithms or preview holographic images?

To solve this problem, we have developed a simple camera emulator to determine what an observer looking at the hologram from various positions will see. Unlike the traditional camera models based on geometric optics which are normally associated with rendering applications, our model uses wave optics in order to capture the three-dimensional effect produced by the interference pattern. We utilize Fourier techniques to simulate the propagation of wavefronts from the hologram, through a camera lens, and onto a film plane. An overview of our camera model and the different steps in the simulation process is shown

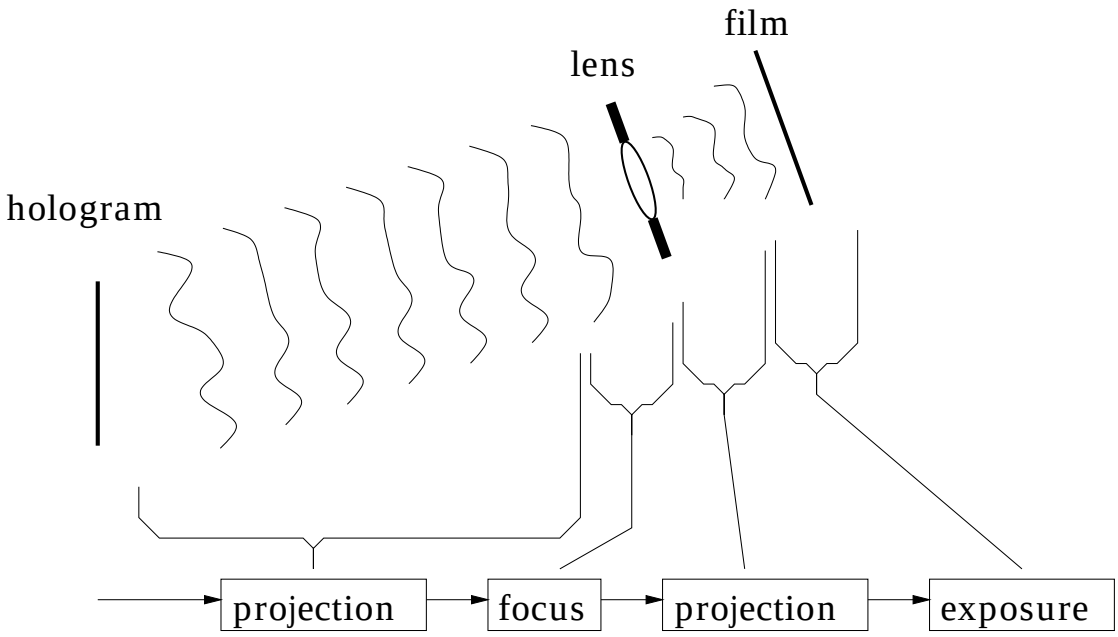

Figure 6.1: Basic overview of our camera model. Light from the hologram is projected onto the lens plane. There, it is adjusted to provide the desired degree of focus. It is then projected onto the film plane, where we obtain an image.

in Figure 6.1. In the following sections, we will describe these steps in more detail.

6.1 Projection

In Section 3.4 we discussed several methods for computing a hologram based on the Fourier transform. Various drawbacks of these algorithms made them unsuitable for the generation of realistic holograms of complex scenes. However, they adapt quite well to the more limited task of generating an image of a hologram that has already been computed. We will now take a closer look at one such method, developed independently by both Leseberg [69] and Tommasi and Bianco [113, 114].

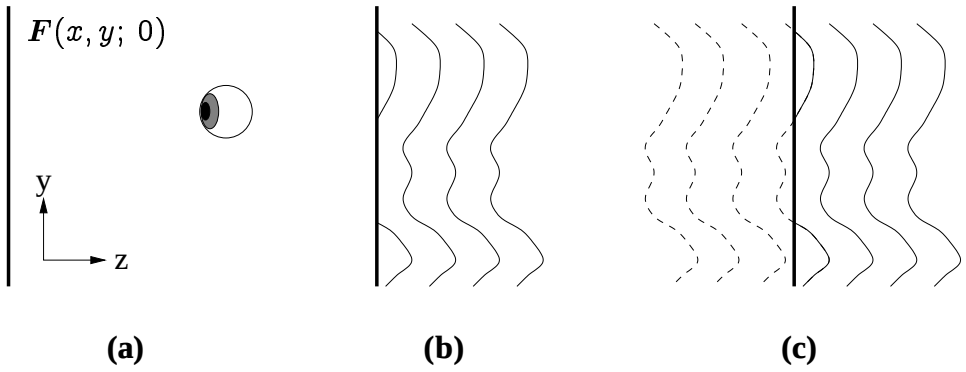

Figure 6.2: (a) A hologram with known emission is situated in the x-y plane and viewed from the positive z region. (b) The field in this region can be derived from the field at the hologram plane. (c) Working backwards, we can also derive a virtual field in the negative z region.

Suppose that we have a hologram lying in the x-y plane, as shown in Figure 6.2(a). We assume that this hologram was created by some unspecified computational process, and that the light $\boldsymbol{F}(x, y;\ 0)$ across it is known. We further assume that the hologram is meant to be observed from the positive z region, and that it emits light only on this side. This gives rise to a field $\boldsymbol{F}(x, y, z > 0)$ throughout this half-space (Figure 6.2(b)). We can extrapolate this to obtain a virtual field in the negative z half-space by treating the light as the result of a wavefront emanating from $z = -\infty$ by backtracking from the hologram plane. (Figure 6.2(c)). Our goal is to find this $\boldsymbol{F}(\vec{x})$ at an arbitrary plane.

6.1.1 Translation

We begin by determining the light at a plane parallel to the hologram (Figure 6.3). Let us define $\boldsymbol{f}(\vec{k})$ to be the frequency space representation of $\boldsymbol{F}$ as given by the Fourier transform:

$$\boldsymbol{f}(\vec{k}) = \mathcal{F}_{\vec{x}}\left\{\boldsymbol{F}(\vec{x})\right\}\left(\vec{k}\right) = \iiint \boldsymbol{F}(\vec{x}) e^{i(\vec{k}\cdot\vec{x})} dx dy dz. \tag{6.1}$$

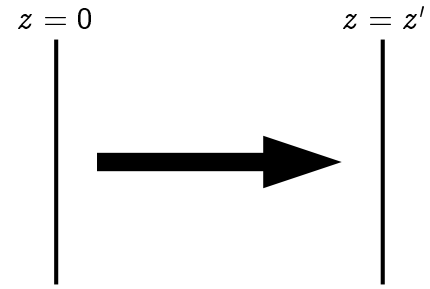

Figure 6.3: Projecting light from the hologram to the $z = z'$ plane.

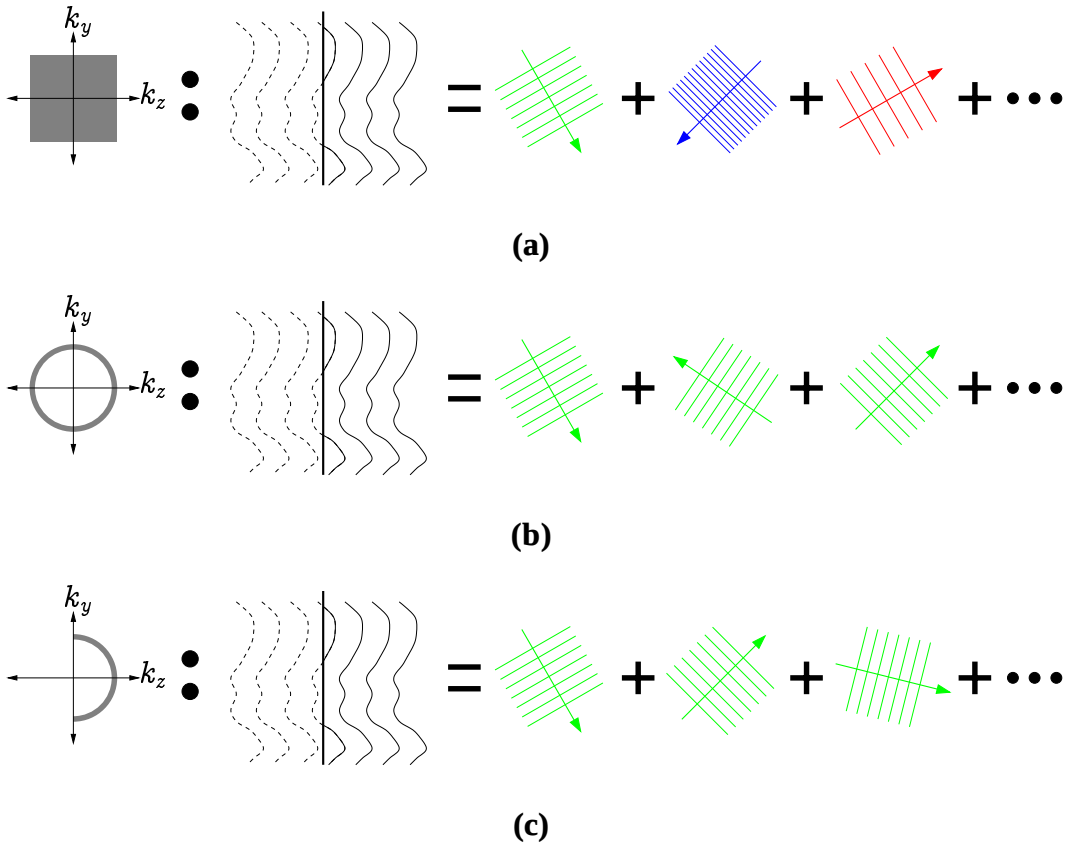

Figure 6.4: (a) The Fourier transform allows us to represent the field as an infinite sum of plane waves. (b) Using monochromatic light, we are restricted to a spherical shell in frequency space. (c) Eliminating light not towards the viewer further restricts us to a hemispherical shell. This can now be represented by a single two-dimensional function.

Inverting this yields

$$\boldsymbol{F}(\vec{x}) = \mathcal{F}_{\vec{k}}^{-1}\left\{\boldsymbol{f}(\vec{k})\right\}(\vec{x}) = \iiint \boldsymbol{f}(\vec{k}) e^{-i(\vec{k}\cdot\vec{x})} dk_x dk_y dk_z. \tag{6.2}$$

For a fixed $\vec{k}$, the expression $e^{-i(\vec{k}\cdot\vec{x})}$ describes a plane wave of wavelength $\frac{2\pi}{k}$ traveling in the $\hat{k}$ direction. Thus Equation (6.2) tells us that $\boldsymbol{F}$ can be treated as a weighted sum of an infinite set of plane waves (Figure 6.4(a)).

If we limit the hologram to monochromatic light of a given wavelength λ, we eliminate all the plane waves except those for which $\|\vec{k}\| = \frac{2\pi}{\lambda}$. This causes $\boldsymbol{f}$ to become zero except over a spherical shell of radius $\frac{2\pi}{\lambda}$ centered at the origin (Figure 6.4(b)). It can now be mapped to a pair of two-dimensional functions, $\boldsymbol{f}_+(k_x, k_y)$ and $\boldsymbol{f}_-(k_x, k_y)$, which represent the light emitted over the positive z and negative z directional hemispheres, respectively. We have

$$\boldsymbol{f}(\vec{k}) = \boldsymbol{f}_+(k_x, k_y)\delta(k_z - k_z') + \boldsymbol{f}_-(k_x, k_y)\delta(k_z + k_z'), \tag{6.3}$$

where $k_z' \equiv \sqrt{\left(\frac{2\pi}{\lambda}\right)^2 - k_x^2 - k_y^2}$.

The fact that the hologram only emits on the positive z side lets us set $\boldsymbol{f}_-(k_x, k_y) = 0$, yielding

$$\boldsymbol{f}(\vec{k}) = \boldsymbol{f}_+(k_x, k_y)\delta(k_z - k_z'). \tag{6.4}$$

The three-dimensional frequency decomposition now maps to a two-dimensional function (Figure 6.4(c)).

Combining Equation (6.2) and Equation (6.4) and selecting a fixed $z = z'$ yields

$$\boldsymbol{F}(x, y;\ z') = \iint \boldsymbol{f}_+(k_x, k_y) e^{-ik_z' z'} e^{-i(k_x x + k_y y)} dk_x dk_y \tag{6.5}$$

$$= \mathcal{F}_{(k_x,k_y)}^{-1}\left\{\boldsymbol{f}_+(k_x, k_y) e^{-ik_z' z'}\right\}(x, y). \tag{6.6}$$

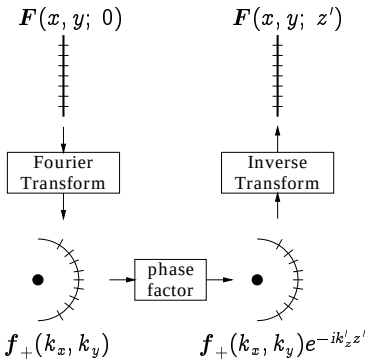

Figure 6.5: Schematic representation of the process of projecting light from one plane to another parallel plane.

Inverting this gives us

$$f_+(k_x, k_y) = e^{+ik'_z z'} \mathcal{F}_{(x,y)} \{F(x, y; z')\} (k_x, k_y), \tag{6.7}$$

which, when applied to the known field at the hologram plane, $z' = 0$, becomes

$$f_+(k_x, k_y) = \mathcal{F}_{(x,y)} \{F(x, y; 0)\} (k_x, k_y). \tag{6.8}$$

Thus, we can use Equation (6.8) to find f_+ from the computed hologram, and then apply Equation (6.6) to determine the light at any plane parallel to the hologram This process is shown in Figure 6.5.

6.1.2 Rotation

Now suppose that we wish to find the field at a plane which is not parallel to the hologram (Figure 6.6(a)). For any such plane, we can always find a new frame of reference in which it is perpendicular to the z axis at some distance z' from the origin and in which the hologram intersects the origin (Figure 6.6(b)). This new reference frame is separated by the original one by some rotation $\mathcal{R}$.

Let us apply Equation (6.8) in the original frame of reference to obtain f_+. Recall that this two-dimensional function maps to the directional hemisphere in

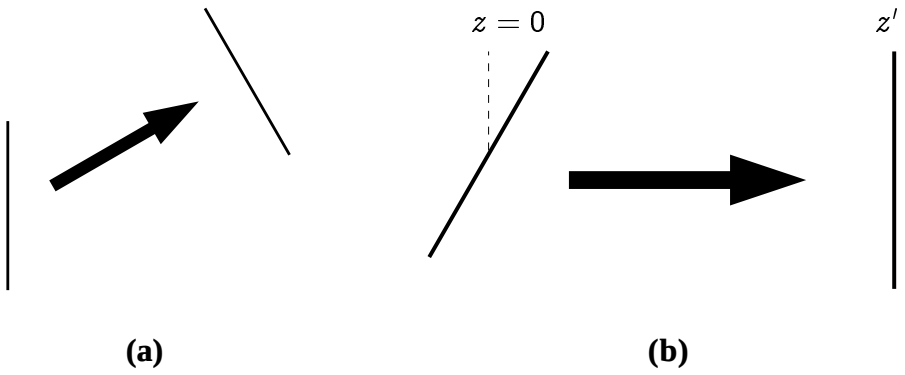

Figure 6.6: (a) Projecting light from the hologram to an arbitrary plane. (b) By choosing an appropriate coordinate transformation, the hologram becomes rotated and the target plane lies perpendicular to the z axis.

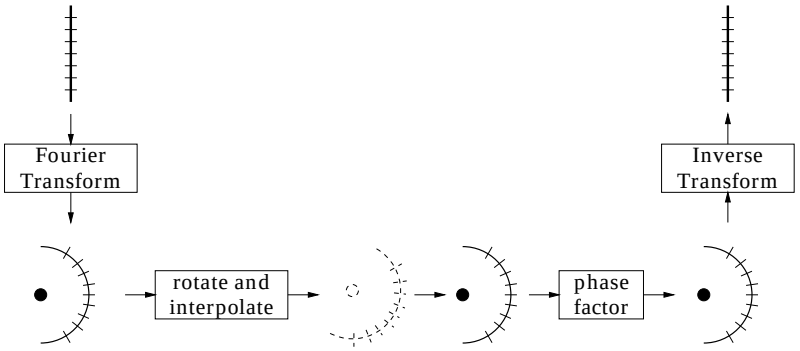

Figure 6.7: Adding rotation to the process of Figure 6.5.

frequency space. To obtain f_+ in the new frame of reference, we need simply rotate this hemisphere. In discrete form, this means that we interpolate the originally computed function to a new sampling grid (Figure 6.7). Once we know f_+ in the new frame, we can proceed as before to project it onto the destination plane with Equation (6.6).

6.1.3 Direction restriction

Recall that the use of the fast Fourier transform for holography results in unwanted duplicate images tiling the plane. These duplicates can interfere with

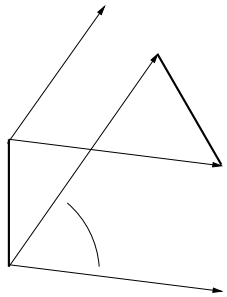

Figure 6.8: The limits of ray directions between the two planes.

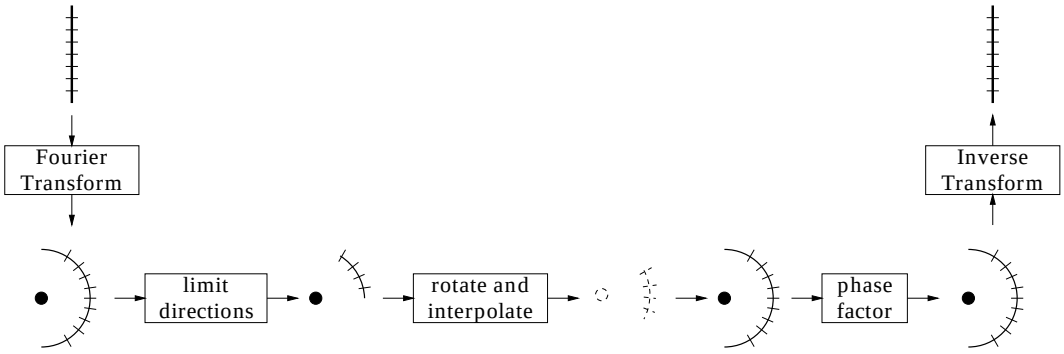

Figure 6.9: The complete projection process

pictures taken by our simulated camera. Although they cannot be eliminated completely, we take some additional steps which greatly reduce them. By examining the boundaries of the hologram and destination planes, we can obtain limits on the set of all ray directions between points on the two planes (Figure 6.8). After applying the Fourier transform, we set all frequency components corresponding to directions outside these limits to zero (Figure 6.9). This will prevent the light from most of the replicated images from being able to pass through the lens of our virtual camera.

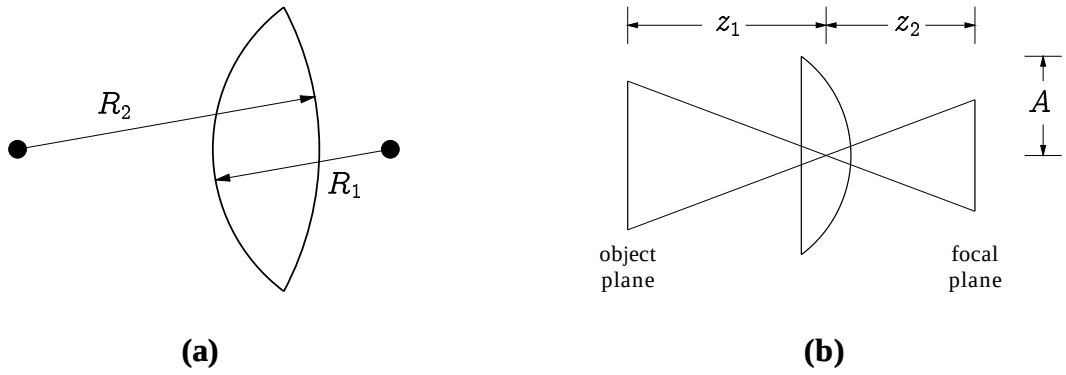

Figure 6.10: (a) General thin lens. (b) Focusing in a planar-convex lens.

6.2 Focus

We now have the means to project the light emitted by the hologram to a lens plane, and from there to a film plane. To complete our camera model, we need to simulate the focusing operation performed by the lens. Since we are using wave rather than geometric optics, we do not model this as a bending of the light. Instead, we treat the lens as an infinitesimally thin surface which modulates the magnitude and/or the phase of the complex wavefront.

There are a number of types of lenses we could choose to emulate here, which give rise to similar modulation functions. Zone plates are planar lenses which affect the magnitude of light passing through them. Fresnel lenses can be modeled as planar lenses which modulate phase. For our purposes, we choose a phase modulation derived from the thin lens equation.

Given a lens with spherical faces of radius R_1 and R_2, as shown in Figure 6.10(a), and index of refraction n, if it sufficiently thin, it can be approximated as having a focal length l given by

$$\frac{1}{l} = (n-1)\left(\frac{1}{R_1} + \frac{1}{R_2}\right). \tag{6.9}$$

If we wish to focus an object at distance z_1 onto a film plane at distance z_2 with

a planar-convex lens ($R_1 = \infty$), we require $R_2 = l(n-1)$, where $\frac{1}{l} = \frac{1}{z_1} + \frac{1}{z_2}$ (Figure 6.10(b)). If the lens has a total aperture of radius A, then its thickness at a distance a from the center is

$$\tau(a) = \sqrt{R_2^2 - a^2} - \sqrt{R_2^2 - A^2} = \sqrt{(l(n-1))^2 - a^2} - \sqrt{(l(n-1))^2 - A^2}. \tag{6.10}$$

Since we are not limited to real materials, we can make the index of refraction become infinitely large. This has two effects. First, the thickness can be approximated as

$$\tau(a) \approx \frac{A^2 - a^2}{2l(n-1)}. \tag{6.11}$$

Second, any light ray striking the planar side of the lens will be refracted so as to travel almost perpendicular to this plane. Combining these two facts, we see that light striking the plane will travel a distance $\tau(a)$ through the lens determined solely by the position at which it strikes the lens, and not by its incoming direction.

Light entering a medium with index of refraction n is slowed by a factor of $\frac{1}{n}$. After traveling a distance τ through such a medium, it will lag $(n-1)\frac{\tau}{\lambda}$ cycles behind light traveling the same distance through empty space. Thus, as n becomes infinite, the lens becomes an infinitesimally thin surface which introduces a phase delay of

$$e^{-i2\pi\frac{A^2-a^2}{2l\lambda}}. \tag{6.12}$$

By applying this phase shift to the light projected onto the lens plane, we can achieve the desired focusing effect.

6.3 Exposure

Finally, we must simulate the exposure of the film to produce an image. This step is trivially easy. Based on the camera geometry and the relative distances between the lens plane and the hologram and film planes, we determine the portion of the film plane onto which the image of the hologram will project. We determine the light intensities within this region by squaring the computed field magnitudes. The sample spacing will be on the order of the wavelength of light, so we downsample by simple averaging to obtain an image of a reasonable size.

6.4 Results

We tested our camera by computing several views of a hologram of Cornell's McGraw bell tower (Figure 6.11). Once again, the amount of memory available proved to be a major limiting factor. In order to efficiently compute the required FFTs, it is necessary to have the entire hologram in memory. This places a bound on how large a hologram we can use. We can alleviate this problem to some extent by running the program in parallel on multiple systems, with each one taking responsibility for a portion of the data. However, given the resources available to us, we were still only able to operate on holograms up to about 8 millimeters in size. Note that this limitation only affects our ability to use the camera simulator. With the algorithm of the previous chapter, we are able to generate significantly larger holograms.

The reason this concerns us is that the size of the hologram limits the size of the camera aperture. If the aperture is too large, then their will be strong depth of field effects, and much of the scene will appear blurry. If the aperture is too

Figure 6.11: A model of Cornell's McGraw bell tower.

small, then diffractive effects will become apparent, making the image noisy. Ideally, the computed hologram should be made as large as possible, allowing the aperture to be big enough to eliminate noise, while still remaining relatively small compared to the hologram, allowing good focus.

Figure 6.12 shows three views of our test hologram from different camera angles. The hologram was 7 mm across, and the aperture used had a diameter of 1 mm. Both the blurring and noise described above are apparent. Nevertheless, the images are of sufficient quality to serve their purpose, confirming that the hologram was rendered correctly and providing a preview of how it will appear. As a result, this simulator proved to be invaluable during the development of the algorithms discussed in the previous chapters.

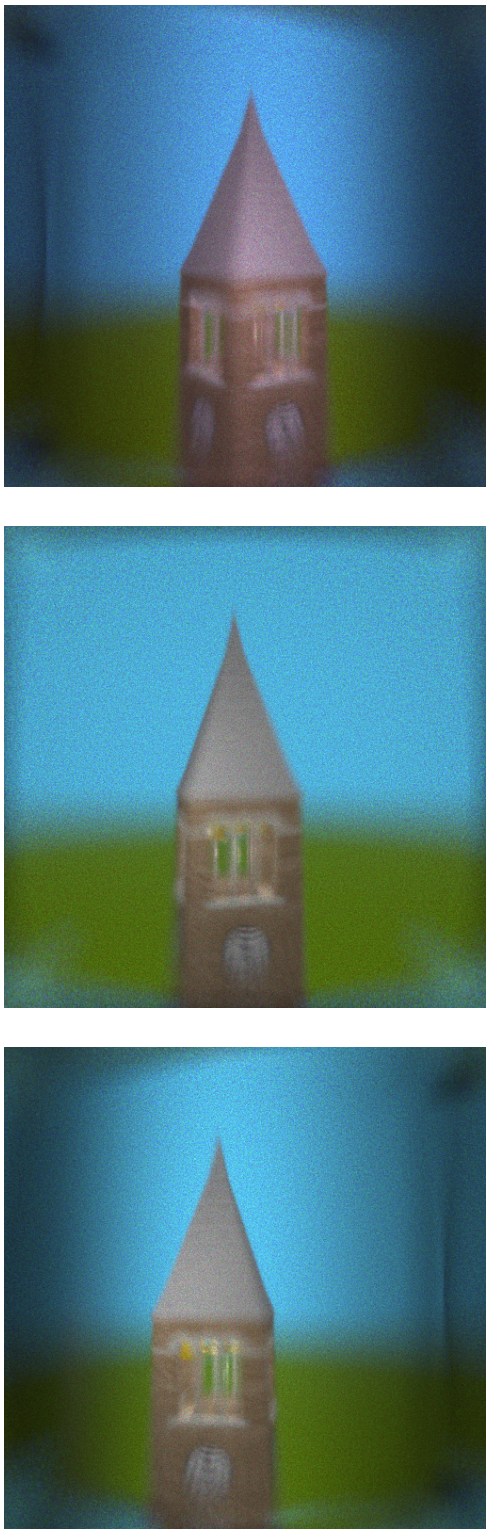

Figure 6.12: Three views of the same hologram taken from different positions using our camera simulator.

Chapter 7

Conclusions

7.1 Summary

We have presented several tools to advance the field of computer generated holographic stereograms.

First, we addressed the issue of compressing the enormous amount of data required to represent the hologram down to a manageable size for transmission and storage. We described how the JPEG compression standard can be extended to handle the compression of lumigraphs. We also described the use of wavelet transforms for this purpose and provide a means for encoding the transformed data which yields compression roughly equivalent to that of the existing EZW algorithm but in much less time. After comparing a number of wavelets, as well as the JPEG scheme, we found the (3,3) average interpolating wavelet to provide the best results.

Next, we described an algorithm for efficiently rendering the lumigraph. We convert the scene geometry into a set of simple four-dimensional primitives, and scan convert them into a set of 4D color and depth buffers. By taking ad-

vantage of coherence in all four dimensions, this method can yield tremendous savings in computation time. Additionally, its structure is designed so as to allow it to be implemented in hardware and serve as the basis for a real-time holographic display system.

Finally, we presented a camera simulator to allow computed holograms to be previewed in the absence of a real-time display. Using wave optics, we compute the propagation of light from the hologram, through a lens, and onto the film plane. The resulting images, while exhibiting some artifacts, allow us to assess the correctness of our holographic rendering software.

7.2 Comments and Future Work

7.2.1 Compression

Using the best of the compression methods examined, we can obtain lumigraphs with only marginally perceptible error at a compression of about 2 pixels per bit in grayscale, or 0.67 ppb for color. At first glance, this seems rather disappointing. JPEG compression of 2D color images can typically achieve compression of at least 1 ppb without significant error, and we expect better performance for a lumigraph. Several factors account for this discrepancy.

The first is that, as we discussed, memory constraints forced us to apply the transforms to only three of the four dimensions of the lumigraph. We can expect that with sufficient memory to transform in all four dimensions, we will obtain higher compression.

The second factor is the difference in how our algorithm makes use of color. Most JPEG implementations convert the image to XYZ, HSV, or some other per-

ceptual color space before applying the DCT. Since errors in color are significantly less noticeable than errors in luminance, the two channels governing the color can be compressed to a much higher degree. Only a disproportionally small percentage of JPEG's compression comes from the luminance channel.

On the other hand, we chose to leave the data in RGB space and compress each channel equally. This decision was made so as to allow the computation of the interference pattern by weighted sums, as in Equation (3.24). This form of conversion is not compatible with any color representation other than separate channels for each wavelength. However, for those situations where conversion will be performed by FFT, we believe it would be well worth exploring how much improvement could be gained by the use of an alternative color space.

The third reason for the apparent shortcoming of our algorithm is the difference in dynamic range. JPEG is normally applied to 8-bit images. Recall, however, that we chose to use lumigraphs with full floating point precision. The scenes on which our algorithm was tested had ranges on the order of 100,000 to 1. Thus, although the number of pixels per bit that we produce is lower than that of JPEG, the effective compression ratio is larger. Nevertheless, we feel that there is potential here for more significant gains.

Our decision to use floating point values was motivated by a desire to take advantage of the high dynamic range afforded by a holographic display. However, we may be preserving more information than is necessary, at the cost of potential compression. Several recent papers on tone reproduction have described methods for collapsing an image with a large dynamic range into a limited number of bits, while preserving important visual content. We believe that by applying such a scheme before the wavelet transform, we should be able

to greatly increase the degree of compression without introducing additional perceptual errors.

Obviously, this is, in general, contrary to our intent to maintain the original lumigraph's high dynamic range. However, one tone reproduction algorithm in particular, the histogram adjustment method of Larson et.al. [59], not only produces high quality results, but possesses the added benefit of being easily invertible. Thus, after decompression, we can reverse the process to obtain the original luminance values. Additionally, we are not hampered by the normal motivation of tone reproduction, where we are mapping to some fixed number of bits determined by a particular display device. Instead we can choose an optimal number of bits for a given lumigraph so as to provide the maximum possible compression while avoiding the loss of detail which often is an inevitable byproduct of such algorithms.

7.2.2 Rendering

We chose to use simplices as the fundamental primitive for our renderer because their simple structure makes them very easy to represent and manipulate, especially for a hardware implementation. However, the repeated slicing and subdivision used by our algorithm to perform clipping can result in the creation of a very large number of very small simplices, reducing the efficiency. In the theoretical worst case scenario, a single scene triangle can generate over 40,000 simplices, although this is a pathological case, and in practice we never observed anything remotely approaching this order of magnitude.

One possible approach to help alleviate this problem is to borrow another concept used by 2D rendering: the triangle strip. This consists of an ordered list

of triangles, each of which shares two vertices with the one preceding it. A triangle strip requires one third the amount of data as a set of independent triangles, and many redundant computations can be eliminated by taking advantage of their connectivity.

We can extend this to four dimensions by creating simplex strips, each member of which shares four of its five vertices with the simplex preceding it. The initial simplex queue created for a polygon can always be sorted into one or two such strips. Whenever clipping of one or more simplices in a strip results in a new set of simplices being created, they can be inserted into the strip, sometimes causing it to be split into two new strips. In this way, it should be possible to perform clipping and scan conversion on an entire strip at once, thereby reducing the computational cost.

Another possible approach is to use a combination of simplices and simploids as the lowest level primitives. Like simplices, simploids also have a structure which can be easily represented and operated on. For many of the intermediate simploids generated by our algorithm, subdivision may not be necessary to the performance of scan conversion. Choosing to perform this operation on a simploid will undoubtedly be more complex than it would be on a simplex, but should still provide savings over subdividing and operating on several simplices.

7.3 Final Thoughts

Two-dimensional images are something of which we have a very strong understanding, as well as a great deal of experience at computing. It is therefore very

tempting to view a lumigraph simply as a collection of images, and to treat the problem of computing it as a series of independent 2D renderings. However, in so doing, we throw away a tremendous amount of coherence which can be used to our advantage. We hope we have shown here that only by moving beyond two dimensions and visualizing the lumigraph as the four-dimensional structure that it is, can we begin to produce algorithms capable of rendering lumigraphs at the rate needed to drive a real-time holographic display.

Bibliography

[1] Robert Akka. Utilizing 6D head-tracking data for stereoscopic computer graphics perspective transformations. In *Stereoscopic Displays and Applications IV (Proceedings of SPIE)*, volume 1915, pages 147–154, 1993.

[2] Marc Antonini, Michel Barlaud, Pierre Mathieu, and Ingrid Daubechies. Image coding using the wavelet transform. *IEEE Transactions on Image Processing*, 1(2):205–220, April 1992.

[3] Stephen A. Benton. Hologram reconstructions with extended incoherent sources. *Journal of the Optical Society of America*, 59:1545–1546A, 1969.

[4] Stephen A. Benton. Holographic displays - a review. *Optical Engineering*, 14(5):402–407, Sep–Oct 1975.

[5] Stephen A. Benton. Holographic displays: 1975–1980. *Optical Engineering*, 19(5):686–690, Sep–Oct 1980.

[6] Stephen A. Benton. Display holography: An SPIE critical review of technology. In *Holography (Proceedings of SPIE)*, volume 532, pages 8–13, 1985.

[7] Stephen A. Benton, editor. *Practical Holography IV (Proceedings of SPIE)*, volume 1212, 1990.

[8] Stephen A. Benton. Elements of holographic video imaging. In *International Symposium on Display Holography (Proceedings of SPIE)*, volume 1600, pages 82–95, 1991.

[9] Stephen A. Benton, editor. *Practical Holography V (Proceedings of SPIE)*, volume 1461, 1991.

[10] Stephen A. Benton, editor. *Practical Holography VI (Proceedings of SPIE)*, volume 1667, 1992.

[11] Stephen A. Benton, editor. *Practical Holography VII: Imaging and Materials (Proceedings of SPIE)*, volume 1914, 1993.

[12] Stephen A. Benton. Edwin Land, 3-D, and holography. *Optics and Photonics News*, 5(10):41–43, October 1994.

[13] Stephen A. Benton, editor. *Practical Holography VIII (Proceedings of SPIE)*, volume 2176, 1994.

[14] Stephen A. Benton, editor. *Practical Holography IX (Proceedings of SPIE)*, volume 2406, 1995.

[15] D. J. De Bitetto. Bandwidth reduction of hologram transmission system by elimination of vertical parallax. *Applied Physics Letters*, 12(5):176–178, March 1968.

[16] Jim Blinn. *Jim Blinn's Corner: A Trip Down the Graphics Pipeline*. Morgan Kaufmann Publishers, Los Altos, CA 94022, USA, 1996. This book is a collection of columns from the journal IEEE Computer Graphics and Applications.

[17] Duane K. Boman. International survey: Virtual-environment research. *Computer*, 28(6):57–65, June 1995.

[18] Reinhard Börner. Progress in projection of parallax-panoramagrams onto wide-angle lenticual screens. In *True 3D Imaging Techniques and Display Technologies (Proceedings of SPIE)*, volume 761, pages 35–43, 1987.

[19] E. Oran Brigham. *The Fast Fourier Transform*. Prentice-Hall, Englewood Cliffs, NJ, 1974.

[20] E. Oran Brigham. *The Fast Fourier Transform and Its Applications*. Prentice-Hall, Englewood Cliffs, NJ, 1988.

[21] B. R. Brown and A. W. Lohmann. Complex spatial filtering with binary masks. *Applied Optics*, 5(6):967–969, June 1966.

[22] Byron Brown. Improved computer-generated binary holograms. *Journal of the Optical Society of America*, 58:729A, 1968.

[23] C. B. Burckhardt. A simplification of lee's method of generating holograms by computer. *Applied Optics*, 9(8):1949, August 1970.

[24] O. Bryngdahl Ch. Frère, D. Leseberg. Computer-generated holograms of three-dimensional objects composed of line segments. *Journal of the Optical Society of America A*, 3(5):726–730, May 1986.

[25] Hsuan Chen and F. T. S. Yu. One-step rainbow hologram. *Optics Letters*, 2(4):85–87, April 1978.

[26] Chromatek Inc. Product literature. 11450-F North Fulton Industrial Blvd, Alpharetta, GA 30201-4703.

[27] D. C. Chu. Recent approaches to computer-generated holograms. *Optical Engineering*, 13(3):189–195, May / June 1974.

[28] C. K. Chui. *An Introduction to Wavelets*. Academic Press, San Diego, 1992.

[29] C. K. Chui, editor. *Wavelets: A Tutorial in Theory and Applications*. Academic Press, San Diego, 1992.

[30] T. E. Clifton III and Fred L. Wefer. Direct volume display devices. *IEEE Computer Graphics and Applications*, pages 57–65, July 1993.

[31] Patrick C. Coffield. An architecture for processing image algebra operations. In *Image Algebra and Morphological Image Processing III (Proceedings of SPIE)*, volume 1769, pages 178–189, 1992.

[32] A. Cohen, Ingrid Daubechies, and J.-C. Feauveau. Biorthogonal bases of compactly supported wavelets. *Communications on Pure and Applied Mathematics*, 45:485–560, 1992.

[33] James W. Cooley and John W. Tukey. An algorithm for the machine calculation of complex fourier series. *Mathematical Computation*, 19:297–301, 1965.

[34] W. J. Dallas. *Computer-Generated Holograms*, pages 291–366. Springer-Verlag, New York, 1980.

[35] Ingrid Daubechies. Orthonormal bases of compactly supported wavelets. *Communications on Pure and Applied Mathematics*, 41:909–996, November 1988.

[36] Ingrid Daubechies. *Ten Lectures on Wavelets*. Number 61 in CBMS-NSF Series in Applied Mathematics. SIAM, Philadelphia, 1992.

[37] Gilles Deslauriers and Serge Dubuc. Symmetric iterative interpolation processes. *Constructive Approximation*, 4:49–68, 1989.

[38] David L. Donoho. *Smooth Wavelet Decompositions with Blocky Coefficient Kernels*. Academic Press, Inc., 1993.

[39] Jesse Eichenlaub. A novel low cost 2D / 3D autostereoscopic system for notebook computers and other portable devices. In *Stereoscopic Displays and Virtual Reality Systems II (Proceedings of SPIE)*, volume 2409, pages 113–117, 1995.

[40] Jesse Eichenlaub, Dan Hollands, and Jamie Hutchins. A prototype flat panel hologram-like display that produces multiple perspective views at full resolution. In *Stereoscopic Displays and Virtual Reality Systems II (Proceedings of SPIE)*, volume 2409, pages 102–112, 1995.

[41] David Ezra, Graham J. Woodgate, Basil A. Omar, Nicolas S. Holliman, Jonathan Harold, and Larry S. Shapiro. New autostereoscopic display system. In *Stereoscopic Displays and Virtual Reality Systems II (Proceedings of SPIE)*, volume 2409, pages 31–40, 1995.

[42] D. Gabor. A new microscopic principle. *Nature*, 161:777–8, 1948.

[43] D. Gabor. Microscopy by reconstructed wave fronts: II. *Proceedings of the Physical Society B*, 64(6):449–469, 1951.

[44] D. Gabor and Dr.-Ing. Microscopy by reconstructed wave-fronts. *Proceedings of the Royal Society A*, 197:454–487, 1949.

[45] Joseph W. Goodman. *Introduction to Fourier Optics*. McGraw-Hill, San Francisco, 1968.

[46] Steven J. Gortler, Radek Grzeszczuk, Richard Szeliski, and Michael F. Cohen. The lumigraph. In Holly Rushmeier, editor, *Computer Graphics (SIGGRAPH '96 Proceedings)*, volume 30, pages 43–54, August 1996.

[47] Paul Haeberli and Kurt Akeley. The accumulation buffer: Hardware support for high-quality rendering. In Forest Baskett, editor, *Computer Graphics (SIGGRAPH '90 Proceedings)*, pages 309–318, 1990.

[48] Kenneth Haines and Debby Haines. Computer graphics for holography. *IEEE Computer Graphics & Applications*, pages 37–46, January 1992.

[49] Michael Halle. Multiple viewpoint rendering. In Michael F. Cohen, editor, *Computer Graphics (SIGGRAPH '98 Proceedings)*, pages 243–254, 1998.

[50] Andrew J. Hanson. Geometry for N-dimensional graphics. In Paul Heckbert, editor, *Graphics Gems IV*, pages 149–170. Academic Press, Boston, 1994.

[51] Thomas J. Haven. A liquid-crystal video stereoscope with high extinction ratios, a 28% transmission state, and one-hundred-microsecond switching. In *True 3D Imaging Techniques and Display Technologies (Proceedings of SPIE)*, volume 761, pages 23–26, 1987.

[52] Thomas S. Huang. Digital holography. *Proceedings of the IEEE*, 59(9):1335–1346, September 1971.

[53] Y. Ichioka, M. Izumi, and T. Suzuki. Scanning halftone plotter and computer-generated continuous-tone hologram. *Applied Optics*, 10(2):403–411, February 1971.

[54] Herbert E. Ives. A camera for making parallax panoramagrams. *Journal of the Optical Society of America*, 17:435–439, December 1928.

[55] Sam H. Kaplan. Theory of parallax barriers. *Journal of the SMPTE*, 59(7):11–21, July 1952.

[56] Lloyd Kaufman. *Sight and mind: an introduction to visual perception*. Oxford University Press, New York, 1974.

[57] M. C. King, A. M. Noll, and D. H. Berry. A new approach to computer-generated holography. *Applied Optics*, 9(2):471–475, February 1970.

[58] B. N. Kishto. The colour stereoscopic effect. *Vision Research*, 5:313–329, 1965.

[59] Gregory Ward Larson, Holly Rushmeier, and Christine Piatko. A visibility matching tone reproduction operator for high dynamic range scenes. *IEEE Transactions on Visualization and Computer Graphics*, 3(4):291–306, October - December 1997. ISSN 1077-2626.

[60] Wai-Hon Lee. Sampled fraunhofer holograms generated by computer. *Journal of the Optical Society of America*, 58:729A, 1968.

[61] Wai Hon Lee. Sampled fourier transform hologram generated by computer. *Applied Optics*, 9(3):639–643, March 1970.

[62] Wai-Hon Lee. Computer generated holograms: Techniques and applications. *Progress in Optics*, XVI(III):119–2323, 1978.

[63] Emmett N. Leith and Juris Upatnieks. Reconstructed wavefronts and communication theory. *Journal of the Optical Society of America*, 52(10):1123–1130, October 1962.

[64] Emmett N. Leith and Juris Upatnieks. Wavefront reconstruction with continuous-tone objects. *Journal of the Optical Society of America*, 53(12):1377–1381, December 1963.

[65] Emmett N. Leith and Juris Upatnieks. Wavefront reconstruction with diffused illumination and three-dimensional objects. *Journal of the Optical Society of America*, 54(11):1295–1301, November 1964.

[66] D[etlef] Leseberg. Computer-generated holograms: display using one-dimensional transforms. *Journal of the Optical Society of America A*, 3(11):1846–1851, November 1986.

[67] Detlef Leseberg. Computer generated holograms: cylindrical, conical, and helical waves. *Applied Optics*, 26(20):4385–4390, October 1987.

[68] Detlef Leseberg. Computer-generated holograms of 3-D objects. In *Holographic Optics II: Principles and Applications (Proceedings of SPIE)*, volume 1136, pages 202–207, 1989.

[69] Detlef Leseberg. Computer-generated three-dimensional image holograms. *Applied Optics*, 31(2):223–229, January 1992.

[70] Detlef Leseberg and Olof Bryngdahl. Computer-generated rainbow holograms. *Applied Optics*, 23(14):2441–2447, July 1984.

[71] Detlef Leseberg and Christian Frère. Computer generated holograms of 3-D objects composed of tilted planar segments. *Applied Optics*, 27(14):3020–3024, July 1988.

[72] L. B. Lesem, P. M. Hirsch, and Jr. J. A. Jordan. Computer synthesis of holograms for 3-D display. *Communications of the ACM*, 11(10):661–674, October 1968.

[73] L. B. Lesem, P. M. Hirsch, and Jr. J. A. Jordan. The kinoform: A new wavefront reconstruction device. *IBM Journal of Research and Development*, 13:150–155, March 1969.

[74] Marc Levoy and Pat Hanrahan. Light field rendering. In Holly Rushmeier, editor, *Computer Graphics (SIGGRAPH '96 Proceedings)*, volume 30, pages 31–42, August 1996.

[75] Lenny Lipton. *Foundations of the Stereoscopic Cinema*. Van Nostrand Reinhold, New York, 1982. ISBN 0-442-24724-9.

[76] Lenny Lipton. Field-sequential electronic stereoscopic projector. In *Projection Display Technology, Sytems, and Applications (Proceedings of SPIE)*, volume 1081, pages 94–100, 1989.

[77] Lenny Lipton. Large screen electro-stereoscopic displays. In *Large-Screen Projection Displays II (Proceedings of SPIE)*, volume 1255, pages 108–113, 1990.

[78] Lenny Lipton. The evolution of electronic stereoscopy. *SMPTE Journal*, 100:332–336, May 1991.

[79] Lenny Lipton and Arthur Berman. Push-pull liquid crystal modulator for electronic stereoscopic display. In Woodrow E. Robbins, editor, *Three-Dimensional Imaging and Remote Sensing (Proceedings of SPIE)*, volume 902, pages 31–44, 1988.

[80] Lenny Lipton and Lhary Meyer. A flicker-free field-sequential stereoscopic video system. *SMPTE Journal*, 93:1047–1051, November 1984.

[81] Charles F. Van Loan. *Computational Frameworks for the Fast Fourier Transform*. SIAM, Philadelphia, 1992.

[82] A. W. Lohmann and D. P. Paris. Binary fraunhofer holograms, generated by computer. *Applied Optics*, 6(10):1739–1748, October 1967.

[83] Mark Lucente. Optimization of hologram computation for real-time display. In *Practical Holography VI (Proceedings of SPIE)*, volume 1667, pages 32–43, 1992.

[84] Mark Lucente. Interactive computation of holograms using a look-up table. *Journal of Electronic Imaging*, 2(1):28–34, January 1993.

[85] Mark Lucente. *Diffraction-Specific Fringe Computation for Electro-Holography*. Ph.D. dissertation, MIT Department of Electrical Engineering and Computer Science, August 1994.

[86] Mark Lucente. Computational holographic bandwidth compression. *IBM Systems Journal*, 35(3–4):349–365, 1996.

[87] Mark Lucente. Holographic bandwidth compression using spatial subsampling. *Optical Engineering*, 35(6):1529–37, June 1996.

[88] David F. McAllister, editor. *Stereo Computer Graphics and Other True 3D Technologies*. Princeton University Press, Princeton, NJ, 1993.

[89] J. T. McCrickerd and Nicholas George. Holographics stereogram form sequential component photographs. *Applied Physics Letters*, 12(1):10–12, January 1968.

[90] P. W. McOwan, W. J. Hossack, and R. E. Burge. Three-dimensional stereoscopic display using ray traced computer generated holograms. *Optics Communications*, 82(1):6–11, April 1991.

[91] John O. Merritt. Often overlooked advantages of 3-D displays. In Woodrow E. Robbins, editor, *Three-Dimensional Imaging and Remote Sensing (Proceedings of SPIE)*, volume 902, pages 46–47, 1988.

[92] Kenneth Meyer, Hugh L. Applewhite, and Frank A. Biocca. A survey of position trackers. *Presence*, 1(2):173–200, Spring 1992.

[93] Doug Moore. Understanding simploids. In David Kirk, editor, *Graphics Gems III*, pages 250–255. Academic Press, 1992.

[94] Takanori Okoshi. *Three-Dimensional Imaging Techniques*. Academic Press, New York, 1976.

[95] Takanori Okoshi. Three-dimensional displays. *Proc. IEEE*, 68:548–564, May 1980.

[96] Robert Patterson and Robert Fox. The effect of testing method on stereoanomaly. *Vision Research*, 24(5):403–408, 1984.

[97] William B. Pennebaker and Joan L. Mitchell. *JPEG Still Image Data Compression Standard*. Van Nostrand Reinhold, New York, 1993.

[98] Eric G. Rawson. 3-D computer-generated movies using a varifocal mirror. *Applied Optics*, 7(8):1505–1512, August 1968.

[99] Whitman Richards. Stereopsis and stereoblindness. *Experimental Brain Research*, 10:380–388, 1970.

[100] J. A. Roese and L. E. McCleary. Stereoscopic computer graphics for simulation and modeling. *Computer Graphics (SIGGRAPH '79 Proceedings)*, 13(3):41–47, August 1979.

[101] John A. Roese and Aida S. Khalafalla. Stereoscopic viewing with PLTZ ceramics. *Ferroelectrics*, 10(1-4):47–51, 1976.

[102] Peter Schröder and Wim Sweldens. *Building Your Own Wavelets at Home*, pages 15–87. 1996.

[103] Alfred Schwartz. Head tracking stereoscopic display. *IEEE Transactions on Electronic Devices*, pages 1123–1127, August 1986.

[104] Ian Sexton. Parallax barrier 3DTV. In *Three-Dimensional Visualization and Display Technologies (Proceedings of SPIE)*, volume 1083, pages 84–94, 1989.

[105] Jerome M. Shapiro. Embedded image coding using zerotrees of wavelet coefficients. *IEEE Transactions on Signal Processing*, 41(12):3445–3462, December 1993.

[106] Lawrence D. Sher. SpaceGraph, a true 3-D PC peripheral. In *Three-Dimensional Imaging and Remote Sensing Imaging (Proceedings of SPIE)*, volume 902, pages 10–16, 1988.

[107] Solomon Volumetric Imaging. Product literature. 2200 One Kendall Square, Cambridge, MA 02139.

[108] Richard Arend Steenblik. The chromostereoscopic process: a novel single image stereoscopic process. In *True 3D Imaging Techniques and Display Technology (Proceedings of SPIE)*, volume 761, pages 27–34, 1987.

[109] Stereographics Corporation. Product literature. 2171 East Francisco Blvd, San Rafael, CA 94901; http://infolane.com/infolane/stereog.

[110] Ivan E. Sutherland. The ulimate display. In *Proceedings of the IFIP Congress*, pages 506–508, 1965.

[111] Ivan E. Sutherland. A head-mounted three-dimensional display. In *Proceedings of the AFIPS Fall Joint Computer Conference*, pages 757–764, 1968.

[112] Homer B. Tilton. Everyman's real-time real 3-D. In *Three-Dimensional Visualization and Display Technologies (Proceedings of SPIE)*, volume 1083, pages 76–83, 1989.

[113] Tullio Tommasi and Bruno Bianco. Spatial frequency analysis for the computer generated holography of 3-D objects. In *Holographic Optics III: Principles and Applications (Proceedings of SPIE)*, volume 1507, pages 136–141, 1991.

[114] Tullio Tommasi and Bruno Bianco. Computer-generated holograms of tilted planes by a spatial frequency approach. *Journal of the Optical Society of America A*, 10(2):299–305, February 1993.

[115] G. Tricoles. Computer generated holograms: an historical review. *Applied Optics*, 26(20):4351–4360, October 1987.

[116] J. J. Vos. The color stereoscopic effect. *Vision Research*, 6:105–107, 1966.

[117] Gregory K. Wallace. The JPEG still picture compression standard. *Communications of the ACM*, 34(4):30–44, April 1991.

[118] James P. Waters. Holographic image synthesis utilizing theoretical methods. *Applied Physics Leters*, 9(11):405–407, December 1966.

[119] James P. Waters. Theoretical, holographic image synthesis. *Journal of the Optical Society of America*, 57:563A, 1967.

[120] James P. Waters. "general" fourier-transform method for synthesizing binary holograms. *Journal of the Optical Society of America*, 58:729A, 1968.

[121] James P. Waters. Three-dimensional fourier-transform method for synthesizing binary holograms. *Journal of the Optical Society of America*, 58(9):1284–1288, September 1968.

[122] John A. Watlington, Mark Lucente, Carlton J. Sparrell, Jr. V. Michael Bove, and Ichiro Tamitani. A hardware architecture for rapid generation of electro-holographic fringe patterns. In *Practical Holography IX (Proceedings of SPIE)*, volume 2406, pages 172–183, 1995.

[123] Charles Wheatstone. Contributions to the physiology of vision - part the first. On some remarkable and hitherto unobserved phenomena of binocular vision. *Philosophical Transactions of the Royal Society of London*, pages 371–394, 1938.

[124] R[odney] Don Williams. Direct volume visualization. In *Proceedings of Visualization '92*, pages 99–106, 1992.

[125] Rodney Don Williams and Jr. Felix Garcia. Volume visualization displays. *Information Display*, 5(4):8–10, April 1989.

[126] The future of holography. *WIRED*, 3(7):60, July 1995.

[127] Ian H. Witten, Radford M. Neal, and John G. Cleary. Arithmetic coding for data compression. *Communications of the ACM*, 30(6):520–540, June 1987.

[128] Toyohiko Yatagai. Stereoscopic approach to 3-D display using computer-generated holograms. *Applied Optics*, 15(11):2722–2729, November 1976.